Title
Development of a Thermally Stable Magnesium-Based Bulk Nanocomposite

Author
Stremfel, Jacob William

Publication Date
2018

UNIVERSITY OF CALIFORNIA

Los Angeles

Development of a Thermally Stable Magnesium-Based Bulk Nanocomposite

A dissertation submitted in partial satisfaction

of the requirements for the degree of Doctor of Philosophy

in Materials Science and Engineering

by

Jacob William Stremfel

2018

ABSTRACT OF THE DISSERTATION

Development of a Thermally Stable Magnesium-Based Bulk Nanocomposite

by

Jacob William Stremfel

Doctor of Philosophy in Materials Science and Engineering

University of California, Los Angeles, 2018

Professor Jenn-Ming Yang, Chair

Magnesium has the potential to become an indispensable structural material alongside aluminum due to its low density. However, magnesium is currently held back in its use as a result of its low strength and poor ductility with relatively limited structural applications. This dissertation presents the results for a processing route that was used to achieve a high-strength and thermally stable magnesium-based bulk nanocomposite in order to increase the applicability of magnesium-based alloys. This processing route included the gas atomization of Mg-4Y-3RE (WE43) powders which were treated by cryomilling (mechanical ball milling in liquid nitrogen) followed by consolidation by spark plasma sintering (SPS) in order to obtain a bulk material. The resulting bulk nanocomposite consisted of approximately 15-20% by volume fraction of extremely fine MgO nanoparticles/grains (< 10 nm) with a bimodally distributed Mg matrix consisting of nanocrystalline

(~10 nm) and coarse grains (~1 μm). Besides Mg and MgO, no other phases were detected suggesting that the rare earth elements were elementally segregated to the grain boundaries. The microstructure contained a quasi-duplex structure consisting of two distinct regions with one of these regions containing only the coarse Mg grains with the other region containing all of the nanocrystalline Mg grains, MgO nanoparticles, and rare earth elements. Focused ion beam (FIB) was used to prepare 4 μm micropillars in order to determine the bulk compressive yield strength along with nanoindentation to evaluate the elastic modulus and hardness. Micropillar compression revealed a compressive yield strength of 325 MPa (compared to 190 MPa for traditional processing consisting of casting and a T6 heat-treatment) with nanoindentation demonstrating an elastic modulus of about 60 GPa and a hardness of 1.25 GPa. The nanocomposite also showed remarkable thermal stability with no observable differences in both its microstructure as well as in its mechanical properties even up to an extremely severe heat-treatment at 450 °C ($0.9T_m$) for 100 hours. The thermal stability was attributed to a combination of the MgO nanoparticles as well as the rare earth elements segregated to the grain boundaries acting as grain boundary pinning sites with the thermal stability of the nanocrystalline regions confining the growth of the discontinuous coarse-grained Mg regions.

This dissertation of Jacob William Stremfel is approved.

Xiaochun Li

Jaime Marian

Jiann-Wen Ju

Jenn-Ming Yang, Committee Chair

University of California, Los Angeles

2018

For Meme

TABLE OF CONTENTS

LIST OF FIGURES

LIST OF TABLES

ACKNOWLEDGEMENTS

I would like to take this opportunity to sincerely thank my advisor, Professor Jenn-Ming Yang for his support and unwavering patience throughout this entire process, without whom, none of this would have been possible. This was a particularly difficult process with lots of personal challenges, and I am extremely grateful for his kindness. I would also like to thank my committee members, Professor Xiaochun Li, Professor Jaime Marian, and Professor Jiann-Wen Ju for their time as well as their advice. In addition to my committee members, I would like to thank Dr. Marta Pozuelo for her encouragement and guidance. I am truly grateful for the countless hours she spent with me, particularly in preparation for the qualifying exam. I would like to thank Dr. Sergey Prikhodko for all of his characterization expertise and genuine desire to teach. I would like to thank Dr. William Hubbard for his extensive help with TEM characterization. His mastery of the Titan is unmatched, bordering on wizardry. I would also like to thank Dr. Saeed Khan for all of his help with XRD and for his generosity in sharing both his time and knowledge. And finally, I would like to thank Dr. Rajiv Tandon for both his advice and generosity with his time as well as his help in obtaining additional magnesium powders. His knowledge and encouragement were immensely appreciated.

CURRICULUM VITAE

University of California, Los Angeles

M.S. in Materials Science and Engineering	2010-2012
B.S. in Materials Engineering	2008-2010

Chapter 1

Introduction

1.1 Magnesium: A Brief Overview

1.1.1 Global Availability

Magnesium is the eight most abundant element and accounts for approximately 2% of the Earth's crust [1]. Due to magnesium's reactivity, native magnesium deposits are not typical. Instead of existing in pure form, magnesium is found in more than 60 naturally occurring minerals [2] and must be mined and processed before elemental magnesium is obtained. Despite existing in this multitude of minerals, magnesium is typically only mined from rock containing dolomite and magnesite due to the relative abundance of these minerals as well as magnesium content and processing restrictions, with dolomite accounting for the vast majority of current magnesium extraction [2]. In addition to being plentiful in the earth, magnesium is the third most abundant element found in the world's oceans behind the elements sodium and chlorine (i.e. common table salt), compromising about 0.13% of seawater by weight [3]. This means that one cubic meter of seawater contains roughly 130 grams of magnesium, making extraction from salt water a viable option given certain economic factors. Magnesium also exists naturally in large concentrations in brines (highly concentrated salt solutions) found in lakes or other large bodies of water in the form of dissolved magnesium chloride. Dissolved magnesium concentrations in brine vary, with the Great Salt Lake in Utah containing an average magnesium concentration by weight of 0.5% [4] and the Dead Sea containing about 3.8% magnesium [5].

1.1.2 Global Production

Up until the 1940s, the only method of commercially producing magnesium was through the electrolysis of fused magnesium chloride. During World War II, with demands for magnesium quickly outstripping supply, alternative forms of magnesium production were investigated with the direct thermal reduction of magnesium oxide being the most feasible. This culminated in what was coined the Pidgeon process [6] after Lloyd M. Pidgeon with the first pilot plant operating in early 1942 [7]. After the war and subsequent decline in demand for magnesium, electrolysis of magnesium chloride returned as the main production method due to the lower production cost. However, since China entered into the market with the first Pidgeon process production plant in 1988 [8], the Pidgeon process (previously thought to be uneconomic and obsolete) has now dominated world production with China's relatively low operating cost and abundance of raw materials [8].

In 2017, world primary production of magnesium was just over 1 million metric tons (1,100,000 metric tons [9]) with production of aluminum (60 million metric tons [10]) and iron and steel (3 billion metric tons [11]) far outweighing overall production. (Just for scale: this means that the world primary production of magnesium for 2017 is the roughly the same amount of magnesium that is dissolved in one cubic kilometer of seawater). Of this over 1 million metric tons of primary magnesium, about 85% (930,000 metric tons) was produced by China, extracted almost exclusively from the mineral dolomite via the Pidgeon process [9]. For the same year, all primary production of magnesium in the United States was recovered by a single electrolytic processing plant which extracted brine from the Great Salt Lake in Utah operated by US Magnesium with a last reported capacity of 63,500 metric tons per year [12]. There is currently no magnesium production through seawater extraction, with the last seawater-based plant in the United States (Freeport, Texas) operated by Dow shutting down in 1998 [13] due to severe price pressures imposed by China's growing magnesium production.

1.1.3 Past and Present Use

Historically, magnesium was extensively used in both the aerospace and automotive industries with large amounts being utilized at the outset of World War II. Magnesium saw its peak for use in automotive applications with the introduction of the Volkswagen Beetle in 1938 which used magnesium alloys for the engine block and gearbox which accounted for roughly 20 kg of the total vehicle weight [14]. The same is true for the use of magnesium in aerospace applications during World War II with the United States Air Force's B-36 long-range bomber reportedly using over 6,500 kg of magnesium in the form of sheets, castings, forgings, and extrusions [15]. Unfortunately, widespread magnesium use in these industries was largely reduced with several concerns in regards to safety and performance. Issues related to corrosion reported in the 1950's and 1960's and fears about magnesium posing a fire hazard led to legislation by the International Air Transport Association, relegating magnesium alloys to only non-structural components in commercial aircraft [16]. Additionally, increasing performance demand on car components, including increased operational temperature and load requirements, saw reduction and elimination of many of these components in automotive production [17].

Use of magnesium and its alloys have since seen a resurgence in applications, with much of these concerns alleviated with the better understanding of magnesium and the development of stronger and more corrosion-resistant alloys. Despite this, however, magnesium alloys still constitute a relatively low proportion of structural components. In the automotive industry, magnesium alloys constitute a very small fraction of the overall vehicle weight, with magnesium only being used in a limited number of body and chassis components [18]. In the aerospace industry, magnesium alloys are not used for structural components by the major aircraft manufactures [19], mainly limited to non-structural engine housings and casings. In the helicopter industry, where weight is of more critical importance, larger adoption of higher strength magnesium alloys has been seen, but still being restricted to non-structural components. In the United States in 2017, the leading use of primary magnesium by weight was in the production of structural magnesium-based alloys including casting and wrought products (38%), with its close secondary use being in the production of aluminum-based alloys including transportation, packaging, and other applications (34%), followed by desulfurization of iron and steel (22%) and other various uses (8%) [20]. Of the structural uses magnesium-based alloys, the majority of these uses are in the automotive and aerospace industries with 98% of the components being produced through casting [21].

1.2 Motivations and Constraints

There has been an ever-increasing interest in magnesium and magnesium-based alloys for structural applications due to its low density (1.74 g/cm^3 for pure magnesium) and relatively high specific strength. There has been particular interest in regard to the automotive and aerospace industries where decreased weight can drastically increase fuel efficiency and overall cost during the lifetime of the vehicle or aircraft. However, despite this increased interest, magnesium has had relatively low implementation in these industries and has largely been overshadowed and outcompeted by aluminum-based alloys. As previously mentioned, behind steel and aluminum, magnesium is the third most commonly utilized metal for use in structural applications. Use of magnesium alloys in these industries has been steadily increasing, but its use has largely been relegated to subcritical components such as casings and housings.

The reason for aluminum alloys being favored comes down to the overall crystal structure of magnesium. Unlike materials with a cubic crystal system, such as aluminum, magnesium has a hexagonal crystal system, specifically a hexagonal closed-packed (HCP) structure, which has considerably less symmetry compared to its cubic competitors. This lower symmetry has a cascading effect on the operating slip systems which has an effect on the ductility, strength, and texture. These drawbacks of magnesium are one of the main reasons (other than cost) that aluminum alloys have seen much wider implementation despite the fact that aluminum is 55% heavier than magnesium with aluminum having a density of 2.70 g/cm^3. Another reason why magnesium alloys have been typically less favored in certain applications is due to low creep resistance at elevated temperature. Magnesium and aluminum alloys both share this fate due to their relatively low melting temperatures of 650 and 660 °C, respectively.

1.3 Research Objectives and Scope

The objective of this research will be to take an existing high-strength Mg alloy, Mg-4Y-3RE (WE43) where Y = yttrium and RE = rare earth elements, and further strengthen this alloy through grain boundary strengthening via grain refinement. This strengthening will be achieved by first obtaining powder particles of the WE43 alloy from gas atomization and then processing these powders via cryomilling (mechanical ball milling at liquid nitrogen temperatures) which will drastically refine the grain structure, obtaining powders containing nanocrystalline grains. These cryomilled powders will then be consolidated through a sintering process called spark plasma sintering (SPS) in order to obtain a bulk sample (as-SPS'ed). The as-SPS'ed sample will then undergo various heat treatments to study the thermal stability in regards to both the microstructure and mechanical properties. The processes of gas atomization, cryomilling, and SPS will discussed in detail in the subsequent chapters.

Several characterization methods will be used to investigate the various aspects of the powder samples, as-SPS'ed sample, and heat-treated samples. For the powder samples, both the as-atomized powder (or as-received powder) and cryomilled powder, the powder particle size and morphology will be studied using a SediGraph particle analyzer along with scanning electron microscopy (SEM). For all powder and bulk samples, the phase and chemical composition will also be investigated using X-ray diffraction (XRD), both conventional and synchrotron, as well as energy dispersive X-ray spectroscopy (EDS). For all powder and bulk samples, the microstructure will be investigated using SEM, transmission electron microscopy (TEM), as well as scanning transmission electron microscopy (STEM) with EDS being used for both SEM and STEM. For all bulk samples, the microstructure will be further examined using electron backscattered diffraction (EBSD). Lastly, the mechanical properties of all bulk samples will be tested using nanoindentation to obtain both the hardness and elastic modulus, while also conducting bulk compression tests along with *in situ* micro-pillar compression.

Chapter 2

Literature Review

2.1 Magnesium and its Crystal Structure

As briefly mentioned in the previous chapter, magnesium is non-cubic, forming a hexagonal close-packed (HCP) crystal structure with lattice constants a = 0.3209 and c = 0.5210 nm giving a c/a ratio of 1.624. For an ideal HCP configuration, the c/a ratio would be equal to $\sqrt{(8/3)}$ or 1.633 with the most densely packed planes being the {0001} planes (i.e. the basal planes). Since magnesium's c/a ratio is close to ideal, this results in a low critical resolved shear stress (CRSS) with basal slip being the dominate operating slip system at room temperature [22]. This is in contrast to titanium which also has an HCP structure but has a c/a ratio of 1.588 which deviates from the ideal c/a ratio. This relatively small deviation in the c/a ratio of titanium resulting in the most densely packed planes being the prismatic planes with slip being more favorable on prismatic planes than basal planes. It should be stated that while the c/a ratio is important in explaining some of magnesium's fundamental deformation characteristics, it does not lead to a fundamental understanding of the deformation mechanisms. It is purely a configurational consideration with other factors, such as electronic configuration, needing to be taken into account.

Another important aspect of magnesium's crystal structure that needs to be considered when trying to understand the deformation mechanisms is the underlying symmetry. Hexagonal lattices are intrinsically less symmetric than cubic lattices, with HCP losing even more symmetry with its 2-point basis compared to its 1-point basis counterpart. Compared to face-centered cubic (FCC) and body-centered cubic (BCC) which both have three 4-fold symmetry axes and four 3-fold axes, HCP only has one 3-fold axis (<c>) and three 2-fold axes (<a1>, <a2>, and <a3>) as seen in Figure 2.1 with <a3> = -(<a1> + <a2>) and the basal plane shown in black. This lower symmetry leads to non-equivalent slip systems which is the source of magnesium's lack of ductility and lack of formability at room temperature. First demonstrated 1928, von Mises [23] showed that in order to perform an arbitrary plastic deformation on a polycrystalline material by slip, the material needs to have a minimum of five independent slip systems (i.e. a slip direction and slip plane). If five independent slip systems are not present, lack of volume conversation can lead to the formation non-volumetric changes such as of pores and cracks which are detrimental to the material properties eventually causing the material to fracture.

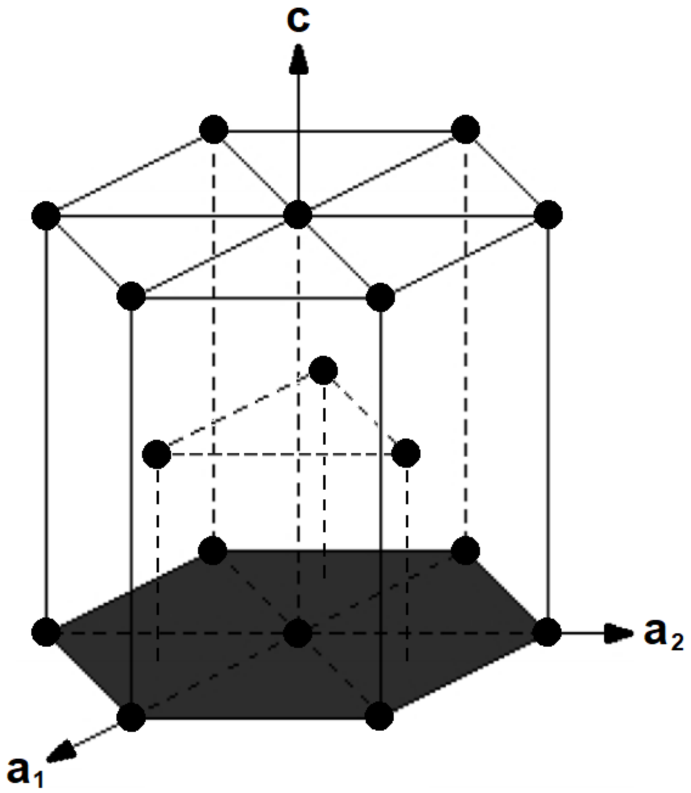

Figure 2.1: Hexagonal close-packed (HCP) crystal structure of magnesium with the basal plane indicated in dark grey.

2.2 Grain Boundary Strengthening

Ever since the early 1950s with the published works of both Hall [24] and Petch [25] on the yield strength of polycrystalline α-Fe, it was known that the grain size of a material could influence its yield strength with a decreasing grain size leading to an increase in the yield strength. This empirical relationship between grain size and yield strength is known as the Hall-Petch relationship and is given below in Equation 2.1:

$$\sigma_y = \sigma_0 + \frac{k}{\sqrt{d}} \qquad \textit{Equation}\ 2.1$$

where σ_y is the yield strength of the material, d is the grain diameter or grain size, and σ_0 and k are material-dependent constants. This empirical relationship, while largely not understood when it was first observed, has been explained on the basis of dislocation pile-up within a grain [26] with the stress needed to induce a dislocation in an adjacent grain increasing with a smaller grain and less ability of the grains to sustain pile-up. This effect can also be understood intuitively by imagining grain boundaries as obstacles for the movement of dislocation with a decreasing grain size constricting the movement of dislocations.

It should be noted that the relationship given by the Hall-Petch is somewhat limited in its application, with applicability failing at the extremes (i.e. amorphous materials). That is to say, there is a limit to how much you can strengthen a material by decreasing its grain size due to the practical limitations on how small a grain can be. Also, it would be inconceivable for a material to increase its yield strength beyond its theoretical strength. Nieh [27] theorized that the Hall-Petch relationship would ultimately break down when the grain size decreased below a critical value such that the grains could no longer support more than one dislocation. The equation governing this critical grain size is given in Equation 2.2:

$$L_c = \frac{3Gb}{\pi(1-v)\cdot H} \qquad \textit{Equation } 2.2$$

where L_c is the critical equilibrium distance between two dislocations, G is the shear modulus, b is the Burgers vector, v is Poisson's ratio, and H is the hardness. Nieh postulated that if the grain size of a material decreases below this critical equilibrium distance between two dislocations, the Hall-Petch relationship would break down as no dislocation pile-up could take place and the yield strength of the material would decrease. Nieh also reasoned that if the grain size approached zero, the material would essentially be amorphous and any effects of grain boundary strengthening via Hall-Petch would be lost.

2.3 Severe Plastic Deformation

In order to obtain the increased strength associated with grain boundary strengthening, nanocrystalline grains, that is grains less than 100 nm, must first be achieved. In this effort to produce nanocrystalline or nanostructured materials (materials containing at least some dimensionality in the nanocrystalline range), several techniques have been developed. Most of the techniques fall under the top-down approach in which small grains are achieved through the decomposition of larger grains. This is in contrast to a bottom-up approach in which small grains are built from non-existing structures. For the top-down approaches, almost all of these techniques use the principle of severe plastic deformation (SPD) [28,29] which imposes extremely high strains on a material through mechanical deformation. Popular techniques that use SPD to achieve bulk nanocrystalline or nanostructured materials include equal-channel angular pressing (ECAP) [30,31] and high-pressure torsion (HPT) [32-34]. The process of ECAP involves taking a rod-shaped billet and making repeated passes through a die which is constrained with a sharp bend, with HPT involving a thin disk being subjected to high hydrostatic pressure while rotating [35].

There also exists another SPD technique in which the levels of strain are imparted to metallic powders in order to obtain nanocrystalline powders. This process is extremely popular with several variations and with several different names including *mechanical alloying*, *mechanical milling*, or more generally *mechanical attrition*. All of these names describe basically the same process in which metallic powders (either elemental, mixed, multiphase, or composite) are placed inside a ball mill in order to homogenize and/or reduce the grain size of the resulting powder. Strictly speaking, mechanical alloying refers to the process of taking different powders (i.e. not an elemental or single phase) and milling these powders together to produce a homogenous final powder which requires mass transfer between particles, and mechanical milling refers to a process in which no homogenization is required in the case of pure metals, and only grain refinement is needed [36,37]. However, these terms are used somewhat interchangeably in the literature. While this technique is powerful in its ability to reliably produce nanocrystalline powders, there are some disadvantages to this technique, mainly the introduction of impurities during the ball milling process and the additional processing that is required to produce a bulk sample which has its own set of disadvantages including grain growth and residual porosity.

2.4 Cryomilling

A more advanced version of mechanical ball milling was developed and patented by the Exxon Research and Engineering Company in 1986 for the purpose of mechanically alloying composite powders to produce an iron alloy [38]. This patent showed that compared to conventional ball milling in either air or argon gas, milling in liquid nitrogen could achieve a finer particle size with much shorter milling times and smaller overall grain structures. Soon after patenting this process, the first described use of this process, coined *cryomilling*, occurred in 1988 with a dispersion-strengthened aluminum composite [39] with the main advantage of this technique being that at cryogenic temperature, the recovery and recrystallization process is suppressed allowing smaller grain sizes to be achieved [36]. This is also one of the slight disadvantages of this technique, making mass transfer more difficult to attain since cold welding is also suppressed at lower temperature. Another disadvantage with this technique being that with the intimate contact with the liquid nitrogen, contamination with nitrogen (as well as oxygen) is also introduced into the powders which may or may not be advantageous.

Cryomilling typically occurs in an attrition mill as seen in Figure 2.2. In this process, prior to milling, the powders and milling media are cooled to cryogenic temperature. This reduces powder agglomeration and well as ensures consistent results across different milling runs. In an effort to reduce powder agglomeration of the powders, a process control agent (PCA) is sometimes used which adsorbs onto the surface of the powder particles, inhibiting cold welding between the particles. Another benefit of using a PCA is an increase in powder yield as cold welding between powder particles and the milling media and chamber is reduced, making more of the powder recoverable. The PCA is typically an organic compound, with stearic acid being the most common. During the milling operation, liquid nitrogen is circulated into the milling chamber and is continuously monitored and replenished to maintain a constant cryogenic temperature. Evaporated nitrogen gas is expelled through a special valve fitted with a particle filter so that no powder particles escape with the exhausted nitrogen gas. The liquid nitrogen makes direct contact with the milling media and powders, creating a liquid slurry with complete immersion of the powders. This is in contrast with the “dry” variation of this technique where the powder and milling media are externally cooled to cryogenic temperatures, with the powders never coming into direct contact with the liquid nitrogen.

Once the milling is complete, this powder and liquid nitrogen slurry is collected and transferred to a glovebox where the nitrogen is allowed to evaporate. The final processing step prior to compaction of the powders typically is a degassing step in which any residual contaminates such as nitrogen or water vapor are removed. The degassing step is particularly important if a PCA is used in the milling process.

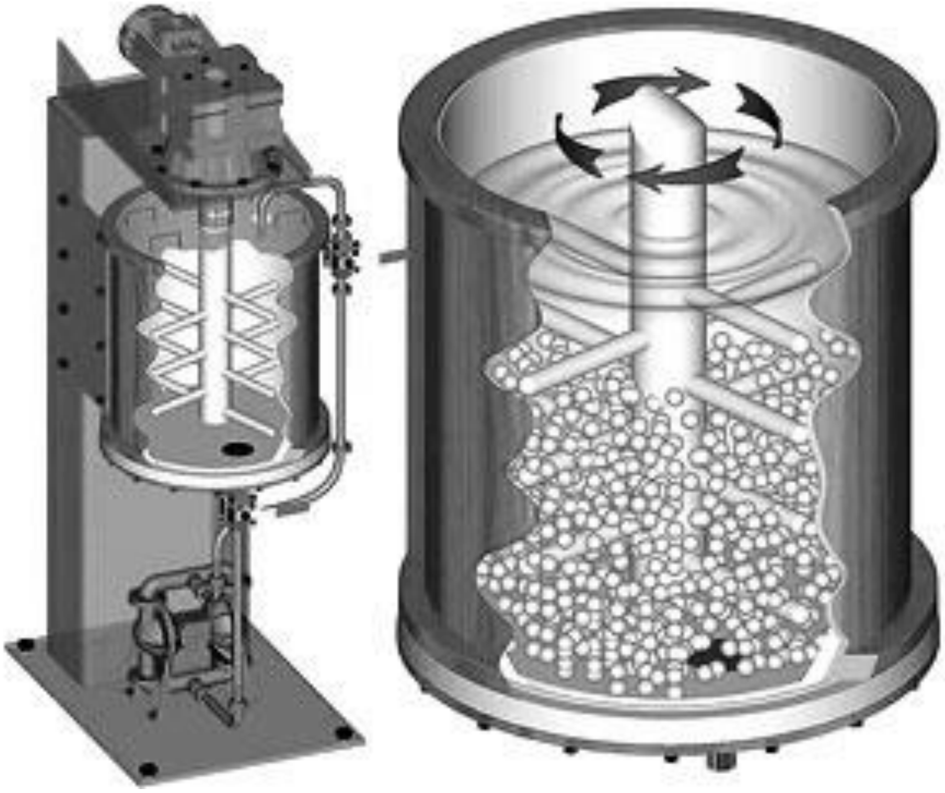

Figure 2.2: Attrition ball mill involved in the cryomilling process showing the milling media and liquid nitrogen.

2.5 Spark Plasma Sintering

Once the powders have been processed either by conventional ball milling or by cryomilling to achieve a nanocrystalline grain structure, the powders will need to be consolidated into a bulk material while maintaining the nanocrystalline nature of the powders. Traditionally, the sintering of the powders has been achieved with standard consolidation methods such as hot isostatic pression (HIP) [40,41] which applies isostatic pressure and external heat to consolidate the powders. However, due to the external heating by the HIP process, also commonly referred to as "HIPing," long dwell times, sometimes as long as several hours, and high temperatures are required to achieve optimal densification of the powders. These long dwell times and high temperatures are due to the fact that the powders are heated externally and rely on radiation to conduct the external heat internally to the powders. Due to this relatively slow heat transfer and thus slow heating rate, considerable grain growth of the nanocrystalline grains can occur during the consolidation process which ultimately defeats the purpose of creating nanocrystalline powders. Lower temperatures along with higher pressures can be attempted during the HIPing process, but this usually results in larger residual porosity in the material which requires extrusion or other post-processing techniques in order to achieve a fully dense material.

Due to these issues associated with the consolidation of metallic powders, more specifically with the consolidation of nanocrystalline metallic powders, a different method was developed called spark plasma sintering (SPS) [42,43] to overcome some of the drawbacks associated with more conventional sintering methods. Different from HIPing, SPS uses an applied and pulsed current to heat the sample through a conductive die (usually graphite) as shown in Figure 2.3. Although current-assisted densification of powders was first proposed and patented by Taylor in 1933 [44], the current form of SPS was established in 1990 with the first commercial development by Sumitomo Heavy Industries (Tokyo, Japan) [45]. As briefly just mentioned, the SPS process involves a pulsed DC current which is applied through a conductive die along with the simultaneous application of a uniaxial pressure. The heating of the sample is achieved through Joule heating in the graphite die as well as through the powders themselves (if conductive), providing extremely high heating rates on the order of 1,000 °C/min [43]. This high heating rate enables sintering with limited grain growth due to the suppression of surface diffusion as well as the shorter dwell times, with the entire process taking only a few minutes rather than a few hours compared to HIP. In addition to the limited grain growth, SPS has been attributed to better powder densification as a result of plasma discharge which eliminates surface oxides [46,47]. However, despite these claims that the SPS offers the advantage of plasma discharge to enhance powder compaction, there is a lack of unambiguous experimental evidence [43].

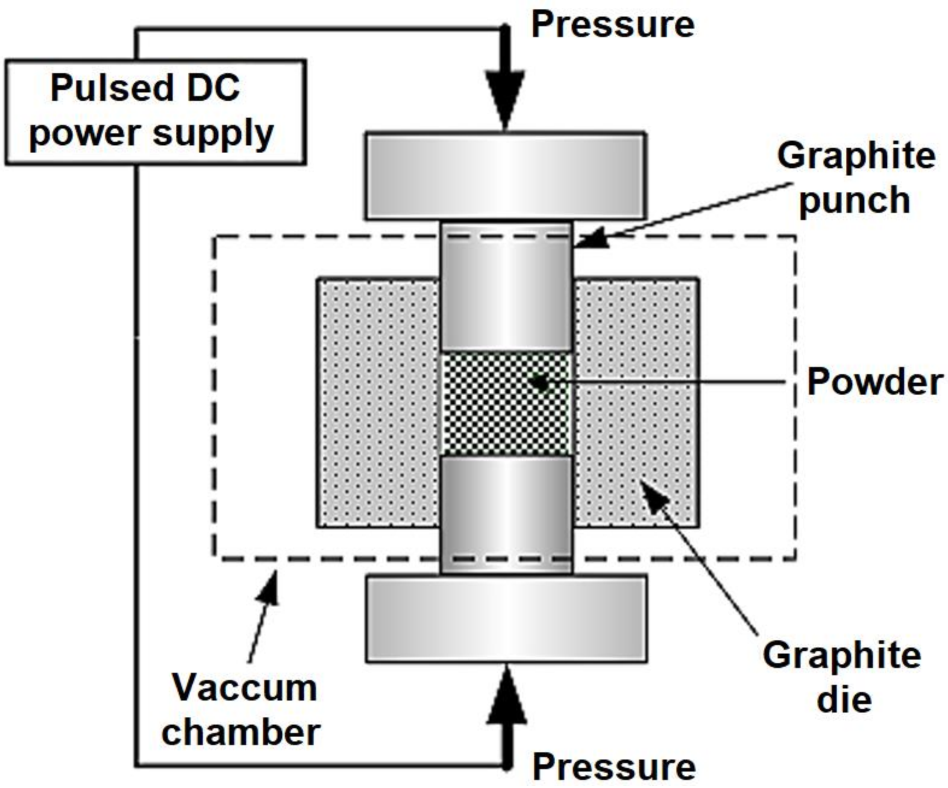

Figure 2.3: Schematic of the spark plasma sintering (SPS) set-up showing the metallic powders inside of the graphite die with applied pressure and applied current.

Chapter 3

Materials and Processing

3.1 Gas Atomization and Alloy Composition

The Mg-4Y-3RE (WE43) powders were obtained through Magnesium Elektron Powders (Manchester, New Jersey) which were produced via an inert gas atomization process. Gas atomization is a widely used commercial process in which small spherical metal powder particles are obtained which are subsequently used in applications such as powder metallurgy or can be used for the production of pigments, catalysts, and solid rocket propellant [48]. In this process, which is shown in Figure 3.1, the desired material is placed in an internal furnace which melts the metal prior to gas atomization. This can be a pure metal or a particular alloy. For the case of an alloy, the alloy chemistry is set in the molten metal prior to the gas atomization process. This is achieved by melting an ingot with the desired composition and making slight adjustments to the melt if needed. In either case, once the material is fully molten the liquid metal is then injected into a high-pressure nozzle where an inert gas such as argon is pumped at high pressure, disrupting the flowing metal and separating into distinct powder particles traveling at high velocity. This process results in each powder particle having a representative chemical composition in relation to the master alloy. That is to say, each powder has the same chemical composition and is not a result of adding separate elements powders together. As previously mentioned, this process also results in mostly spherical particles along with some asymmetrical particles. This powder is then collected and sorted by particle size, usually by sieve.

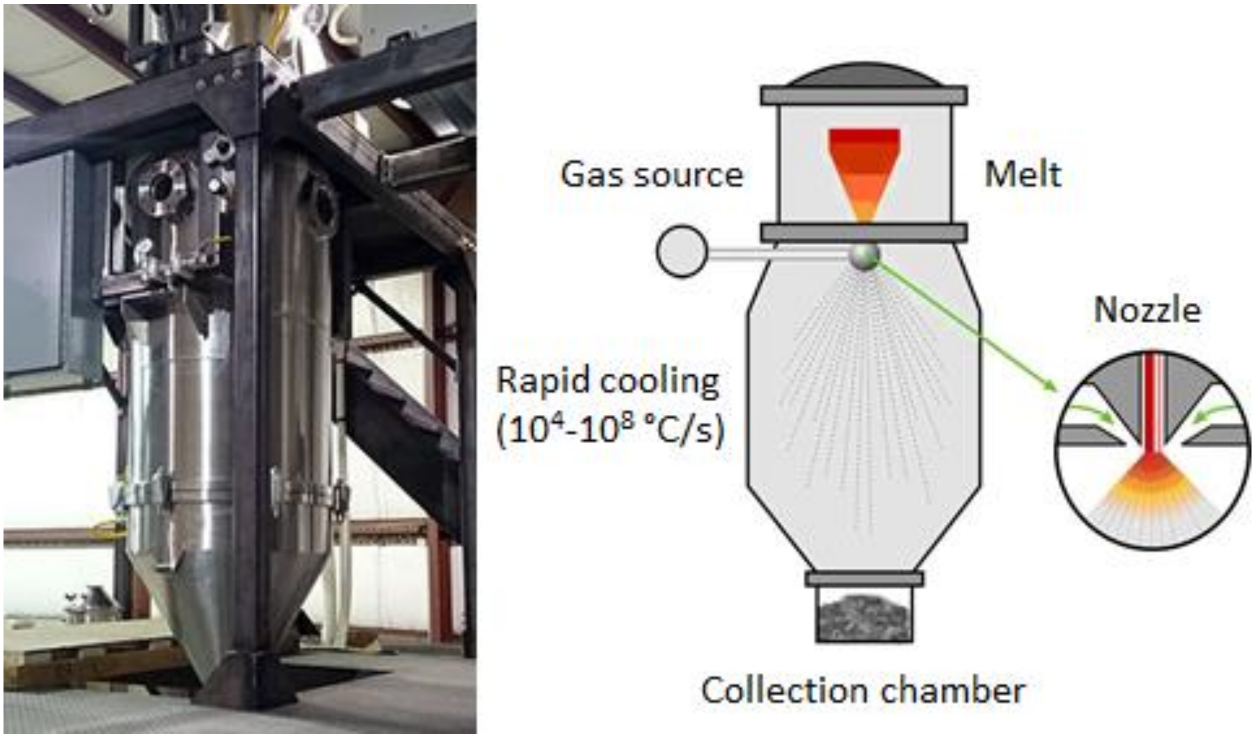

Figure 3.1: Overview of the gas atomization process in which the molten metal alloy is transformed into metallic powders.

Other notable parts of the atomization process include rapid solidification and the intentional passivation of the powders by oxidation. Due to the large temperature difference between the molten metal and the atomization chamber and due to the large velocities in which the molten droplets are subjected to, large cooling rates are observed for the powders one the order of 10^4 °C/s [48] for powder particles in the micrometer size range. This rapid cooling rate often leads to significant undercooling which gives rise to the supersaturation of alloying elements in solid solution beyond their equilibrium values at room temperature or the solidification of non-equilibrium phases. As the molten metal solidifies, the particles are also subjected to a controlled oxygen enriched environment in which the powders are intentionally passivated. This passivation is done to reduce the risk of the powders igniting as magnesium powders tend to be highly flammable. This results in a relatively thin oxide layer on the particle’s surface.

Below is the chemical position of the WE43 powders provided by Magnesium Elektron in the Certificate of Compliance and Analysis presented in Table 3.1 which shows the yttrium content at just below 4 wt. % along with a rare earth (RE) content of just over 3 wt. % with neodymium (Nd) contributing about 70% of the overall RE elements. There is also about a half percent of zirconium (Zr) which is typically added to this alloy to promote grain refinement during solidification when this alloy is cast. It is also important to note that the particle size of the gas atomized powders was a -325 mesh, meaning that the maximum nominal particle diameter is less than 45 μm as a result of the sieving process. The complete particle size data is presented in Table 3.2 which shows that the number and volume mean diameter of the as-received powder are 4.8 ± 2.5 μm and 19.6 ± 11.6 μm, respectively. Additionally, a scanning electron microscopy (SEM) image of the as-received powder is given in Figure 3.2 which shows that most of the particles are spherical in shape due to the gas atomization process as just described.

Table 3.1: Chemical analysis of as-received powder (Certificate of Compliance and Analysis).

	Mg	**Y**	**Total RE**	**Zr**	**Li**	**Al, Ag, Mn**	**Cu, Si, Zn (each)**	**Fe**
wt. %	92.1	3.96	3.29 (Nd: 2.30)	0.56	0.05	0.01 (each)	<0.01	<0.005
at. %	97.9	1.15	0.57 (Nd: 0.41)	0.16	0.2	0.01, 0.002, 0.005	<0.004	<0.002

Table 3.2: Particle size distributions of the as-received powders as measured via SediGraph.

	Mass division diameters*			**Avg. particle diameters†**		**Span‡**
	D10 (μm)	D50 (μm)	D90 (μm)	D[1,0] (μm)	D[4,3] (μm)	
As-Received pwd.	4.4	17.1	35.4	4.8 ± 2.5	19.6 ± 11.6	1.8

* Represent the particle size in which the stated value (in percent) of the powder's cumulative mass falls below.
† D[1,0] and D[4,3] are the number and volume averages, respectively.
‡ (D90-D10)/D50

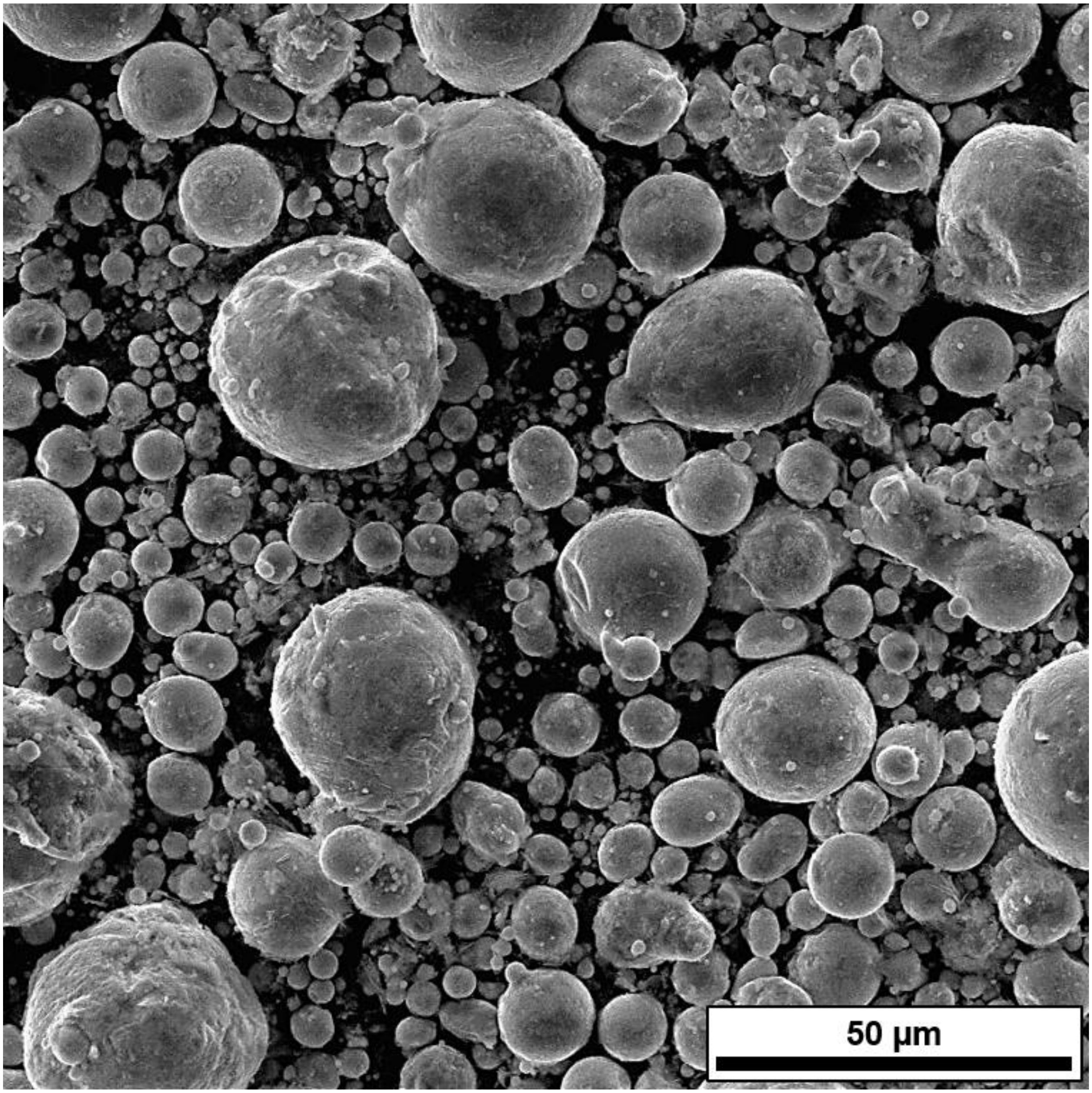

Figure 3.2: Scanning electron microscopy (SEM) image the as-received powder as processed by gas atomization.

3.2 Cryomilling of the As-Received Powder

In order to reduce the grain structure as well as homogenize the phases and elemental distribution of the as-received powder, a Szegvari Batch Attritor (Model 1-S, 5.7 Liter) by Union Process (Akron, Ohio) extensively modified for liquid nitrogen and argon use by California Nanotechnologies (Cerritos, California) was used for cryomilling of the as-received WE43 powders, with a similarly modified mill given in Figure 3.3 [49]. Grade 440C martensitic stainless-steel balls (6.4 mm diameter) were used as the milling media with a 30:1 ball-to-powder mass ratio which is common for the milling of metallic powders. It should be noted that no process control agent (PCA) was added to the powders for the cryomilling, which is typically used in order to coat the powder to prevent or reduce powder agglomeration during the milling process. A typical PCA used in milling is stearic acid which is usually added in about 1 wt. % of the total powder mass.

Prior to the cryogenic milling, in order to minimize iron contamination, approximately 400 g of the 1 kg of powder was run in the mill at ambient temperature for a coating process to coat the chamber walls and milling media. About half of this powder (200 g) was consumed in the coating process, with the other half of the powder (200 g) being removed from the chamber and discarded due to probable iron contamination, leaving just the coated milling media and chamber behind. This was followed by a 2-hour cool-down period in which the coated chamber walls and milling media were brought from ambient to cryogenic temperatures with liquid nitrogen (77 K). Once final temperature was reached, 500 g of fresh powder was added to the chamber and milling was performed for 8 hours with a rotation speed of 180 rpm. Once milling was complete, the liquid nitrogen and slurry mixture was collected via a gravity valve at the bottom of the tank and taken to a nitrogen glove box where the liquid nitrogen was allowed to evaporate in order to reduce oxidation of the powders. A summary of the milling parameters used for the cryomilling of the as-received powder is presented on the next page in Table 3.3.

Figure 3.3: Modified attrition mill to accommodate the use of liquid nitrogen with the milling of metallic powders [49].

Table 3.3: Summary of cryomilling parameters.

Milling media:	440C stainless steel balls / 6.4 mm diameter
Ball-to-powder mass ratio:	30:1 / 500 g of powder
Temperature:	77 K (liquid nitrogen)
Milling speed, milling time:	180 rpm, 8 hours
Process control agent:	None used

3.3 Spark Plasma Sintering of the Cryomilled Powder

With the goal of consolidating the nanocrystalline powders with the least amount of grain growth, spark plasma sintering (SPS) was used with a Dr. Sinter Lab Spark Plasma Sintering System (Model SPS-515S) by SPS Syntex (Kawasaki, Japan) shown in Figure 3.4. SPS consolidation was also performed at California Nanotechnologies. Prior to compaction, 10 g of cryomilled powder was placed in a graphite die with a diameter of 25 mm, lined with graphite foil to help in the heat distribution as well as the longevity of the die. The die was then placed between the two graphite punches which transfer the uniaxial load to the powders during loading. The heating was achieved through a pulsed alternating electric current that was applied through the graphite punches and was monitored by a K-type thermocouple attached to the outer wall of the graphite die. The pulse duration was 3.3 ms with an on-off ratio of 12:2 meaning that current was pulsed continuously for 39.6 ms followed by 6.6 ms with no pulse and subsequently repeated. This cyclic heating allows for localized joule heating to take place, compacting the powders locally without excessively heating the entire sample.

Prior to heating, a pre-press of 10 kN (20 MPa) was applied to slightly compact the powders and aid in powder consolidation when heated. The sintering was performed under vacuum with the force and temperature simultaneously ramping up with an approximate heating and loading rate of 100 °C/min and 10 kN/min, respectively, before reaching a maximum temperature of 425 °C and a maximum force of 50 kN (100 MPa). The powders were then held at maximum temperature and force for a duration of approximately 5 minutes before the current and force were quickly removed, allowing the now-compacted sample to cool to room temperature. The consolidated bulk samples this process produced are cylindrical in shape, referred to as *SPS pucks* and more generally as the *as-SPS'ed* sample, having a nominal diameter of 25 mm and an approximate height of 10 mm. A complete summary of the SPS parameters are listed below in Table 3.4.

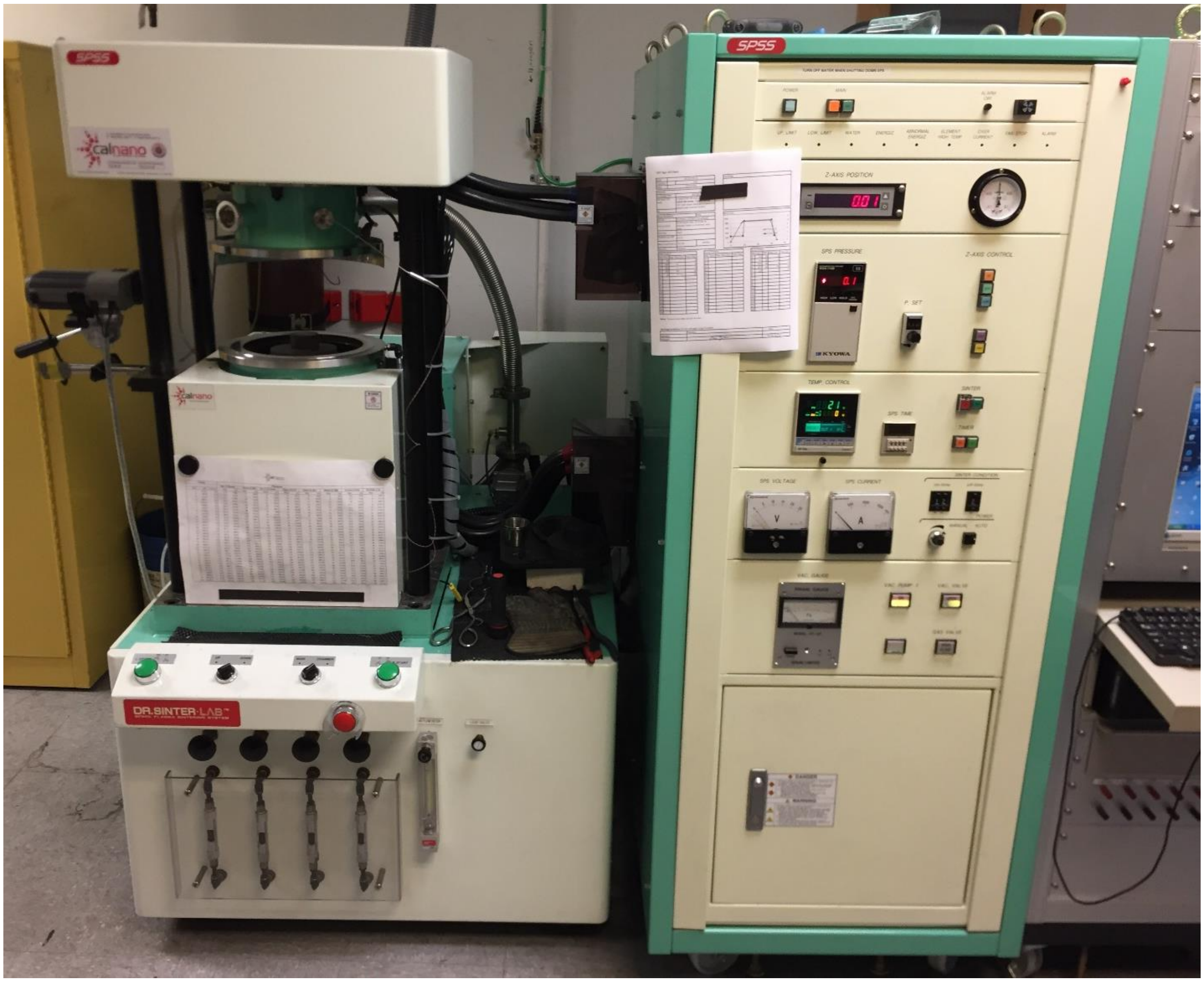

Figure 3.4: The Dr. Sinter Lab Spark Plasma Sintering System (Model SPS-515S) by SPS Syntex (Kawasaki, Japan) located at California Nanotechnologies (Cerritos, California).

Table 3.4: Summary of SPS parameters.

Die material, diameter:	Graphite, 25 mm
Pre-press:	10 kN (20 MPa) prior to heat ramp
Loading rate, max. load:	10 kN/min, 50kN (100 MPa)
Heating rate, max. temp.:	100 °C/min, 425 °C
Pulse duration, on-off sequence:	3.3 ms, 12:2 (39.6 ms on, 6.6 ms off)
SPS puck mass, dimensions:	10 g, 25 mm diameter x 10 mm height

It is important to note that several different sintering temperatures were experimented with before 425 °C was settled on as the optimum sintering temperature. Other temperatures that were investigated were 375 and 400 °C with the first sintering temperature being 375 °C and then increasing at intervals of 25 °C to enhance the consolidation by minimizing porosity. Attempts to increase the sintering temperature beyond 425 °C were not attempted due to the relatively low porosity with the sample sintered at 425 °C (discussed below) and due to the fact that the sample SPS'ed at 425 °C only saw slight increases in density compared to the sample sintered at 400 °C. An additional concern was that increasing the sintering temperature any further would result in a homologous temperature nearing $0.9T_m$ where appreciable grain growth could occur and the possibility of localized melting. This concern was also based on the method in which the sintering temperature is monitored which is by a thermocouple which is placed on the outside of the graphite die, just inside of a small grove made for the thermocouple to sit in. Due to the fact that the powder are themselves conductive, the true temperature of the powders is therefore likely higher than the temperature that is monitored during the sintering process. In hindsight, given the remarkable thermal stability of the consolidated alloy which will be discussed in Chapter 7, sintering the cryomilled powders at 450 °C would have probably worked as well and reduced the residual porosity even further.

All of the resulting density values of the as-SPS'ed samples for the differing SPS consolidations temperatures performed at 375, 400, and 425 °C are listed in Table 3.5 along with their respective relative densities. For the relative density values, all three of the as-SPS'ed samples consolidated at 375, 400, and 425 °C were extruded at a 2:1 ratio in order to remove any porosity to achieve a perfectly dense material. Despite having different as-SPS'ed densities, after extrusion they all had the density of 2.14 g/cm^3 indicating that this was the fully compact density with the lower as-SPS'ed densities indicating various degrees of porosity. The value of 2.14 g/cm^3 was then used as the true density and the as-SPS'ed density values were simply divided by this value to obtain their respective relative densities. Therefore, the as-SPS'ed sample consolidated at 425 °C has a measured density of 2.11 g/cm^3 with an estimated relative density of 98.6%. Although several different sintering temperatures were experimented with when determining the best SPS temperatures, all of the experimental data generated and presented in the following chapters is with as-SPS'ed samples sintered at 425 °C.

Table 3.5: Summary of the SPS temperature and resulting as-SPS'ed density.

SPS temperature (°C)	Density (g/cm^3)*	Relative density† (%)
375	1.99	93.0
400	2.08	97.2
425	2.11	98.6

* Measured by Archimedes' method.
† Calculated by dividing the density by the extruded density (2.14 g/cm^3) which was assumed to be fully dense.

It is important to note that the as-received powders were also compacted via the SPS process to serve as a control or baseline to better elucidate the effect that the cryomilling and the SPS process has on both sets of powders. In order to avoid confusion between these two SPS samples, that is the sample produced from consolidating the as-received powder and the sample produced from consolidating the cryomilled powder by the SPS consolidation process, the sample derived from the as-received powder will be referred to as the *SPS control* sample and the sample derived from the cryomilled powder will strictly be referred to as the as-SPS'ed sample, as described earlier. An interesting first observation is that the as-received powder, and the WE43 alloy in general, has a reported density of 1.84 g/cm^3 which is significantly different than the density of the as-SPS'ed sample which was measured at 2.14 g/cm^3 for the fully compacted (i.e. extruded) sample. This density of 1.84 g/cm^3 was also measured for the SPS control sample (the sample produced from consolidating the as-received powders by SPS) which indicates that there is indeed a fundamental density difference between the as-received and cryomilled powders. This difference in density will be explored in detail later on in Chapter 4 which will demonstrate that the increased density related to the cryomilled powder is indeed real and was a result of *in situ* oxidation during the cryomilling process.

3.4 Materials and Processing Overview

The overall process from gas atomization, cryomilling, and SPS consolidation to achieve the as-SPS'ed sample is given in Figure 3.5 along with the major parameters involved with each of these steps and overall dimensions of the final consolidated material. Again, it will be noted that all three of these steps (gas atomization, cryomilling, SPS consolidation) will be involved in producing the as-SPS'ed sample from the consolidation of the cryomilled powders. In addition to this sample, the as-received powder will also be consolidated via SPS, thus skipping the cryomilling process with this sample being referred to as the SPS control sample.

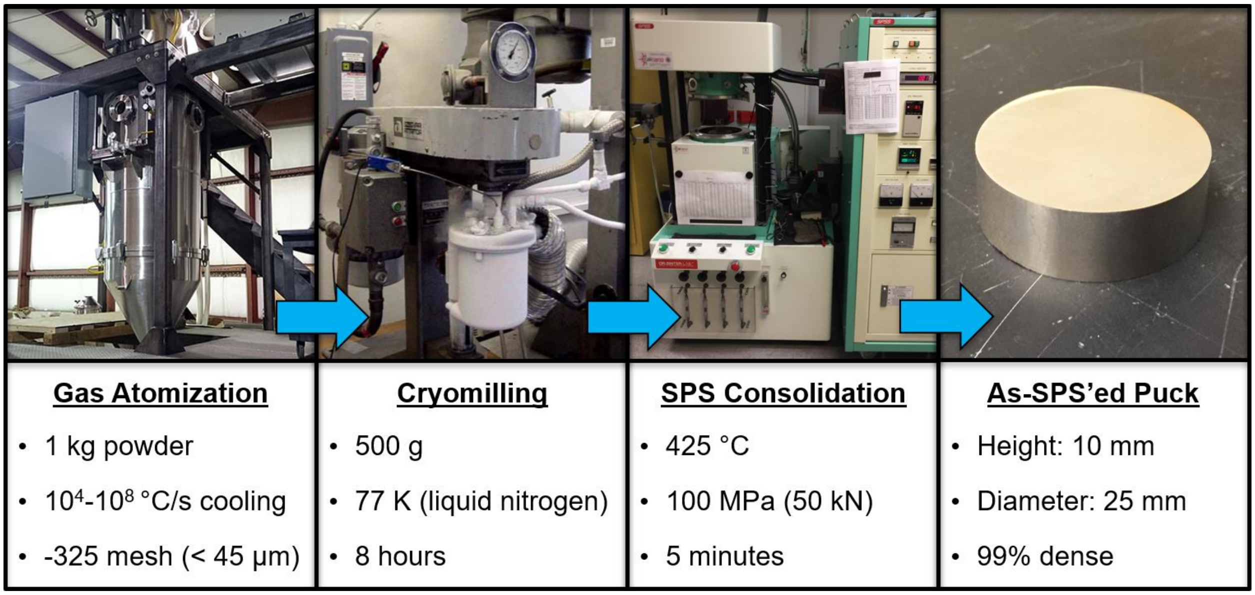

Figure 3.5: Materials and processing overview for the as-SPS'ed sample.

3.5 Heat Treatment of the As-SPS'ed Sample

In order to determine the thermal stability of the as-SPS'ed sample, four different heating regimes were devised: 150, 250, 350, and 450 °C. As-SPS'ed samples were subjected to each of these temperatures for 2, 4, 8, 16, 32, 64, and 100 hours for a total of 28 separate testing conditions. A summary of these heat treatments along with the homologous temperatures are presented in Table 3.6. All samples were heated in a 2.5 cm diameter quartz tube that was brought to working temperature prior to the samples being inserted. Once the samples were placed inside the quartz tube, the tube was quickly placed under vacuum (< 0.1 Pa) to reduce oxidation. Samples were subsequently removed at the predetermined times while the furnace was still at operating temperature and allowed to cool to room temperature. It should be noted that the surface finish on the all the heat-treated samples appeared to be unaffected with exception of the sample heat treated at 450 °C for 100 hours. After this particular heat treatment, the surface of the sample contained a significant amount of white powder which was assumed to be MgO. All other heat-treated samples contained no such powder.

Table 3.6: Summary of heat treatments that the as-SPS'ed sample were subjected to along with the homologous temperature of each temperature regime.

Temperature (°C)	T/T_m*	Time (hr)
150	0.52	2, 4, 8, 16, 32, 64, 100
250	0.64	2, 4, 8, 16, 32, 64, 100
350	0.77	2, 4, 8, 16, 32, 64, 100
450	0.89	2, 4, 8, 16, 32, 64, 100

* Calculated using a melting temperature of 540 °C (813 K).

Chapter 4

Characterization Techniques

4.1 Particle Size

To characterize the particle size distributions of the powders, a SediGraph III 5120 by Micromeritics was used for both the as-received and cryomilled powders. In this process, approximately 1 g of powder was dispersed in 50 mL of a commercial dispersant (SediSperse A-11) operating at 35 °C with the dispersant having working density and viscosity of 0.746 g/mL and of 1.17 mPa-s, respectively. During operation, a narrow collimated beam of x-rays is used to directly measure the concentration via absorption of x-ray radiation (Beer's Law) and is used in conjunction with sedimentation theory (Stokes' Law) to the determine particle size distribution. From this technique, we are able to fully characterize the particle size distributions.

4.2 Phase Identification and Crystallite Size

4.2.1 Conventional X-Ray Diffraction

For phase identification and crystallite size measurements, an X'Pert PRO Multipurpose Powder Diffractometer from PANalytical (Almelo, Netherlands) was used. Copper K_α radiation (λ = 0.154187 nm) was generated via a copper anode operated with a voltage and current of 45 kV and 40 mA, respectively. Data was collected over the 2θ range of 5-65° for phase identification and a 2θ range of 25-50° for crystallite size measurements for the Mg and MgO phases. Scanning was performed with a 2θ step size of 0.008° for both of the 2θ ranges and a nominal scan speed of 1.2 deg./min. For data acquisition, a scanning X'Celerator detector was used with variable anti-scatter and divergent slits with a beam mask of 15 mm. A second anti-scatter slit of 2° was used to help improve the signal-to-background ratio. All scans were carried out in 'continuous' mode at room temperature.

When measuring the crystallite size for the as-SPS'ed and heat-treated samples, many small rectangular samples (4 x 4 x 2 mm) were cut from a single SPS puck to ensure any differences in samples were a result of the heat treatment, and not due to variance between SPS samples. In order to subtract the background and deconvolute Cu Kα_1 from Cu Kα_2, the software package PANalytical X'Pert HighScore Plus was used assuming a Cu Kα_1 to Cu Kα_2 ratio of 2:1. For calculating the crystallite size, the Scherrer formula [50] was used which has the form:

$$L = \frac{K\lambda}{\beta_{size} cos\theta} \qquad Equation\ 4.1$$

where L is the crystallite size, K is a dimensionless number (on the order of unity), λ is the wavelength of the radiation used, θ is the Bragg angle, and β_{size} is the line broadening or full with at half maximum (FWHM) due to the size broadening. In order to obtain the size broadening, we must first subtract all other contributions from the measured or observed broadening from the FWHM. If the peak profiles are assumed to be Lorentzian, the size broadening can be calculated from the following equation:

$$\beta_{obs.} = \beta_{size} + \beta_{strain} + \beta_{inst.} \qquad Equation\ 4.2$$

where $\beta_{obs.}$ is the total observed FHWM broadening, β_{strain} is the component of broadening due to strain, and $\beta_{inst.}$ is the inherent broadening from the instrument.

A standard value of 0.9 was chosen for K, and the FWHM values were measured from the most intense diffraction peak at approximately 2θ = 36.6° for Mg and approximately 2θ = 43.0°. For λ, the value of 0.154060 nm corresponding to Cu $K\alpha_1$ was used as $K\alpha_2$ was stripped using the PANalytical X'Pert HighScore Plus software package. Instrument broadening was calculated to be 0.07° from a standardized lanthanum hexaboride (LaB_6) powder sample, and the broadening due to strain was assumed to be negligible. When measuring crystallite size, ten separate measurements were taken for the as-received powder, cryomilled powder, as-SPS'ed sample, and all heat-treated samples heated for 100 hours (i.e. 150, 250, 350, 450 °C at 100 hours). For all other heat-treated samples (i.e. 150, 250, 350, 450 °C at 2, 4, 8, 16, 32, 64 hours), only 5 separate measurements were made. For phase identification and lattice parameter measurements, the powder diffraction files (PDFs) of 03-065-3365 and 03-065-0474 for Mg and MgO, respectively.

It should be noted with caution the distinction between crystallite size and grain size and the limitations associated with the former as measured via XRD and the Scherrer equation. For the purposes of this work, a clear distinction will be made between crystallite size and grain size. The term *crystallize size* will be confined to indirect methods of measurement such as XRD via line broadening, and the term *grain size* will used only in the context of direct measurements such as TEM (dark field images) and EBSD. The reasons for these distinctions are due to limitations of applying the Scherrer formula which will briefly be discussed. The Scherrer equation gives the average or apparent crystallite size which may or may not be equivalent to the grain size as measured by direct methods. The presence of planar defects such as stacking faults, dislocation bands, or twins may cause the crystallite size to be smaller than the grain size in some cases. In general, the crystallite size gives the lower limit or lower bound on the grain size.

In addition to these subtleties in the difference between crystallite size and grain size, there are some cases in which it is not appropriate to apply the Scherrer equation or cases in which the results from this method have no physical interpretation. These cases would be when the crystallites are too broadly distributed or the crystallites of the material are too large, having a size broadening on the order of the instrument broadening. The Scherrer equation is only appropriate when the crystallite size is narrowly distributed in a unimodal distribution. Applying this method to a bimodal crystallite size distribution would give no real physical interpretation as multimodal distributions are not adequately characterized by a single grain size and would lead to an incorrect impression of the microstructure. In relation to the size restriction, crystallite size is inversely proportional to the FWHM, meaning that the accuracy of the measurement decreases as the grain size increases due to the decrease in resolution. Even with the best laboratory instruments, Cu-based radiation techniques are only accurate for crystallite sizes below 100-200 nm [51] with 100 nm being the generally accepted lower limit cutoff for accurate measurements [52].

Despite all of these restrictions and caveats, line broadening is a powerful, easy, and widely used tool to measure crystallite size under the correct conditions and serves as a stand-alone method for estimating the grain size of a material as well as serving as an additional characterization method to supplement direct grain size measurements such as TEM and EBSD. Even if the absolute crystallite size cannot be obtained from XRD, the relative crystallite size can be used to compare samples when direct grain size measurements are uneconomical or impractical.

4.2.2 Synchrotron X-Ray Diffraction

In order to confirm our results and to ensure that there were no additional phases that went undetected by the lower brightness of the conventional XRD, samples were testing with using X-rays produced via synchrotron radiation at the SAGA Light Source (SAGA-LS) in Kyushu, Japan. SAGA-LS is a third-generation synchrotron radiation source equipped with a 1.4 GeV storage ring [53]. Testing was conducted using the BL07 beamline which uses a 4 T superconducting wiggler capable of generating hard X-rays up to 40 keV. The diffraction experiments were conducted in transmission geometry (as compared to reflective geometry for convention XRD) with X-rays having traveled through the samples prior to being detected. The synchrotron set-up is shown in Figure 4.1. For the samples, thin slices were cut from a single SPS puck roughly measuring 20 x 10 mm in cross-section and 1 mm in thickness. X-rays with energies of 25 keV ($\lambda = 0.049594$ nm) were used in order to penetrate the sample with a beam cross-sectional area of approximately 1 mm^2. During testing, Debye-Scherrer rings were recorded on a 2D PILATUS 100K detector with an area of 487 x 195 pixels with a pixel size of 172 x 172 µm. Data was collected over a 2θ range of 2-24° in three separate and slightly overlapping segments of about 7.5° with an acquisition time of 600 s for each segment. Conventional line profiles were obtained from the diffraction patterns by using an azimuthal integration of the Debye-Scherrer rings. The individual line profile datasets were combined into one overlapping dataset with the overlapping data being deleted and the background baseline subtracted using the Origin data analysis software.

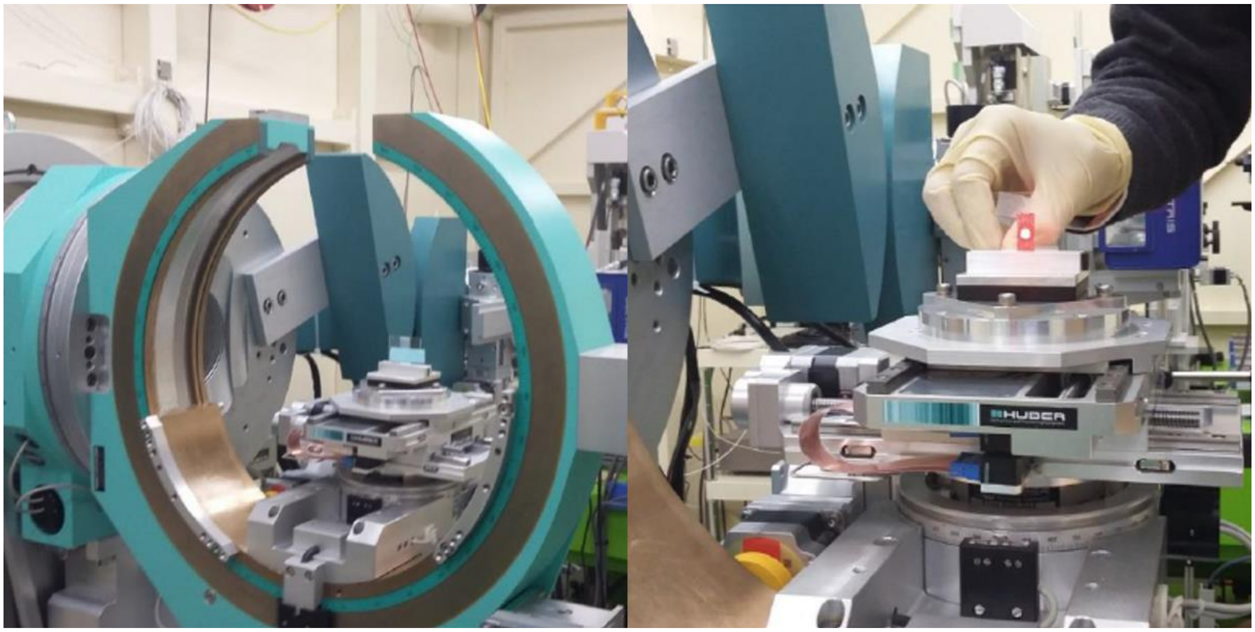

Figure 4.1: Set-up for the synchrotron XRD data collected at the SAGA Light Source (SAGA-LS) in Kyushu, Japan.

4.3 Microstructure

Several methods were used to characterize the microstructure for both the powder (both as-received and cryomilled) and bulk samples. These methods include scanning electron microscopy (SEM), transmission electron microscopy (TEM) including the more advanced scanning transmission electron microscopy (STEM), electron backscattered diffraction (EBSD), and energy-dispersive X-ray spectroscopy (EDS) which was used in combination with both the SEM and STEM. To directly characterize the grain structure of both the powder and bulk samples, TEM (specifically dark field micrographs) and EBSD were utilized. For the powder samples, only TEM was used to measure the grain size distributions. For the bulk samples, both TEM and EBSD were used. Again, it is important to distinguish grain size from crystallite size, as briefly mentioned earlier in this chapter, with grain size only referring to measurements taken from direct methods such as TEM and EBSD with crystallite size referring to data obtained using line broadening analysis from XRD (both conventional and synchrotron).

4.3.1 Scanning Electron Microscopy

The morphology, composition, and microstructure of the powders and bulk samples were investigated using an FEI Nova Nano 230 Field Emission SEM equipped with a Thermo Scientific UltraDry EDS Detector. For regular SEM images, an accelerating voltage of 10 kV. For EDS analysis including point analysis and mapping, an accelerating voltage of 20 kV with a working distance of 5 mm was used. For the preparation of powder samples, loose powders were simply pressed into carbon take with the excess powder removed with compressed air. For bulk microstructural investigations, samples were hand polished to a final polish of 0.05 μm gamma alumina powder. In order to reveal contrast, the bulk samples were slightly over polished. No etchant solutions were used to achieve this.

4.3.2 Transmission Electron Microscopy

The microstructure, specifically the grain structure, of the powders and bulk samples were investigated using an FEI Titan Field Emission S/TEM equipped with a high-angle annular dark-field (HAADF) as well as an EDS detector. For all uses (TEM, STEM, EDS), an accelerating voltage of 300 kV was used. For dark field images, the smallest objective aperture was used to isolate both the Mg and MgO diffraction rings for the purpose of isolating the grains belonging to both of these phases. For the preparation of powder samples, powders were suspended and sonicated in ethanol before transferred to the carbon side of a Formvar/carbon 200 mesh copper TEM grid and placed under vacuum to dry. For the preparation of bulk samples, the focused ion beam (FIB) *in situ* "lift-out" technique was used to selectively remove small 10 μm x 5 μm cross-sections from the bulk and then thin enough to be transparent to electrons, usually < 100 nm.

4.3.3 Electron Backscattered Diffraction

All electron backscattered diffraction (EBSD) testing was conducted by EBSD Analytical (Lehi, UT). Data was collected on a Philips XL-30 Field Emission SEM equipped with an EDAX Hikari EBSD Camera. Images were collected over a 75 x 75 μm area using a hexagonal grid sampling with a step size of 0.1 μm using an accelerating voltage of 20 kV with a beam current of 5 nA. For grain size characterization, the areas of each grain were calculated by grouping together adjacent pixels with orientations differing by less than 5°. Grain diameters were calculated assuming the area came from a circular grain. It should be noted that due to step size, grains below 100 nm were not able to be detected and these regions will be represented by the color black. Decreasing the step size would not increase grain size resolution to a large degree as EBSD is ultimately limited by the interaction volume of electrons as well as the probe diameter which are both roughly on the same order as the step size.

4.4 Mechanical Properties

4.4.1 Elastic Modulus and Hardness

Elastic modulus and hardness were both obtained via an MTS Nano Indenter XP from MTS Nano Instruments (Oak Ridge, Tennessee) equipped with the standard XP head and a Berkovich diamond indenter shown in Figure 4.2. The indentations were conducted under load-control with a constant strain rate of 0.05 s^{-1} and indented to a total indentation depth of 2,000 nm. Both the hardness and elastic modulus were simultaneously measured via the continuous stiffness measurement (CSM) method which superimposes a harmonic displacement of 2 nm at 45 Hz to produce a continuous elastic response. With the CSM, the contact stiffness was able to be continuously measured which enabled the contact depth, hardness, and elastic modulus to be calculated for all indentation depths over the 2,000 nm range as opposed to a conventional or non-CSM method which only obtains one result for both the elastic modulus and hardness at one particular indention depth upon unloading. For each indentation using the CSM method, an average elastic modulus and hardness were calculated over the indentation depth from 200 to 1,800 nm, disregarding the initial and final loading portions of the curve. For each test condition, one of the square samples used in the crystallite measurements was chosen for testing. For the as-SPS'ed sample and all of heat-treated samples heated for 100 hours (i.e. 150, 250, 350, 450 °C at 100 hours), 50 indentations were performed. For all other test conditions, 25 indentations were made with indentations being spaced 250 μm apart (center-to-center) with a lateral distance of the indentations having an approximate length of 15 μm at the maximum indentation depth of 2,000 nm.

In order to understand how the elastic modulus and hardness are calculated in nanoindentation, we first have to look to the seminal work of Oliver and Pharr [54] who were able to derive a formula for calculating the contact depth based on both the maximum load measured at full indentation depth and the sample stiffness [55], with the contact depth always being less than the indentation depth due to compliance in the substrate assuming a rigid indenter tip. These results were only possible due to initial work done by Sneddon [56] who provided a solution to the axisymmetric Boussinesq problem, providing a simple formula for the depth of penetration of a punch of arbitrary profile into an elastic half space. Oliver and Pharr would later build upon this initial work by Sneddon, making it possible for the direct and simultaneous measurement of both elastic modulus and hardness from simple indentation based on the applied load and indentation depth of the indenter tip.

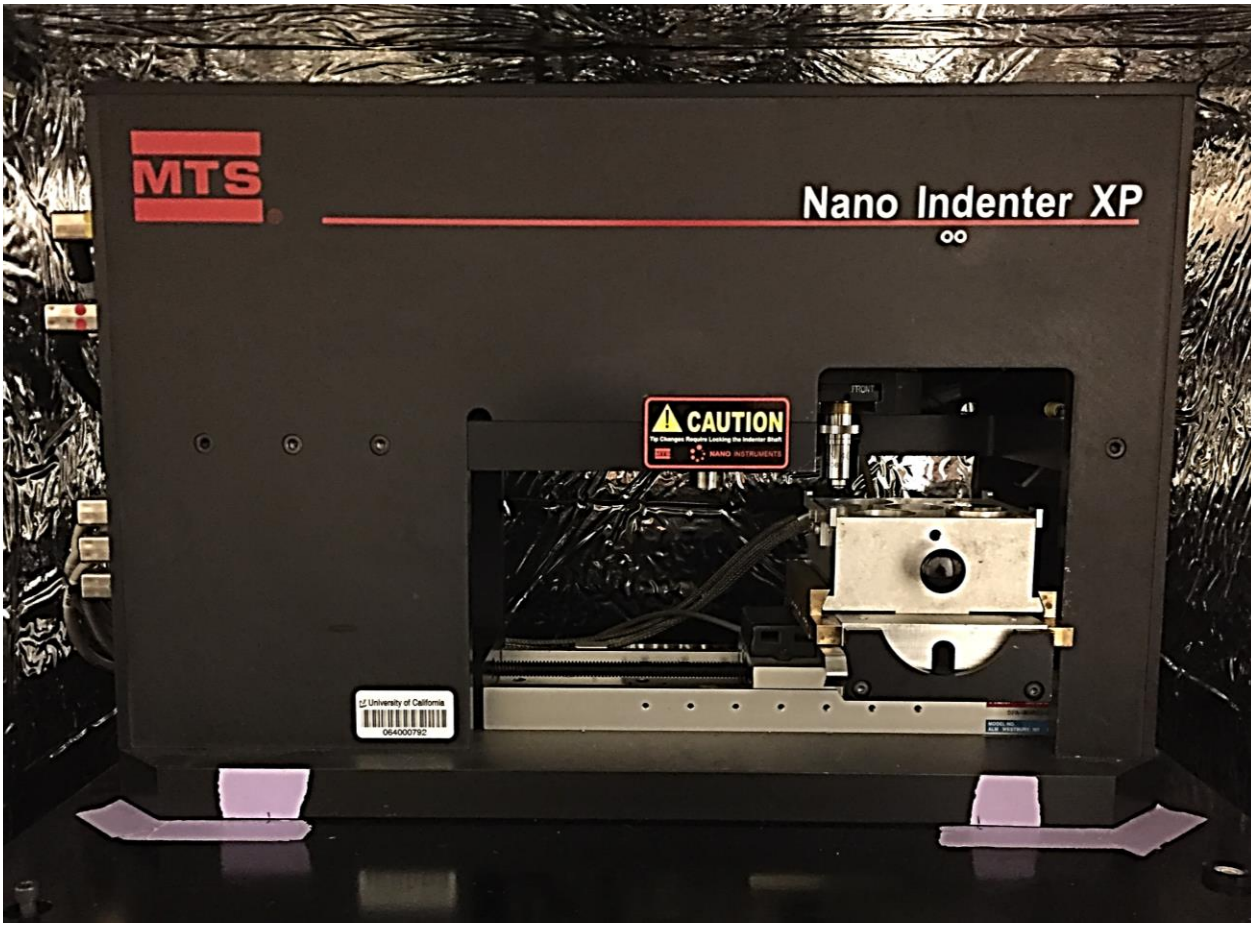

Figure 4.2: MTS Nano Indenter XP from MTS Nano Instruments (Oak Ridge, Tennessee) equipped with the standard XP head and a Berkovich diamond indenter for the measurement of elastic modulus and hardness.

As just mentioned, the work by Oliver and Pharr was fundamental for the ability to acquire the elastic modulus and hardness of a given material at a particular depth. This field of study eventually became known as *nanoindentation* and was based on the formation of Oliver and Pharr to calculate the contact depth that an indenter tip made when penetrating a material with a specific indenter geometry. This equation is given below in Equation 4.3:

$$h_c = h_{max} - k\frac{P_{max}}{S} \qquad Equation\ 4.3$$

where h_c is the contact depth, h_{max} is the full or maximum indentation depth, k is a constant dependent on the indenter geometry which is equal to 0.75 for a Berkovich tip, P_{max} is the maximum load at the maximum indentation depth, and S is the stiffness of the material as calculated from the elastic unloading region of the load vs. displacement curve (dP/dh). Once the contact depth is known, the projected contact area can be calculated according to Equation 4.4:

$$A_{c\ proj.}(h_c) = 3\sqrt{3}\ h_c^2\ tan^2 65.27° = 24.5\ \mathrm{h}_c^2 \qquad Equation\ 4.4$$

which is simply derived from the indenter tip which in this particular case is the Berkovich indenter tip which is a three-sided equilateral pyramid with a total included angle of 142.3° and a half angle of 65.27° [57,58]. It should be noted that the Berkovich geometry was set up in such a way as to have the same projected area-to-depth ratio as the Vickers indenter. It also should be noted that the projected contact area function given in this equation is for a perfect indenter geometry, and for actual indenters additional terms are added to this function to correctly account for imperfections such as rounding of the indenter tip. These additional area function terms are determined through indentation of a calibration material, typically fused silica, in which the material properties are known.

With both the stiffness and the projected contact area between the indenter tip and the material known, the reduced elastic modulus can be calculated from a relationship that was presented in the original Sneddon analysis which is modified with the addition of a constant β term which accounts for the indenter tip having a different boundary condition than the one assumed by Sneddon [55], mainly that the indenter tip used in testing (almost always diamond) is not perfectly rigid as in the analysis done by Sneddon. This reduced elastic modulus equation is given below in Equation 4.5:

$$E_r = \frac{\sqrt{2}}{2\beta} \frac{S}{\sqrt{A_{c\,proj.}}} \qquad Equation\ 4.5$$

with a β value of 1.0 used in the case for the Berkovich indenter tip.

And finally, with these concepts and equations, the equations to calculate the elastic modulus and hardness can finally be presented with the elastic modulus being calculated from Equation 4.6 and the hardness being calculated from Equation 4.7:

$$\frac{1}{E_r} = \frac{1-\nu_s^2}{E_s} + \frac{1-\nu_i^2}{E_i} \qquad Equation\ 4.6$$

$$H = \frac{P_{max}}{A_{c\,proj.}} \qquad Equation\ 4.7$$

where E_r is the reduced elastic modulus, E_s is the elastic modulus of the test specimen, E_i is the elastic modulus of the indenter, ν_s is the Poisson's ratio of the test specimen, ν_i is the Poisson's ratio of the indenter, and H is the hardness of the test specimen. For a diamond indenter tip, ν_i and E_i are 0.07 and 1,141 GPa [59], respectively.

4.4.2 Compressive Yield Strength

Two different characterization methods were used to determine the compressive yield strength of the as-SPS'ed sample. Those two characterization methods being bulk compression via conventional bulk compression testing and microcompression with micropillars prepared via focused ion beam (discussed in next section). Bulk compression testing was conducted using an Instron SATEC 5590 Series static hydraulic testing machine with cylindrical samples cut from the SPS puck measuring approximately 6 mm in diameter and 6 mm in height. Five compression tests were performed with a nominal strain rate of 2 x 10^{-3} s^{-1}. Microcompression testing was conducted using a Hysitron PI 85 *in situ* SEM PicoIndenter shown in Figure 4.3 with micropillars prepared via focused ion beam (discussed in next section). Similarly, five microcompression tests were performed on micropillars approximately 4 μm in width and approximately 12 μm in height under displacement-control with a displacement rate of 20 nm/s and an effective strain rate of 2 x 10^{-3} s^{-1}. The microcompression process of the micropillars is shown in Figure 4.4 with an SEM image of the indenter tip in contact with the micropillar just prior to compression in Figure 4.4(a) and an SEM image showing the indenter withdrawn from the micropillar following compression, and ultimate fracture, of the micropillar in Figure 4.4(b).

Due to the fact that there was excellent agreement between the compressive yield strength obtained from both the bulk compression and microcompression testing and due to a limitation in the overall quantify of samples, microcompression was only used to characterize the yield strength of heat treated samples with high confidence that microcompression testing was an accurate analogue for calculating the bulk compressive yield strength. Also, due to the fact that there was no discernable difference between the hardness values of the as-SPS'ed sample and any of the heat-treated samples as determined by nanoindentation, microcompression testing was only performed on the sample heat-treated at 450 °C for 100 hours as this was the most aggressive of the heat treatments carried out. It was assumed that if there was no difference in compressive yield strength as determined by microcompression between the as-SPS'ed sample and the sample heat-treated at 450 °C for 100 hours, microcompression tests for the other numerous heat treatment conditions would be unnecessary.

When calculating the compressive yield strength from the microcompression data, it is important to note that certain modifications to the raw displacement data were performed due to compliance of the substrate, and to a much lesser degree, the compliance of the indenter tip which result in an overestimation of the strain in the pillar during compression. The overall relationship between the total measured displacement and separate components of compliance is given below in Equation 4.8:

$$x_{total} = \Delta x_{ind.} + \Delta x_{pillar} + \Delta x_{sub.} \qquad \textit{Equation } 4.8$$

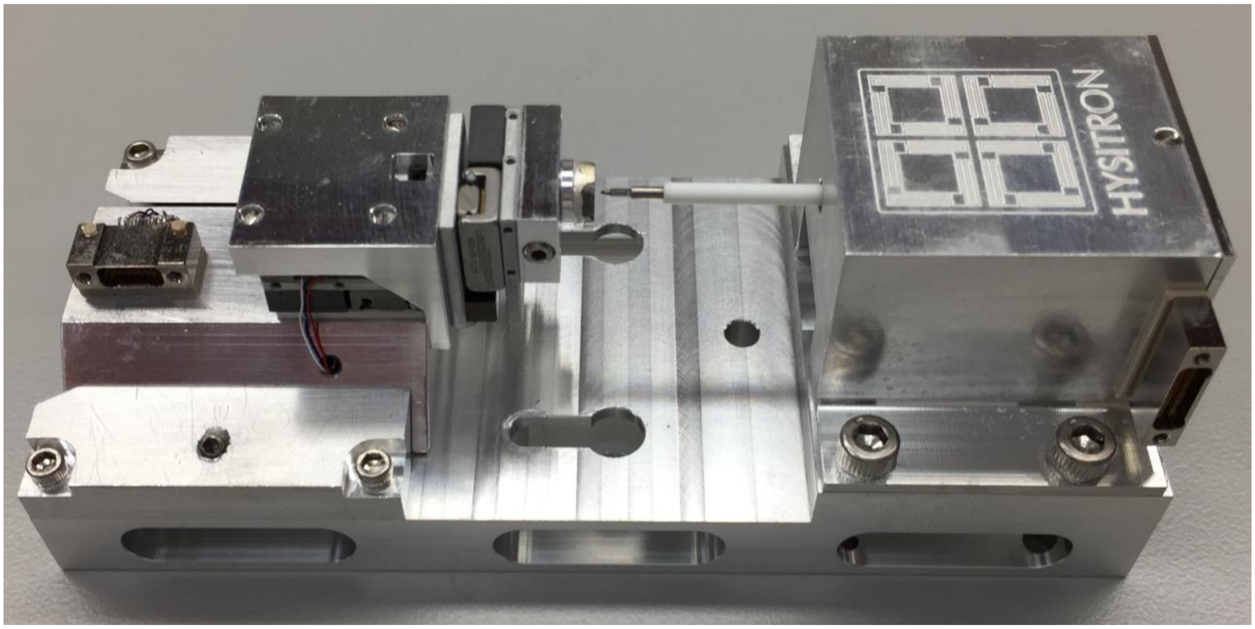

Figure 4.3: Hysitron PI 85 *in situ* SEM PicoIndenter for use in microcompression of the micropillars prepared via FIB.

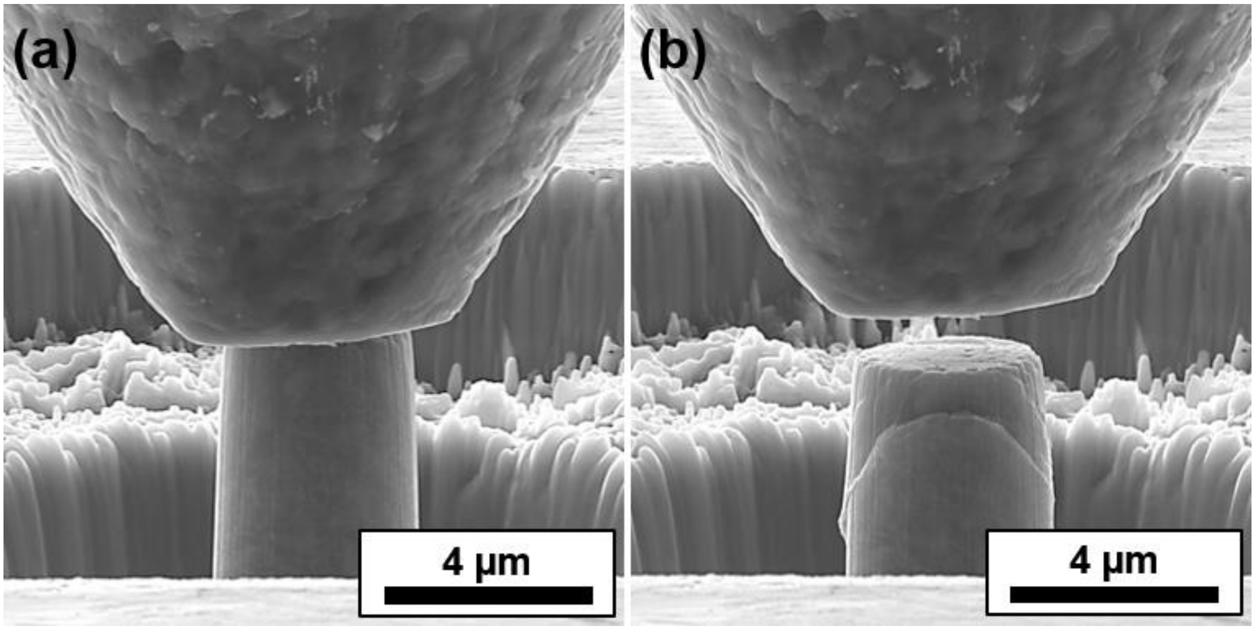

Figure 4.4: SEM images of the micropillar compression testing via the Hysitron PI 85 *in situ* SEM PicoIndenter with (a) the diamond indenter tip in contact with the top of the micropillar prior to compression and (b) the diamond indenter tip withdrawn after compression the micropillar to failure.

which shows that the total measured displacement (x_{total}) is simply a linear summation of the compliance due to the indenter ($\Delta x_{ind.}$), compliance due to the pillar (Δx_{pillar}), and compliance due to the substrate ($\Delta x_{sub.}$). This modification is unique to micropillar compression, where the compliance of the substrate can be considerable and can significantly affect the displacement and thus the strain data. The initial work, again, was done by Sneddon which was later adopted for the use in micropillar compression [60,61] to give the total displacement in just the pillar in the relation given below in Equation 4.9:

$$\Delta x_{pillar} = x_{total} - \frac{\left(1 - \upsilon_{ind.}^2\right)}{E_{ind.}} \frac{P_{meas.}}{d_{top}} - \frac{\left(1 - \upsilon_{sub.}^2\right)}{E_{sub.}} \frac{P_{meas.}}{d_{bot.}} \qquad Equation\ 4.9$$

where $\nu_{ind.}$ and $\nu_{sub.}$ are the Poisson's ratio for the indenter and substrate, respectively, $E_{ind.}$ and $E_{sub.}$ are the elastic modulus of the indenter and substrate, respectively, $P_{meas.}$ is the measured load on the micropillar, and d_{top} and $d_{bot.}$ are the pillar diameters measured at the top of the pillar and the bottom (or base) of the pillar, respectively.

Using the raw displacement data without making this modification will lead to an overestimation of the strain in the pillar which will lead to an overestimation in the modulus. It should, however, not have a significant impact on the yield strength due to the fact that the 0.2% offset method for determining yield strength is not very sensitive to this effect. When calculating this displacement correction for the as-SPS'ed and heat-treated samples, an elastic modulus of 60 GPa, as calculated from nanoindentation, was used along with an assumed Poisson ratio of 0.3. With these values and the values for the diamond indenter tip, it was shown that the pillar displacement during micropillar compression accounted for approximately 85% of the total overall displacement.

4.5 Pillar Fabrication

In order to prepare the micropillars for microcompression, FIB was utilized for micropillar fabrication using an FEI Nova 600 Nano Lab Dual Beam SEM/FIB with a gallium source. Prior to fabrication, samples were tilted to 52° relative to the electron beam such that the ion beam (Ga+ ions) was normal to the sample surface. During fabrication, an ion beam accelerating voltage of 30 kV with various beam currents (or spot sizes) being used. The micropillar fabrication process followed four primary fabrication steps in order to achieve a micropillar with a nominal diameter of about 4 μm with an aspect ratio (height-to-diameter) of 3:1. Milling was performed in an annular fashion with disks of various sizes being used with ever decreasing diameters. This annular fabrication sequence is documented in Table 4.1 which outlines the four sequences along with the beam current and annular disc diameters.

Table 4.1: Annular FIB sequence for the fabrication of 4 μm micropillars.

Step	**Outer dia. (μm)**	**Inner dia. (μm)**	**Current (nA)**	**Beam dia. (nm)**
1	35	15	20	~400
2	17	8	20	~400
3	9	5	5	~100
4	5.5	4	1	~50

This fabrication sequence is also visually presented in Figure 4.5 in which each step in Table 4.1 is shown with SEM images. From this sequence of images, the overall pillar fabrication is shown in which the micropillar is milled out of the bulk material with ever decreasing probe currents until a pillar is formed with only a slight taper. Also present in these SEM images is a "viewing window" that is milled into the sample in order to accurately monitor and measure the overall progress and height of the pillar during fabrication. This window is also useful for viewing deformation of the micropillar during microcompression. A complete summary of the pillar geometry including pillar diameters, height, aspect ratio, and taper angle is given in Table 4.2 along with a higher magnification SEM image of a single micropillar as-fabricated by FIB in Figure 4.6.

Table 4.2: Summary of pillar geometrical parameters of all pillars fabricated by FIB.

Geometrical parameter	**Avg. ± std. dev.**
Top diameter:	3.57 ± 0.05 μm
Median diameter*:	4.15 ± 0.04 μm
Bottom diameter:	4.83 ± 0.12 μm
Height:	12.49 ± 0.05 μm
Aspect ratio:	3.01 ± 0.24
Taper angle:	1.51 ± 0.13°

* Measured at half the pillar's height.

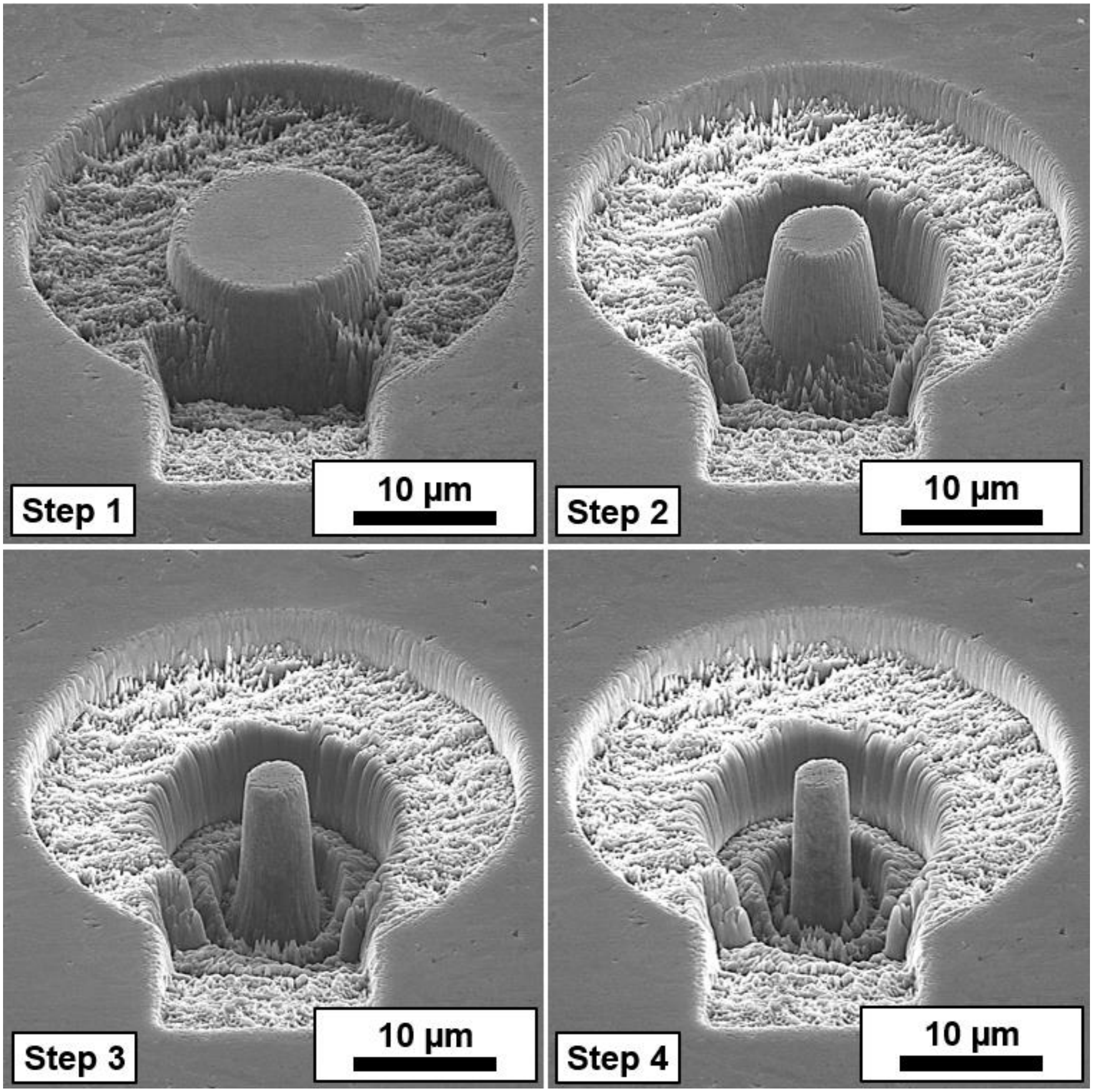

Figure 4.5: SEM overview of the annular FIB sequence used for the fabrication of 4 μm micropillars as outlined in Table 4.1. Stage is tilted 52° degrees relative to the electron beam.

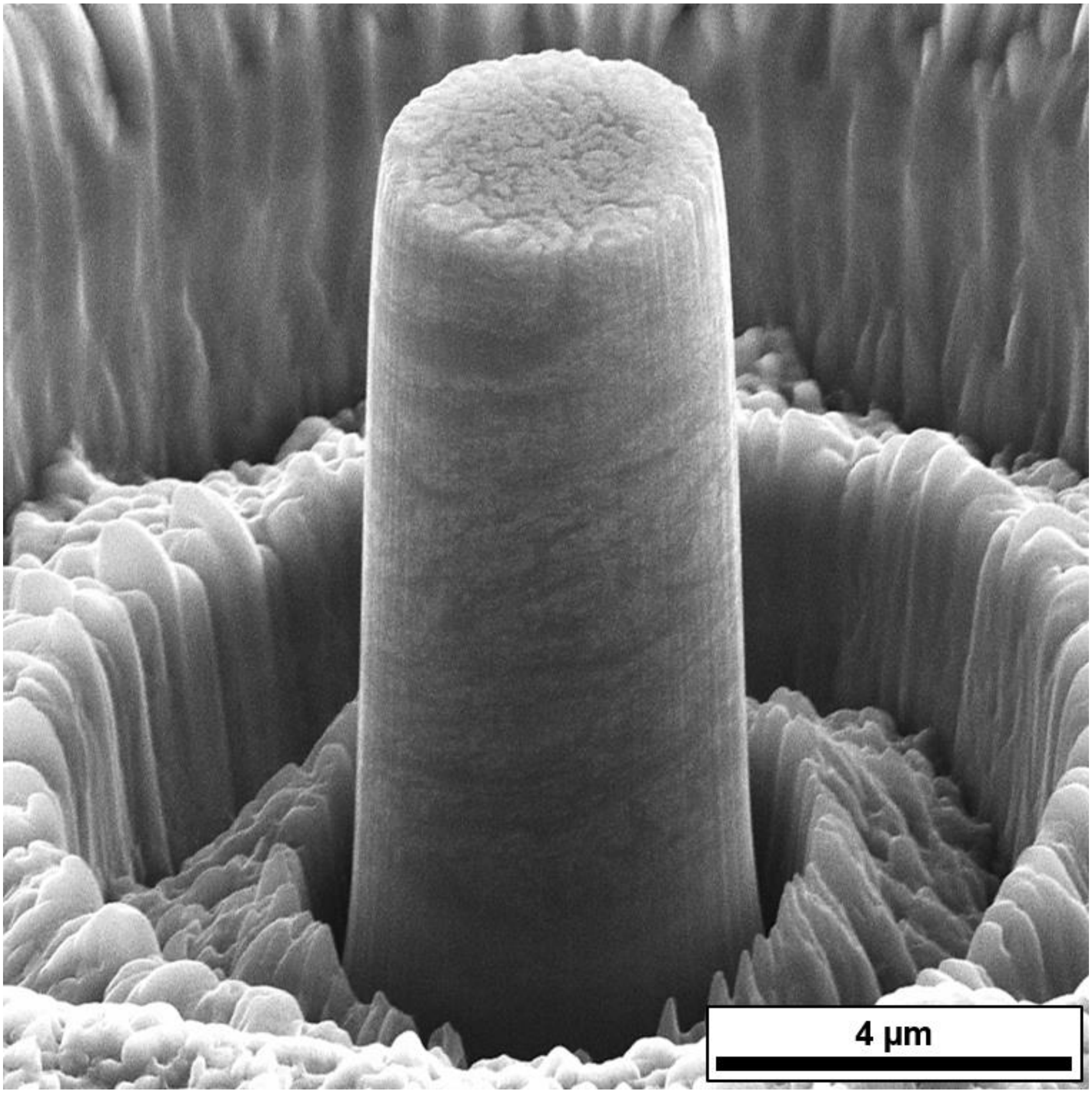

Figure 4.6: SEM image of a single micropillar as fabricated by FIB with the stage tilted 52° degrees relative to the electron beam.

Chapter 5

Characterization of As-Received and Cryomilled Powders

5.1 Particle Size and Composition

Figure 5.1 shows two side-by-side scanning electron microcopy (SEM) images of both the as-received WE43 powders and the powders after the cryomilling process. From these SEM images, the as-received powders generally appear round in shape due to the gas atomization process in which the molten metal is sprayed and rapidly quenched. This process, as previously mentioned, also involved an intentional passivation process, introducing a thin oxygen-rich passivation layer on the surface of the particles. After cryomilling, the powders show a faceted morphology indicative of the ball milling process where the particles are repeatedly welded and fractured. It is assumed that the passivation layer is mechanically broken up and incorporated into the bulk of the cryomilled powders. There does not appear to be any elongation in the cryomilled powders which sometimes occurs when powders are not adequately milled. From a simple visual inspection of the SEM images, there does not seem to be any significant difference in particle size distribution between both sets of powders. This is confirmed with the results from the SediGraph which shows that volume mean diameter of the as-received powder and cryomilled powders are 19.6 ± 11.6 μm and 17.9 ± 6.8 μm, respectively.

The complete particle size data is presented in Table 5.1. These results suggest that there was no significant issue with agglomeration during milling and show that the cryomilled powders slightly narrowed in their size distribution compared to the as-received powders. In addition, the Sedigraph results indicate that the -325 mesh (i.e. particle size below 45 μm) for the as-received powders was accurate with a D90 value of 35 μm, indicating that 90% of the powder's cumulative mass is below this particle size.

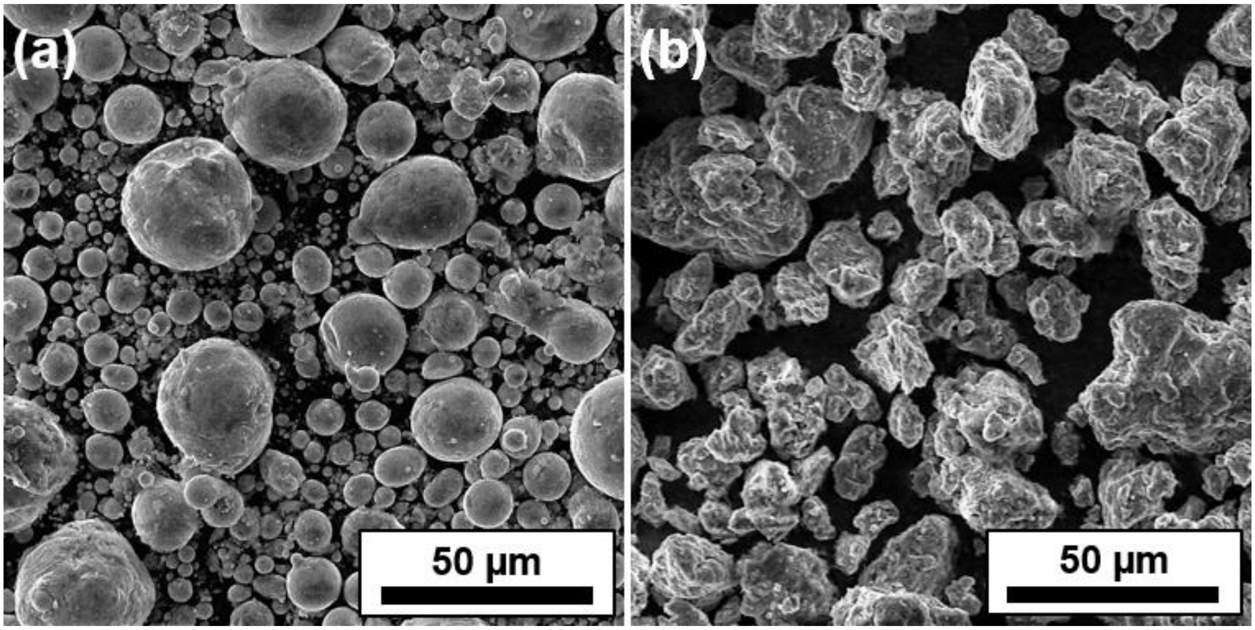

Figure 5.1: Scanning electron microscopy (SEM) images of (a) the as-received powder and (b) the cryomilled powder.

Table 5.1: Particle size distributions of the as-received and cryomilled powders as measured via SediGraph.

	Mass division diameters*			**Avg. particle diameters†**		**Span‡**
	D10 (μm)	D50 (μm)	D90 (μm)	D[1,0] (μm)	D[4,3] (μm)	
As-Received pwd.	4.4	17.1	35.4	4.8 ± 2.5	19.6 ± 11.6	1.8
Cryomilled pwd.	6.3	15.9	32.0	9.2 ± 4.3	17.9 ± 6.8	1.6

* Represent the particle size in which the stated value (in percent) of the powder's cumulative mass falls below.
† D[1,0] and D[4,3] are the number and volume averages, respectively.
‡ (D90-D10)/D50

In addition to particle size, the chemical composition was verified by energy dispersive X-ray spectroscopy (EDS) which was in good agreement with the certificate of analysis provided by the manufacturer (see Chapter 3 for this analysis). A complete summary of the EDS analysis is presented in Table 5.2 which gives both the weight and atomic percentages of Mg and each of the major alloying elements. The RE elements identified were Nd, Gd, and Dy with Nd being the main RE alloying element comprising approximately 75% by weight of the total RE elements (compared to about 70% as stated from the certificate of analysis). Besides the main alloying elements (i.e. Y, Nd, Gd, Dy, and Zr), no other impurity elements were detected, indicating low impurity levels. Oxygen, however, was detected and calculated to be about 1 wt.%. The presence of oxygen is most likely due to the thin passivation layer formed on the surface of the particles during the passivation process.

Table 5.2: Chemical analysis of the as-received powder as measured by energy dispersive X-ray spectroscopy (EDS).

	Mg	**Y**	**Total RE**	**(Individual RE)**	**Zr**	**O**
wt. %	90.04 ± 0.34	4.02 ± 0.06	3.75 ± 0.13	Nd: 2.90 ± 0.06 Gd: 0.37 ± 0.03 Dy: 0.48 ± 0.04	1.16 ± 0.06	1.03 ± 0.05
at. %	96.17 ± 0.36	1.17 ± 0.02	0.66 ± 0.03	Nd: 0.52 ± 0.01 Gd: 0.06 ± 0.01 Dy: 0.08 ± 0.01	0.33 ± 0.02	1.67 ± 0.04

Although Zr was identified in the quantified EDS data with a value of 1.16 wt. % and is close to the value reported from the manufacturer (0.56 wt. %), the proximity of the characteristic Lα line energy for Zr (2.042 keV) to that of the Lα line energy for Y (1.922 keV) makes it difficult to ascertain the accuracy of the values for Zr considering the Y signal at this energy dominates the signal of Zr due to the fact that Y has a much higher weight percentage in this alloy compared to Zr. In order to confirm the presence and accuracy of the Zr semi-quantitative data, higher energy values for the electron beam accelerating voltage would be required since it is only at higher energies that the energy lines between these two elements becomes large enough to uniquely distinguish them. However, the highest energies capable of the SEM were unable to generate adequate signal to achieve this. Therefore, the Zr semi-quantitative data along with the Zr elemental mapping (presented in Chapters 6 and 7) should be viewed with uncertainty, with this data not being omitted.

Table 5.3 shows the complete EDS analysis for the cryomilled powders which shows approximately a tenfold increase in the oxygen content with the cryomilled powders consisting of about 13 wt. % compared to about 1 wt. % for the as-received powders. This oxygen uptake is a bit surprising considering one of the reported benefits of the cryomilling process has been the decrease in powder oxidation compared to conventional ball milling. However, there does seem to be conflicting reports in the literature with some results [62,63] reporting significant oxygen uptake in cryomilled powders with the authors mostly attributing this effect to *ex situ* oxidation of the powders after the cryomilling process and not a direct result of the cryomilling process. From EDS analysis alone, it is unclear as to whether this tenfold increase in oxygen of the cryomilled process was a result of *in situ* oxidation or a result of *ex situ* oxidation with the cryomilled powders being more susceptible to oxidation with the native oxidation layer no longer passivating the powders. It is reasonable to expect that the cryomilled powders are more susceptible to oxidation after the cryomilling process, and that some oxidation of the powders occurred after cryomilling during transport outside of the glovebox for characterization and for consolidation. However, it is unlikely that oxidation after cryomilling could explain the significant percentage of oxygen considering the native passivation layer on the as-received powders only accounted for about 1 wt. %. Further analysis will need to be provided in order to ascertain the source of this oxidation and in order to determine in which phase(s) the oxygen is present.

Table 5.3: Chemical analysis of the cryomilled powder as measured by EDS.

	Mg	**Y**	**Total RE**	**(Individual RE)**	**Zr**	**O**
wt. %	79.79 ± 0.30	3.31 ± 0.02	3.41 ± 0.20	Nd: 2.63 ± 0.09 Gd: 0.35 ± 0.05 Dy: 0.43 ± 0.06	0.63 ± 0.05	12.86 ± 0.05
at. %	79.03 ± 0.29	0.90 ± 0.01	0.55 ± 0.03	Nd: 0.44 ± 0.01 Gd: 0.05 ± 0.01 Dy: 0.06 ± 0.01	0.17 ± 0.01	19.35 ± 0.07

5.2 Phase Identification and Crystallite Size

5.2.1 Conventional X-Ray Diffraction

Conventional X-ray diffraction (XRD) was used to characterize the phases, lattice parameters, and crystallite size for both the as-received as well as cryomilled powders. XRD spectra for both powders are presented in Figure 5.2. It should be noted that the units for intensity are given in a logarithmic scale. The relevant lattice constants and crystallite sizes calculated from the XRD spectra are also given in Table 5.4.

For the as-received powders, besides Mg the largest phase detected was a Mg_3RE intermetallic phase where RE can represent a solid solution of differing rare earth elements (i.e. Nd, Gd, Dy, etc.) along with Y due to its similar metallic radius. Due to the rapid quenching of the powders during the gas atomization process, this intermetallic phase is most likely a non-equilibrium phase with reported equilibrium phases of $Mg_{41}Nd_5$ [64] and $Mg_{12}Nd$ [65] at temperatures near the melt temperature. Besides this intermetallic phase, the only other phases present in the as-received powders are trace amounts of yttrium (α-Y) and yttrium oxide (Y_2O_3) with the yttrium oxide probably serving as the protective oxide layer during the passivation process just after gas atomization. It is also important to note that there is no presence of magnesium oxide in the as-received powders indicating a preferential reaction with Y or RE elements during the passivation process. This is most likely a result of Y and RE elements segregating to the molten surface of the powder particles prior to solidification and passivation which resulted in the creation of Y_2O_3 and the absence of MgO. There does not seem to be any noticeable difference between the lattice parameters of the as-received powders compared to the Mg reference values which indicates low solubility of Y or RE elements in α-Mg. The solubility of RE elements in Mg is quite low, usually less than a few atomic percent at room temperature due to the large atomic mismatch between the RE elements and Mg, supporting this conclusion. The measured Mg crystallite was found to be 95 ± 5 nm as measured by the Scherrer equation which may or may not hold any significance as previously discussed at length in the previous chapter.

After the cryomilling process, three major observations are made from the XRD results of the cryomilled powders. These observations being: (1) the Mg_3RE intermetallic compound is eliminated, (2) the magnesium crystallites have become nanocrystalline with a measured crystallite size of 18 ± 2 nm, and (3) the introduction of a nanocrystalline MgO phase with a crystallite size of 2 ± 1 nm. As previously stated, the intermetallic compound present in the as-received powders was a non-equilibrium phase due to the rapid solidification during the atomization process which makes is not so surprising that this phase is no longer present after cryomilling. In addition to the elimination of the intermetallic compound, it is also apparent that the yttrium and yttrium oxide have essentially been reduced to peak intensities just above the background level, although it is difficult to tell if yttrium is still present due to the large broadening of the Mg peaks. The transformation of the Mg phase into nanocrystallites is not surprising as this was the ultimate goal of the cryomilling process. As previously mentioned, the introduction of oxygen during the cryomilling process was surprising. But it is apparent that almost all of the oxygen introduced into the cryomilled powders is present in the form of MgO with negligible amounts of oxygen in Y_2O_3.

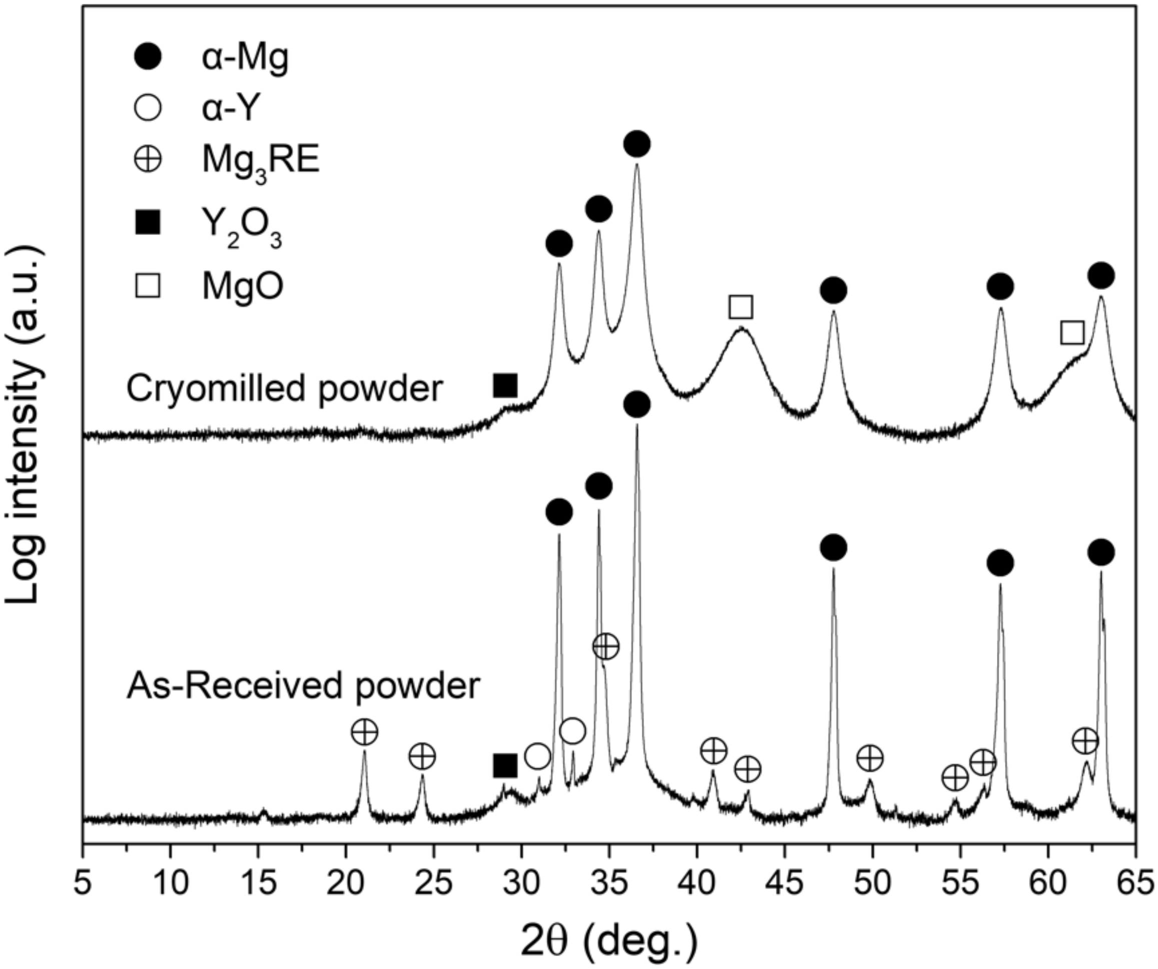

Figure 5.2: Conventional X-ray diffraction (XRD) spectra for both the as-received and cryomilled powders.

Table 5.4: Relevant lattice constants and crystallite sizes as calculated from the conventional XRD spectra for the as-received and cryomilled powders given in Figure 5.2.

	Mg Lattice Parameters			**Crystallite size (nm)**	
	a (nm)	c (nm)	c/a	Mg	MgO
As-Received pwd.	0.3215 ± 0.0004	0.5210 ± 0.0005	1.621 ± 0.003	95 ± 5	-
Cryomilled pwd.	0.3213 ± 0.0004	0.5212 ± 0.0003	1.622 ± 0.003	18 ± 2	2 ± 1
Pure Mg	0.3209	0.5210	1.624	-	-

5.2.2 Synchrotron X-Ray Diffraction

Figure 5.3 shows the synchrotron XRD spectra for both the as-received and cryomilled powders conducted at the SAGA Light Source in Kyushu, Japan. The lower 2θ values compared to conventional XRD is the result of a smaller wavelength of x-rays which decreases the diffraction angles according to Bragg's Law. The synchrotron XRD spectra confirms the presence of both the Mg and MgO phases. There are, however, some additional phases that the synchrotron radiation was able to pick up. Unfortunately, these extra phases could not be identified. Intermetallic compounds between Mg and RE elements were ruled out as possibilities for these phases as these intermetallic compounds are largely known and documented in the literature. The first of these unknown phases appears in both the as-received and cryomilled powders with a single observable peak just below 5°. The second unknown phase appears in the cryomilled powders with the three most intense peaks (assuming these come from a single phase) occurring below 5°.

Table 5.5 gives the Mg lattice parameters and calculated crystallite size for both the Mg and MgO phases. The lattice parameters as calculated by the synchrotron radiation are a little smaller compared to the values as calculated from conventional XRD, but are largely in agreement and do not show much deviation from the values for pure Mg. The crystallite size of Mg for the as-received powder is calculated to be 50 nm which is almost half the value as calculated by conventional XRD with a crystallite size of 95 ± 5 nm. There does not seem to be much agreement between the Mg crystallite size of the as-received powder for the conventional and synchrotron XRD, but this is not too surprising since the grain size for the as-received powder is probably not narrowly distributed which makes the crystallite size unreliable. The crystallite sizes of the cryomilled, however, are in much better agreement with Mg and MgO having a crystallite size of 18 ± 2 nm and 2 ± 1, respectively. The phases in the cryomilled powder are expected to be nanocrystalline which are much narrower and more reliably characterized by the crystallite size.

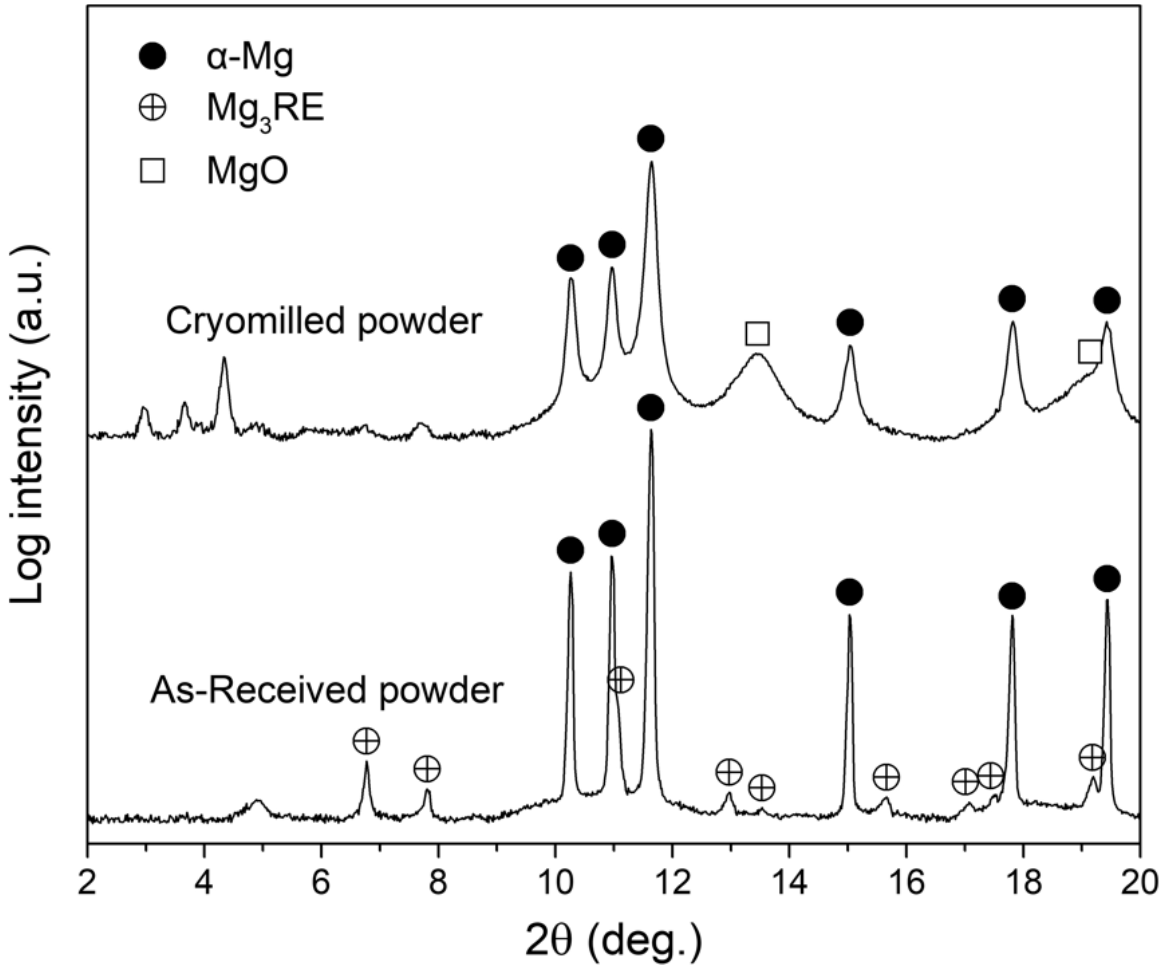

Figure 5.3: Synchrotron XRD spectra for both the as-received and cryomilled powders.

Table 5.5: Relevant lattice constants and crystallite sizes as calculated from the synchrotron XRD spectra for the as-received and cryomilled powders given in Figure 5.3.

	Mg Lattice Parameters			**Crystallite size (nm)**	
	a (nm)	c (nm)	c/a	Mg	MgO
As-Received pwd.	0.3204	0.5188	1.619	50	-
Cryomilled pwd.	0.3202	0.5189	1.621	17	3
Pure Mg	0.3209	0.5210	1.624	-	-

5.3 Microstructure

In order to investigate the microstructure and to more accurately characterize the grain structures of both the as-received and cryomilled powders, both scanning transmission electron microscopy (STEM) and traditional TEM techniques were used. Figure 5.4 shows a STEM image of a single as-received powder particle along with other STEM images of selected magnifications generated from a high-angle annular dark-field (HAADF) detector. This means that any electrons detected by the HAADF detector have been scattered to very high angle just by the nature of how the signal is selected by the detector. This scattering is achieved mainly from atomic scattering which is dependent on the atomic number (Z) of the individual atoms with heavier elements producing more scattering. This ability of heavier elements to scatter more of the electron beam means that elements with larger Z values will generate more of a signal in HAADF than smaller Z elements. This difference in scattering leads to HAADF producing images with contrast mostly attributed to difference in Z, or Z-contrast.

It is clear from the high Z-contrast shown in the STEM HAADF image in Figure 5.4(a) that the fast cooling of the gas atomization process has resulted in the segregation of the RE elements to the grain/cell boundaries where the intermetallic phases ultimately precipitated. This segregation is highlighted in both Figure 5.4(b) and Figure 5.4(c) where the higher brightness indicates more scattering due to higher Z-containing elements. Individual grains of the intermetallic phase can be seen in both of these images with the grains becoming more apparent at higher magnification in Figure 5.4(c). There is also the presence of a yttrium-rich oxide, as indicated by STEM-EDS, serving as a passivation layer on the particle surface as seen in Figure 5.4(d) which is the interface of two adjoining powder particles of around 10 nm in thickness. It is important to note that the thicker high-contrast material surrounding the powder particle is platinum which was deposited during the FIB process and is not the oxide layer.

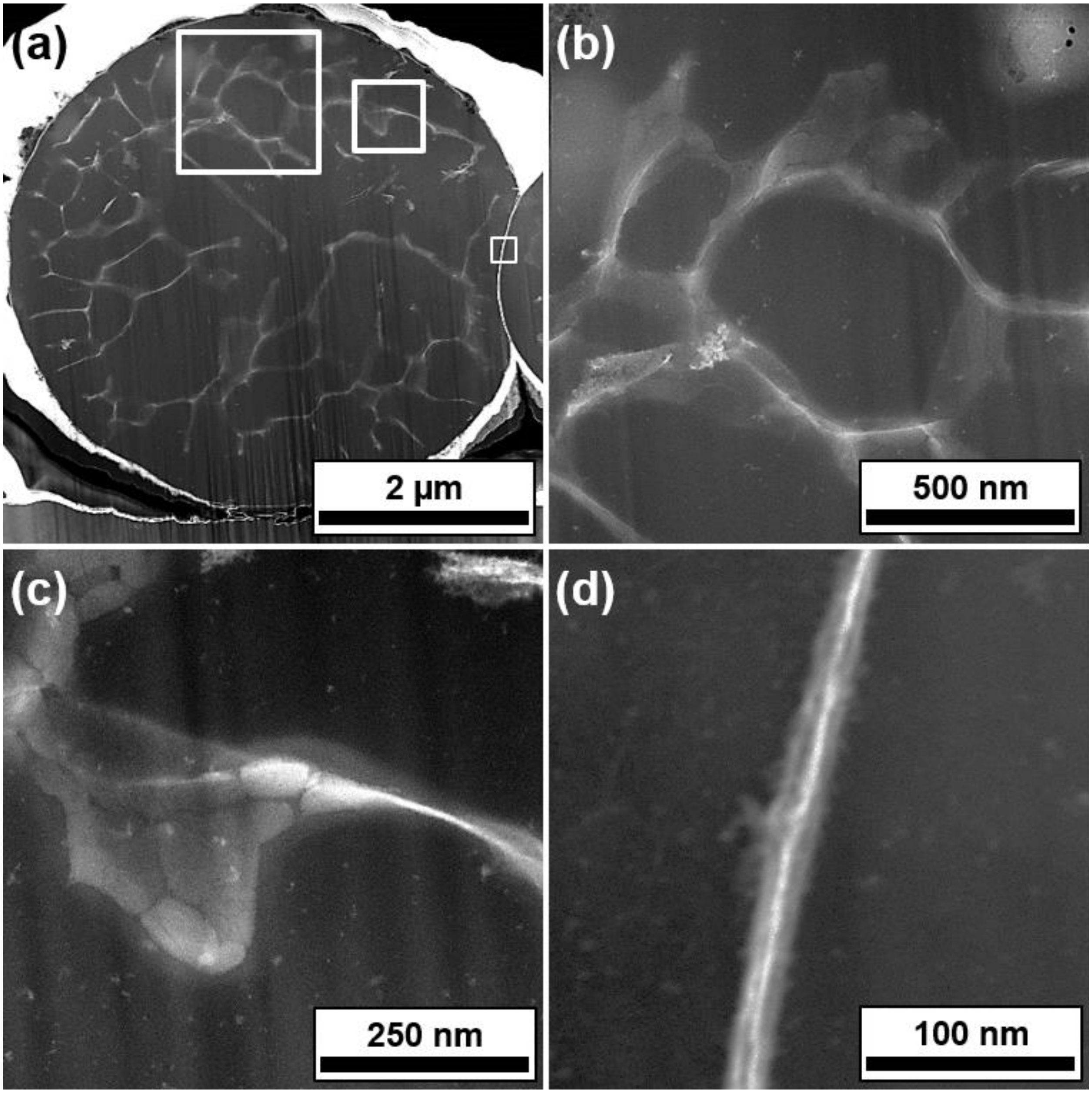

Figure 5.4: Scanning transmission electron microscopy (STEM) high-angle annular dark-field (HAADF) images showing (a) an entire as-received powder particle prepared by focused ion beam (FIB), (b) a magnified portion showing the segregation of RE elements to the cell boundaries, (c) a magnified section showing intermetallic sub grains, and (d) a magnified section showing the passivation layers between two adjoining powder particles.

TEM was also utilized in order to investigate the microstructure of the cryomilled powders. This time, however, selected area diffraction (SAED) was used in order to identify phases and the use of complementary bright-field (BF) and dark-field (DF) techniques were used in order to provide direct and complete grain size characterization. For reference, BF TEM images are generated by placing an aperture in the back focal plane of the objective lens, otherwise known as an “objective aperture,” which only allows the direct beam to pass through, thus generating an image mostly with mass-thickness and diffraction contrast. DF TEM images, on the other hand, are generated by placing the objective aperture around one or more of the diffracted beams, which only allows the diffracted beam or beams to pass through, thus generating a highly selected image which can only include particular grains of a particular orientation.

Such analysis was done on several cryomilled powder particles with one of these powder particles with the complete analysis being shown in Figure 5.5. A BF TEM image of the single cryomilled particle is shown in Figure 5.5(a) as well an indexed SAED pattern in Figure 5.5(b) along with the accompanying table which identifies each phase, plane, and lattice constant. From the indexed SAED patterns in along with the accompanying table, Mg and MgO are the only two phases present which confirms the results of XRD. In order fully characterize these two phases individually, the smallest objective aperture was used in conjunction with the SAED rings in order to isolate the different phases and generate DF images of selected composition. Due to the size restriction of the objective aperture as shown in Figure 5.5(b) with the black and white circles, it was impossible to completely isolate MgO due to the particular arrangement of the SAED rings in relation to Mg. There was no such issue for Mg as the first three rings were easily isolated. Despite these restrictions for MgO, it was still possible to generate a DF image mostly consisting of MgO by maximizing the area of the MgO rings and minimizing the area of Mg inside the objective aperture. This resulted in a DF image of only Mg grains as shown in Figure 5.5(c) and a DF image of predominantly MgO grains as shown in Figure 5.5(d).

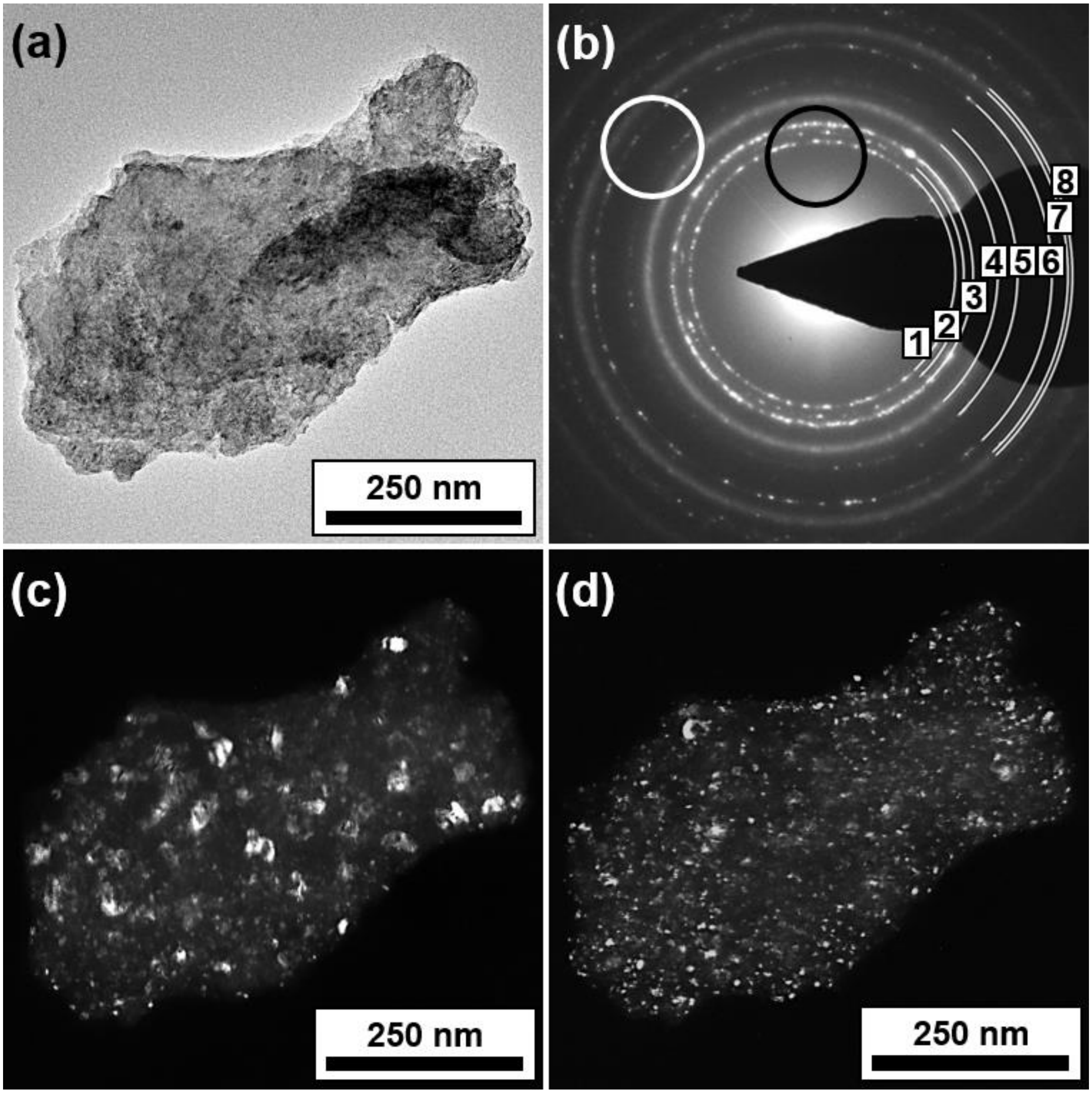

Figure 5.5: Transmission electron microscopy (TEM) analysis of a single cryomilled powder. (a) Bright-field image with (b) the resulting selected area diffraction (SAED) pattern generated by the entire powder particle, along with complementary dark-field images taken with the objective aperture encompassing the area of the SAED pattern indicated by (c) the black circle showing Mg grains and (d) the white circle showing mostly MgO grains.

Ring	d (nm)	Ref. (nm)	Error (%)	Lattice	Plane	Phase
1	0.2782	0.2779	0.05	HCP	$10\bar{1}0$	Mg
2	0.2609	0.2605	0.01	HCP	0002	Mg
3	0.2438	0.2452	0.58	HCP	$10\bar{1}1$	Mg
4	0.2098	0.2102	0.19	FCC	200	MgO
5	0.1899	0.1901	0.05	HCP	$10\bar{1}2$	Mg
6	0.1608	0.1604	0.20	HCP	$11\bar{2}0$	Mg
7	0.1482	0.1486	0.27	FCC	220	MgO
8	0.1462	0.1473	0.75	HCP	$10\bar{1}3$	Mg

Figure 5.5 (*cont. from previous page*): Table showing the interplanar spacings as calculated from each of the SAED rings along with the indexed planes and identified phases.

Looking at the two DF images in Figure 5.5, it is clear that the Mg and MgO grains have different grain size distributions with Mg grains appearing noticeably larger. In order to characterize the two grain size structures, several powder particles were imaged with Mg and MgO DF images similar to the ones shown in Figure 5.5. From these DF images, several hundred individual grains of Mg and MgO were measured. Histograms of both the Mg and MgO grain size measurements are provided in Figure 5.6 with the number and area averages provided for the Mg grains in Figure 5.6(a) and the MgO grains in Figure 5.6(b). For Mg, the area and volume average grain diameter are 11 ± 7 nm and 20 ± 9 nm, respectively. For MgO, the area and volume average grain diameter are 5 ± 2 nm and 6 ± 2 nm, respectively. These values are in good agreement with the crystallize size measurements from XRD which showed an average crystallite size for Mg of 18 ± 2 nm and an average crystallite size of MgO of 2 ± 1 nm. The slight discrepancy between the MgO crystallite and grain sizes is most likely due to the inability to accurately measure grains below a few nanometers in diameter. Signal from such small grains is often diffuse and does not produce enough contrast to distinguish from the background.

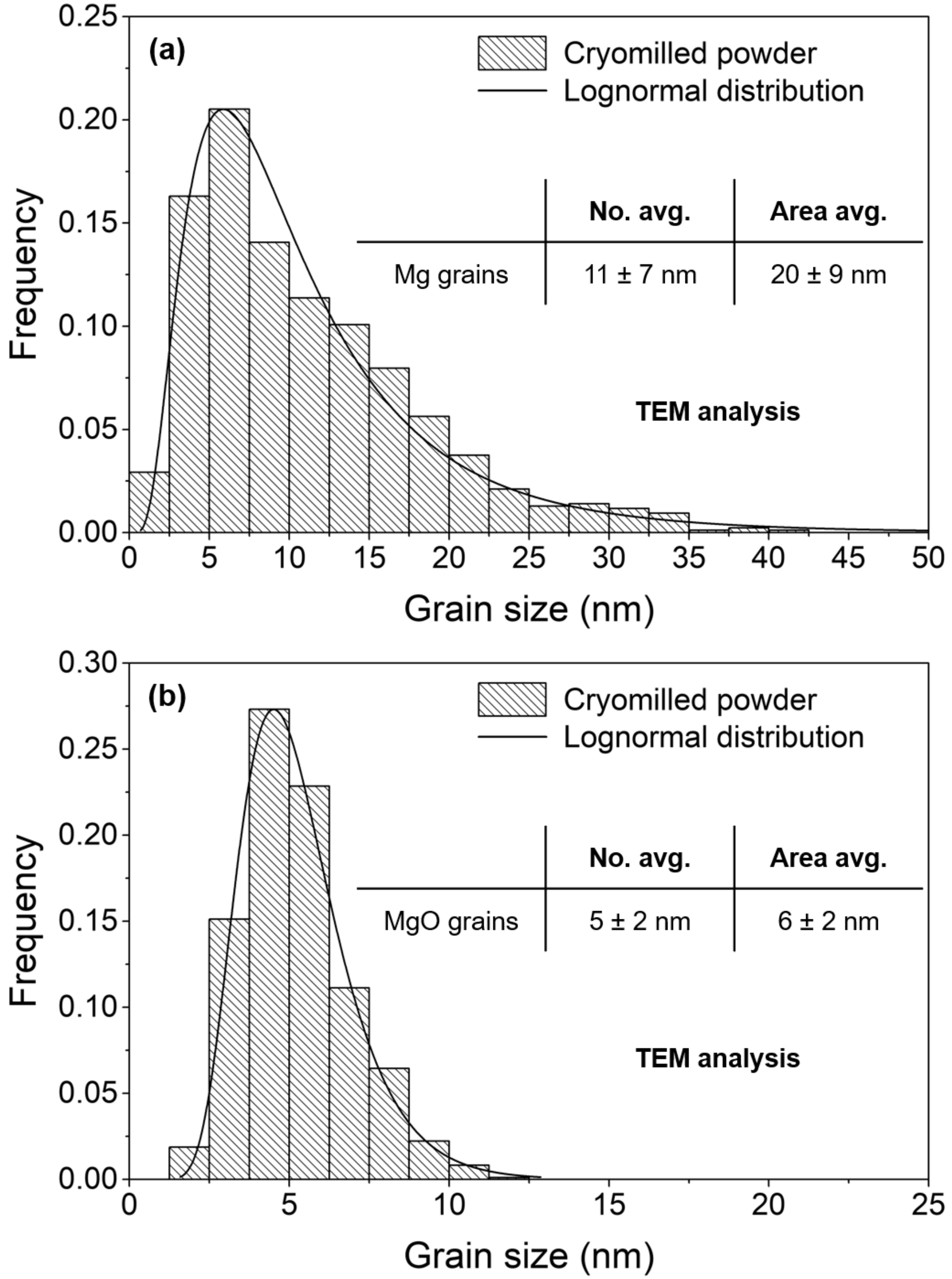

	No. avg.	Area avg.
Mg grains	11 ± 7 nm	20 ± 9 nm

	No. avg.	Area avg.
MgO grains	5 ± 2 nm	6 ± 2 nm

Figure 5.6: Grain size histograms of the cryomilled powder as measured by TEM for both the (a) Mg phases and (b) MgO phases in the cryomilled powder.

To further characterize the grain and phase distribution of the cryomilled powder, FIB was used to create a thin slice of a selected cryomilled powder particle for analysis with S/TEM, similar to the process used on the as-received powder. These results are presented in Figure 5.7. The individual powder particle as imaged by STEM HAADF is shown in Figure 5.7(a) which shows a unique and non-homogenous microstructure. The uneven contrast of the STEM HAADF image suggests an uneven distribution of phases and/or elements. The SAED pattern as generated from the area enclosed by the white box of the powder particle is presented in Figure 5.7(b) which shows that the only two phases are Mg and MgO which confirms the results obtained from XRD. A separate STEM HAADF image of this area enclosed by the white box is also shown in Figure 5.7(c) which highlights what appears to be a slight lamellar-type structure. Figure 5.7(d) shows the TEM DF image of this region with the objective aperture placed on the region of the SAED pattern as shown by the white circle indicating that both Mg and MgO phases are selected.

Another cryomilled powder particle was prepared and thinned via the FIB process for additional characterization by S/TEM. This second cryomilled powder particle study is presented in Figure 5.8. A similar STEM HAADF image of the overall powder particle is shown in Figure 5.8(a) which again shows a non-homogenous distribution of elements and/or phases as evident by the non-uniform contrast. Figure 5.8(b) shows the SAED pattern from the area enclosed by the white box which again confirms the presence of only Mg and MgO. Figure 5.8(c) displays a higher magnification STEM HAADF image of the area indicated by the white box which shows additional contrast than the first powder particle in Figure 5-7 did. This image shows additional contrast with the addition of a brighter, almost white, contrast shown towards the bottom half of the image. The TEM DF image of this same region is shown in Figure 5.8(d) with the objective aperture placed on the region of the SAED pattern as shown by the white circle indicating that both Mg and MgO phases are selected which shows a similar distribution as shown in Figure 5.7. Further analysis of this region will be discussed in the following paragraphs.

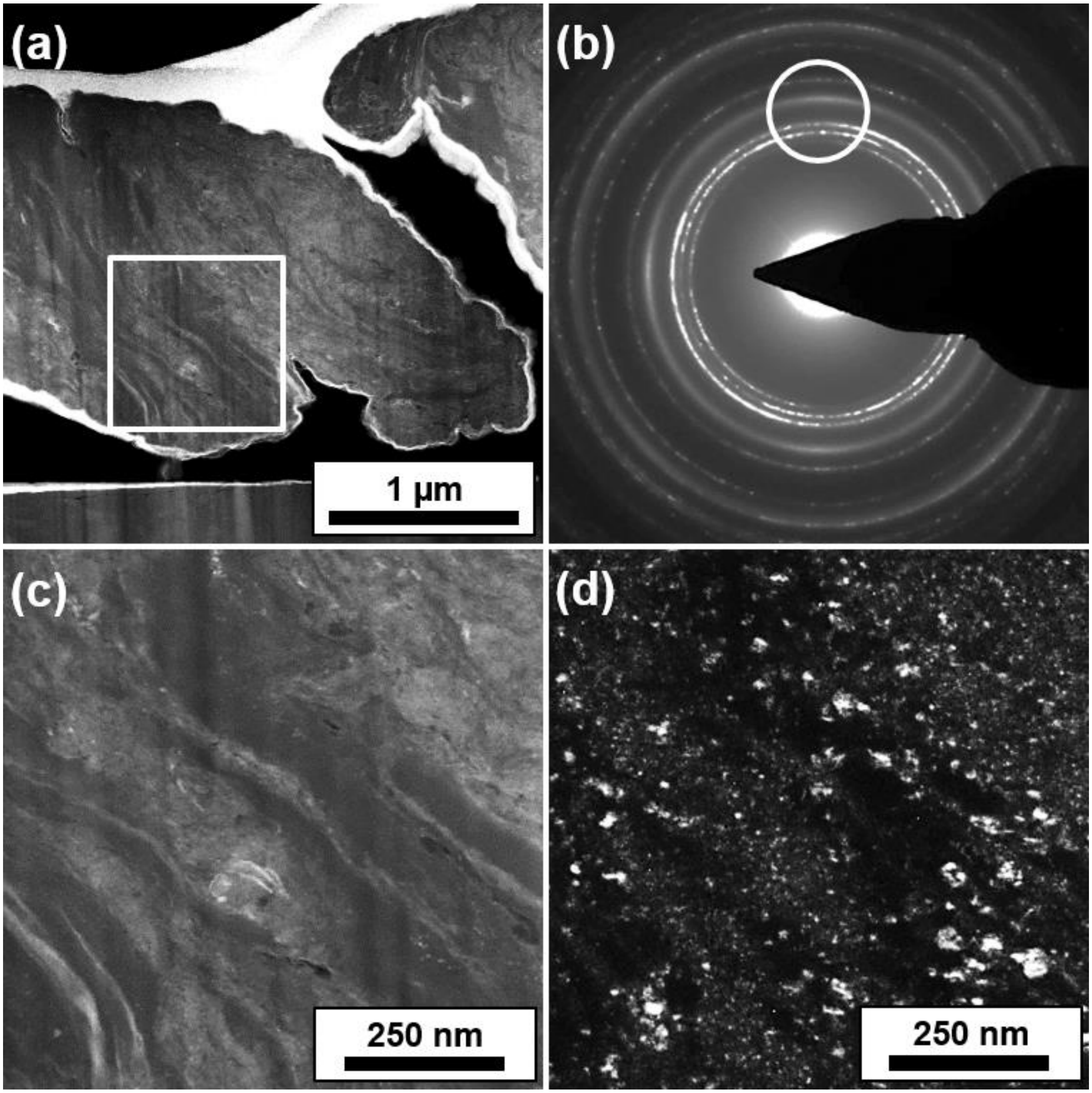

Figure 5.7: S/TEM analysis of a single cryomilled powder prepared by FIB. (a) Low magnification STEM HAADF image of cryomilled powder with (b) resulting SAED pattern generated from the area indicated by the white box, along with a complementary (c) STEM HAADF and (d) dark-field image taken of the area enclosed by the white box with the objective aperture encompassing the area of the SAED pattern indicated by white circle showing both Mg and MgO grains.

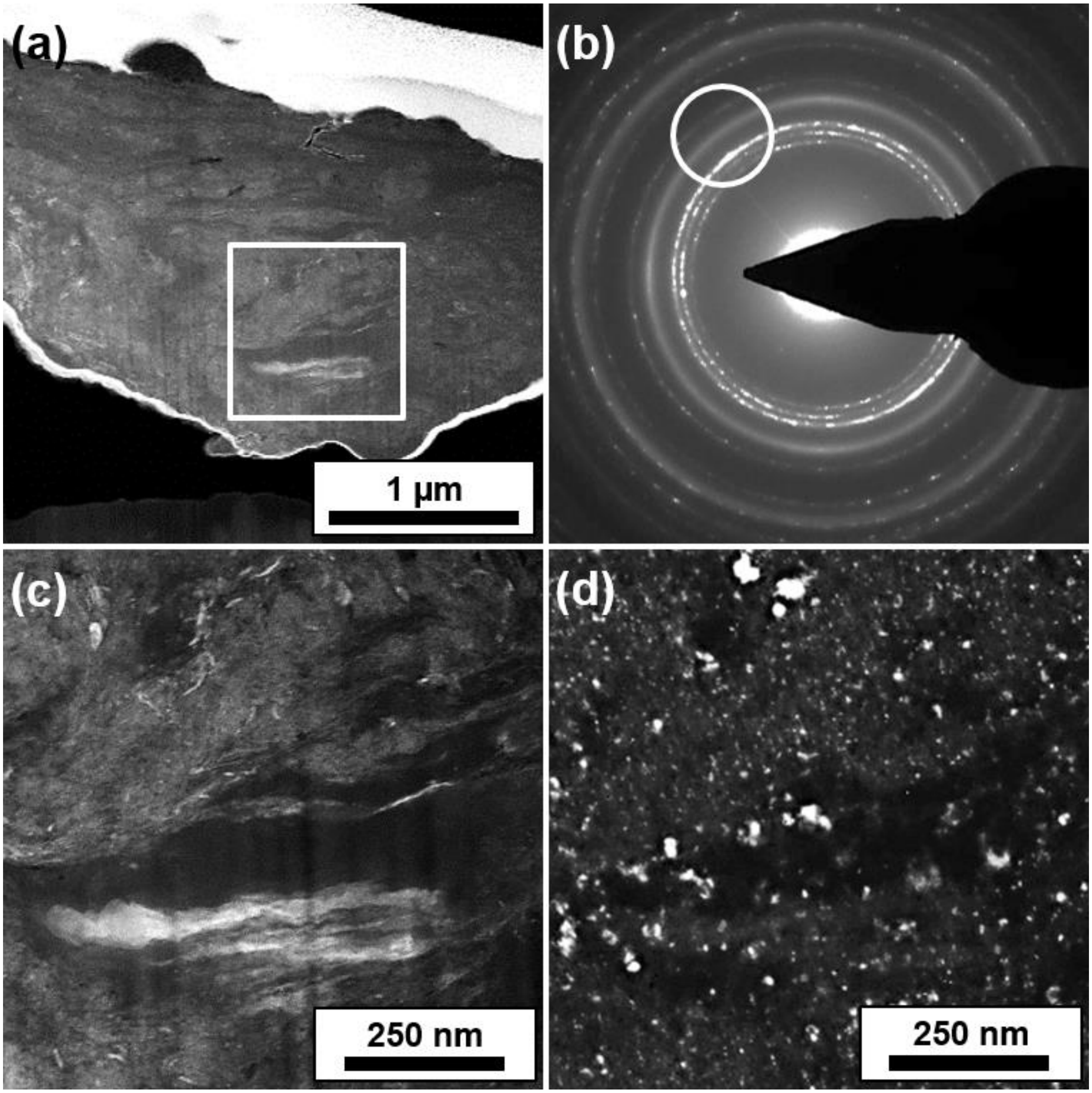

Figure 5.8: S/TEM analysis of a single cryomilled powder prepared by FIB. (a) Low magnification STEM HAADF image of cryomilled powder with (b) resulting SAED pattern generated from the area indicated by the white box, along with a complementary (c) STEM HAADF and (d) dark-field image taken of the area enclosed by the white box with the objective aperture encompassing the area of the SAED pattern indicated by white circle showing both Mg and MgO grains.

From both of the analysis represented in both Figure 5.7 and Figure 5.8, it is clear that there is a non-uniform distribution of elements as shown by the differing contrast in the STEM HAADF images. As mentioned previously, the contrast from STEM HAADF images comes mainly from Z-contrast, indicating that the brighter regions in these images contain heavier elements such as RE elements. From these figures it is also apparent that these different contrast regions. It also appears that that these different regions, as identified by contrast, have a difference in phase and grain distributions. If we look at the darker regions in the STEM HAADF images and compare them to the TEM DF images, we can see that the coarser Mg grains are somewhat concentrated in these regions with the nanocrystalline Mg and MgO grains predominantly in the lighter contrast images. From both of these observations about contrast and phase distribution, it is likely that the powders were not milled sufficiently which resulted in insufficient mass transfer.

In order to correlate the contrast seen in the STEM HAADF images and in order to determine the elemental distribution, STEM-EDS mapping was performed on a zoomed-in portion of Figure 5.8(c). These elemental maps are provided in Figure 5.9 with the mapped elements of Mg, Y, O, Nd, and Zr along with a BF and DF TEM images showing the same area and showing the distribution of both the Mg and MgO grains. From this figure, we can see that there is a clear segregation of elements in the different contrasted regions in the STEM HAADF image. It is evident that these dark contrasted regions are essentially pure Mg with the bulk of the oxygen (and thus MgO) located in these grey contrasted regions along with the addition of some RE elements. The brightest contrasted region seen in the STEM HAADF image seems to be a large pocket of Y and Nd which is why there appears to be so much contrast from this region. However, from the overall STEM images of the powder particles in Figure 5.7 and Figure 5.8, this region is not quite representative. Despite this, it is clear that the overwhelming majority of the microstructure is composed of these grey contrasted regions which contain Y, RE elements, and the MgO grains while the dark contrasted regions are essentially pure Mg.

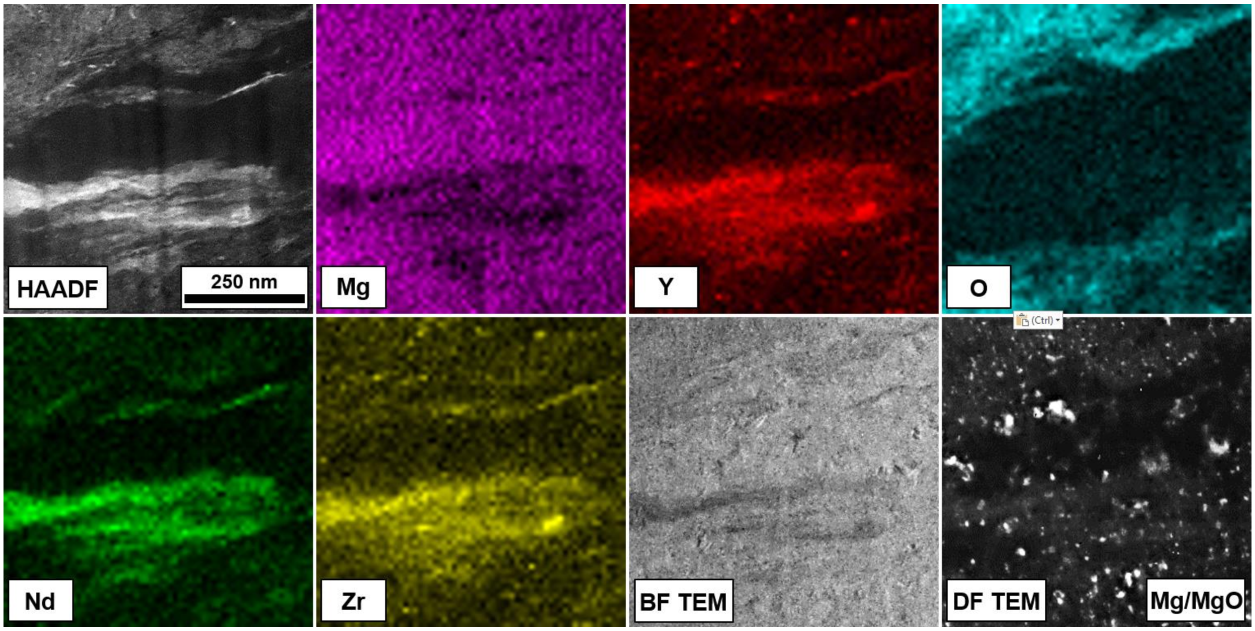

Figure 5.9: STEM-EDS elemental mapping of the cryomilled sample showing the STEM HAADF image of the overall sampling area with the individual mapped elements for Mg, Y, O, Nd, and Zr along with complementary TEM bright-field and dark-field images (dark-field image taken from Figure 5.8 and with both images appropriately cropped and scaled) showing the distribution of Mg and MgO grains. All images are of the same region and set to the same scale.

Chapter 6

Characterization of Magnesium-Based Bulk Nanocomposite

6.1 Phase Identification and Crystallite Size

6.1.1 Conventional X-Ray Diffraction

Figure 6.1 shows the conventional XRD spectra for both the cryomilled powder and the as-SPS'ed sample (the sample made by consolidating the cryomilled powder), showing the effect of the SPS process. From both spectra, it is clear that no additional phases are produced from the consolidation process, and the only phases present in any meaningful quantities are Mg and MgO. It is also clear from the spectra that the SPS process has led to the coarsening of the Mg grains as illustrated by the sharpening (decrease in width) of the peaks along with an increase in relative peak intensity. There does not seem to be a similar sharpening with the MgO peaks, indicating little or no grain growth. To quantify this effect, the crystallite size of both the Mg and MgO phases is presented in Table 6.1 along with the Mg lattice parameters for both the cryomilled powder and the as-SPS'ed sample. The crystallite size for the Mg phase goes from 18 ± 1 nm for the cryomilled powder to 79 ± 4 nm for the as-SPS'ed, indicating grain growth. The crystallite size for the MgO phases stays constant at 2 ± 1 nm for both the cryomilled powder and the as-SPS'ed sample, indicating no grain growth. It should be noted, as mentioned in Chapter 4. that if the grain size distribution of the Mg grains after the SPS process is not unimodal, the crystallite size might not be an accurate representation of the actual Mg grain size. However, the Mg crystallite size does qualitatively indicate that grain growth has occurred and that significant changes have occurred to the overall grain structure of the material.

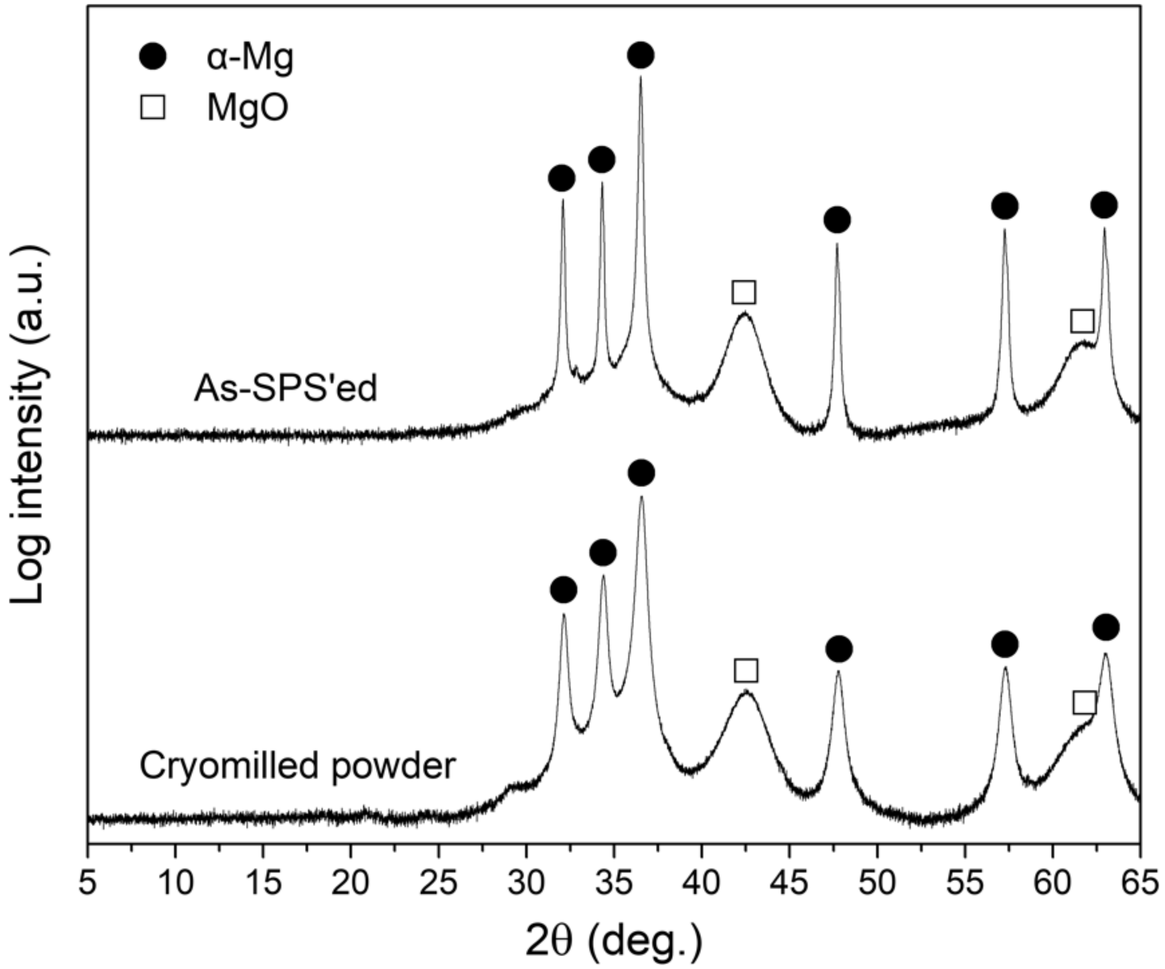

Figure 6.1: Conventional XRD spectra for both the cryomilled powder and the as-SPS'ed sample.

Table 6.1: Relevant lattice constants and crystallite sizes as calculated from the conventional XRD spectra for the cryomilled powder and the as-SPS'ed sample given in Figure 6.1.

	Mg Lattice Parameters			**Crystallite size (nm)**	
	a (nm)	c (nm)	c/a	Mg	MgO
Cryomilled pwd.	0.3213 ± 0.0004	0.5212 ± 0.0003	1.622 ± 0.003	18 ± 2	2 ± 1
As-SPS'ed	0.3215 ± 0.0004	0.5215 ± 0.0004	1.622 ± 0.003	79 ± 4	2 ± 1
Pure Mg	0.3209	0.5210	1.624	-	-

In terms of the Mg lattice parameters, there appears to be no difference between the two samples and in relation to the pure Mg reference, indicating that the SPS process did not have any significant effect on the solubility of the rare earth elements in α-Mg. If the cryomilling process had induced a solid supersaturation of RE elements in magnesium, the SPS process would have likely precipitated out these elements in the form of intermetallic compounds. The fact that there is almost no change in the lattice parameters and the fact that these lattice parameters are almost identical to that of pure Mg suggests that there is no significant solubility of the RE elements in the α-Mg. This along with the absence of any intermetallic phases suggests that the RE elements might be elementally segregated to the large area fraction of the nanocrystalline α-Mg grain boundaries, making them less likely to coalesce and form intermetallic compounds during the relatively short time in which the consolidation takes place.

Figure 6.2 shows the conventional XRD spectra for both the SPS control sample (the sample made by consolidating the as-received powder) and the as-SPS'ed sample, along with the relevant lattice parameters and crystallite sizes in Table 6.2, showing the effect that the SPS process has on the as-received powders without the cryomilling process. The differences between these two samples is stark, with the SPS control sample showing the creation of the equilibrium $Mg_{41}Nd_5$ intermetallic compound. This intermetallic compound is absent in the as-SPS'ed sample, showing a large difference between the two powder samples. In addition to the creation of this equilibrium intermetallic phase, it is also clear that the intermetallic compound present in the as-received powders (Mg_3RE) was eliminated during the SPS process without mechanical milling, supporting the conclusion that this was a non-equilibrium phase. Also, the fact that the SPS process did not lead to the formation of the $Mg_{41}Nd_5$ intermetallic phase with the cryomilled powder, as did in the SPS control sample, reaffirms the conclusion that the RE elements are elementally segregated to the grain boundaries. Another large difference between these two samples in the absence of MgO in the SPS control sample, demonstrating that the SPS process is not a source of MgO in the as-SPS'ed sample.

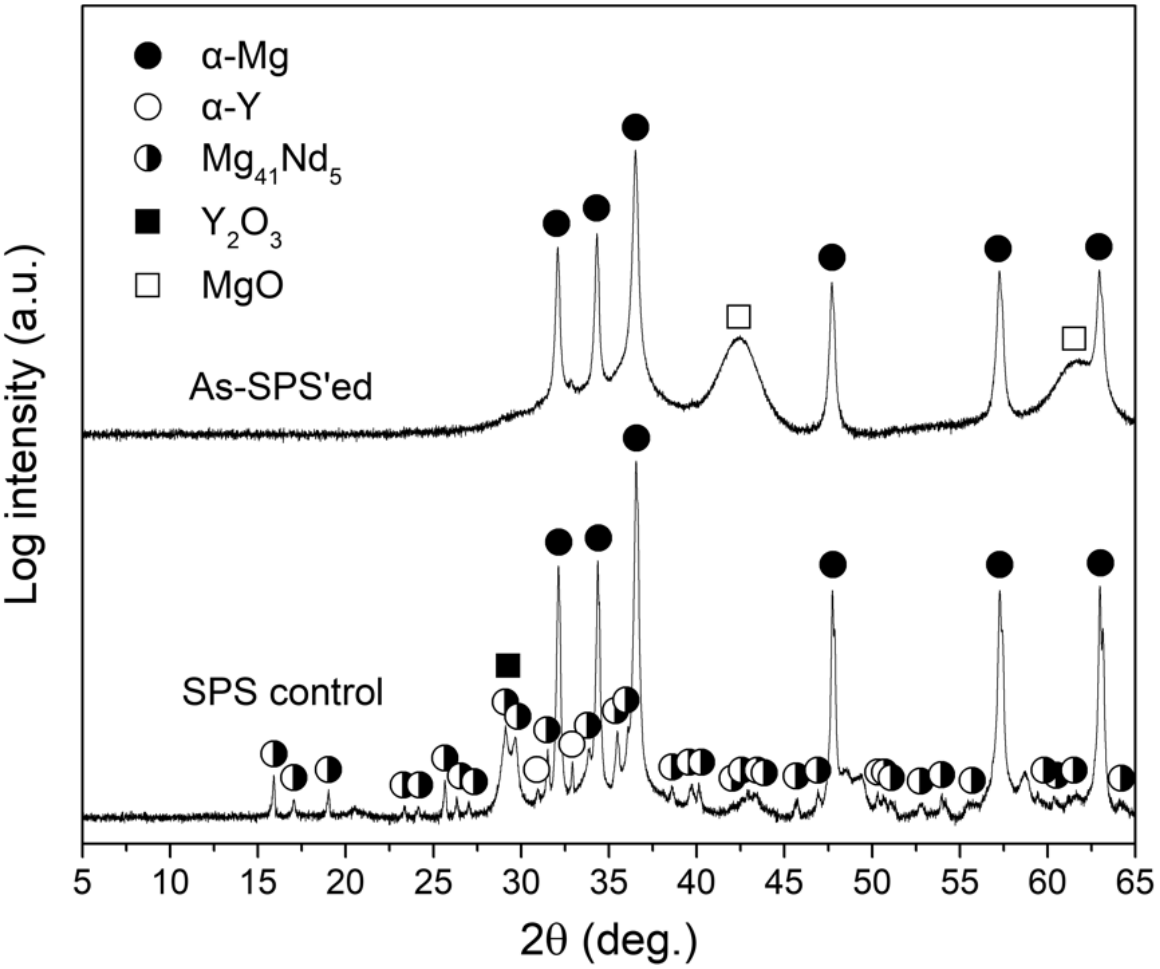

Figure 6.2: Conventional XRD spectra for both the SPS control sample and the as-SPS'ed sample.

Table 6.2: Relevant lattice constants and crystallite sizes as calculated from the conventional XRD spectra for the SPS control and the as-SPS'ed samples given in Figure 6.2.

	Mg Lattice Parameters			**Crystallite size (nm)**	
	a (nm)	c (nm)	c/a	Mg	MgO
SPS control	0.3215 ± 0.0005	0.5215 ± 0.0004	1.622 ± 0.003	113 ± 45	-
As-SPS'ed	0.3215 ± 0.0004	0.5215 ± 0.0004	1.622 ± 0.003	79 ± 4	2 ± 1
Pure Mg	0.3209	0.5210	1.624	-	-

6.1.2 Synchrotron X-Ray Diffraction

Figure 6.3 shows the synchrotron XRD spectra for both the cryomilled powder and the as-SPS'ed sample, again showing the effect of the SPS process had on the cryomilled powders. Almost identical data is presented in the synchrotron XRD spectra, compared to the spectra given from conventional XRD. The synchrotron XRD spectra confirms that the only phases present in any meaningful concentration in both the powders and the as-SPS'ed sample are Mg and MgO. Table 6.3 displays the Mg lattice parameters as well as the crystallite sizes for both the Mg and MgO phases, showing that the Mg crystallites grew from 17 nm in the cryomilled powder to 37 nm in the as-SPS'ed sample with the MgO crystallites just slightly increasing from 3 nm to 4 nm in the as-SPS'ed sample. Again, it is not clear if the Mg crystallite size for the as-SPS'ed sample is meaningful. There does seem to be a slight difference in the Mg lattice parameters between the cryomilled powder and the as-SPS'ed sample, with the Mg lattice parameters of the cryomilled sample being smaller which could be due from strain induced during the cryomilling process. However, if this difference is indeed due to stresses induced from cryomilling, the SPS process seems to relieve these stresses as the Mg lattice parameters increase to the values of pure Mg in the as-SPS'ed sample. Also, due to only one sample being run for the synchrotron data, it is difficult to tell whether this is within the error of the measurements.

It is important to note that one of the two unknown phases identified in the cryomilled powders was eliminated during the SPS consolidation process. Although this phase was unknown and was only present in the cryomilled powders, it is not present in the as-SPS'ed sample making it less critically important. The other unknown phase that was shown in the synchrotron XRD of the as-received powders is still present in the as-SPS'ed sample, with a single faint peak around 5°. However, it is in such a small quantity in relation to the Mg and MgO phases, and its impact on the microstructure and mechanical properties will most likely be negligible.

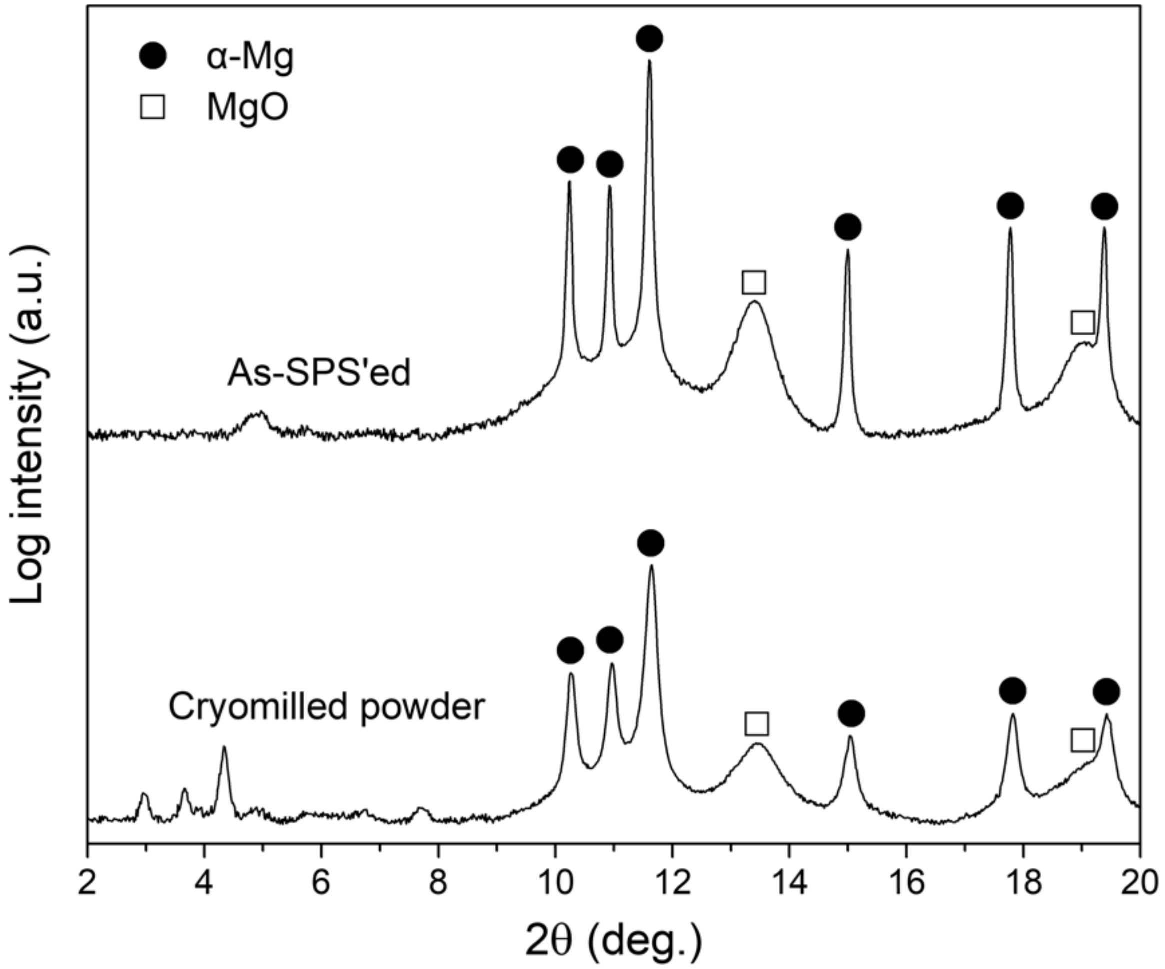

Figure 6.3: Synchrotron XRD spectra for both the cryomilled powder and the as-SPS'ed sample.

Table 6.3: Relevant lattice constants and crystallite sizes as calculated from the synchrotron XRD spectra for the cryomilled powder and the as-SPS'ed sample given in Figure 6.3.

	Mg Lattice Parameters			**Crystallite size (nm)**	
	a (nm)	c (nm)	c/a	Mg	MgO
Cryomilled pwd.	0.3202	0.5189	1.621	17	3
As-SPS'ed	0.3210	0.5209	1.623	37	4
Pure Mg	0.3209	0.5210	1.624	-	-

6.2 Microstructure

6.2.1 Scanning Electron Microscopy

Figure 6.4 presents the side-by-side SEM images showing the microstructures of both the SPS control sample and the as-SPS'ed sample. There are quite a few differences between the microstructures of these two samples with the main difference being that for the SPS control sample in Figure 6.4(a), the prior particle boundaries (PPBs) are still present. It appears that the passivation layer on the as-received powders was not broken up during the SPS process which inhibited diffusion between adjacent powder particles leading to incomplete bonding. This incomplete bonding is most evident at triple-point junctions where diffusion across the passivation layer was not enough to sufficiently fill the geometrical voids during the sintering process. Additional proof that these apparent PPBs are indeed the remaining particle oxide layers is that the size distribution of these PPBs is roughly equal, by simple visual inspection, to the particle size distribution data obtained from the as-received powder via the SediGraph analysis, with a volume average powder particle diameter of 19.6 ± 11.6 μm.

In the case for the as-SPS'ed sample in Figure 6.4(b), there does not seem to be any issues with PPBs as this oxidation layer was broken up during the cryomilling process and therefore is absent in the SEM image. The as-SPS'ed sample does, however, display what looks like a duplex microstructure consisting of two distinct regions: one region with darker contrast occupying a relatively small volume fraction of the overall material, and another region with brighter contrast occupying the remaining vast majority of the volume fraction. It should also be noted that no etchant was used in preparing the samples for SEM by polishing, indicating that these darker regions in the as-SPS'ed sample are softer in comparison to the lighter regions, showing topographical relief due to a faster removal rate in these darker regions during the final polishing steps. Additional techniques will be needed to further characterize these two regions of the as-SPS'ed microstructure.

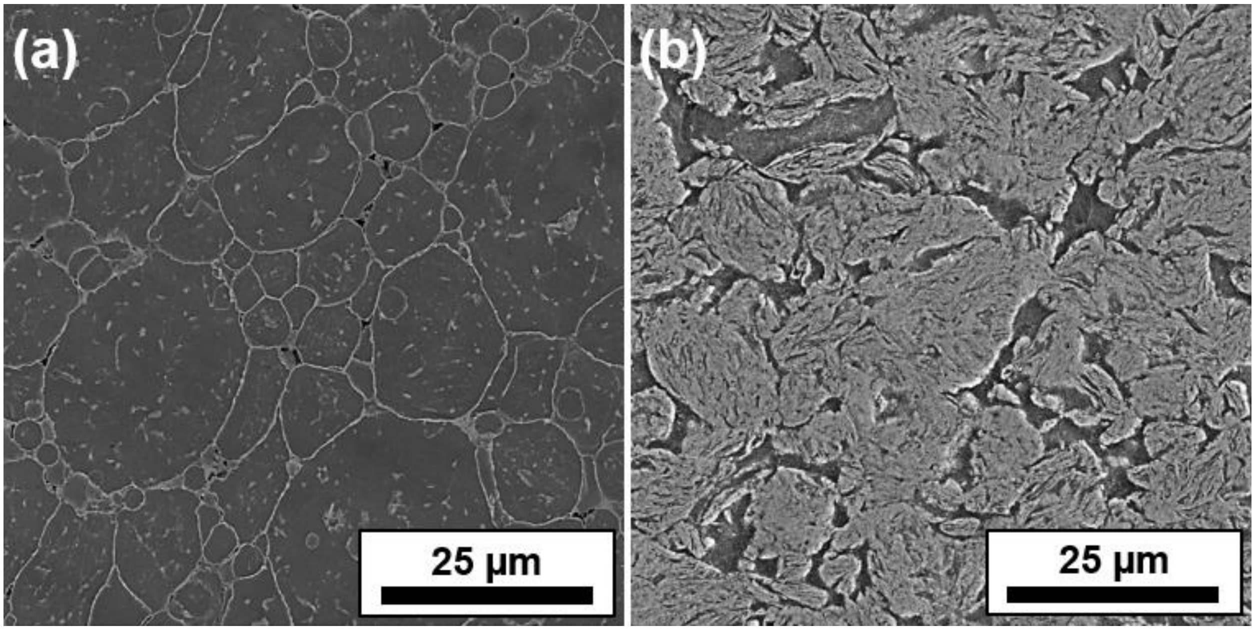

Figure 6.4: SEM microstructural images of (a) the SPS control sample and (b) the as-SPS'ed sample.

In order to determine the chemical composition and elemental distribution of both bulk samples, EDS elemental mapping was performed with the SEM on the SPS control sample as well as on the as-SPS'ed sample with the results presented in Figure 6.5 and Figure 6.6, respectively. Each of these figures display an SEM image of a selected representative area along with EDS elemental mapping for Mg, Y, O, Nd, and Zr along with EDS point analysis for two selected points of each sample as indicated on the SEM images. Additional chemical analysis of the SPS control sample and the as-SPS'ed sample is provided in Table 6.4 and Table 6.5, respectively, which gives the overall chemical analysis as measured by the EDS elemental maps given in their respective figures. As noted previously in Chapter 5, the EDS analysis for Zr should be viewed with skepticism as there does not seem to be any difference in the elemental maps from these two elements, suggesting that the Zr elemental map is simply produced based on the larger EDS signal from Y. The same skepticism should be applied to the EDS point analysis for Zr in both the SPS control sample as well as the as-SPS'ed sample.

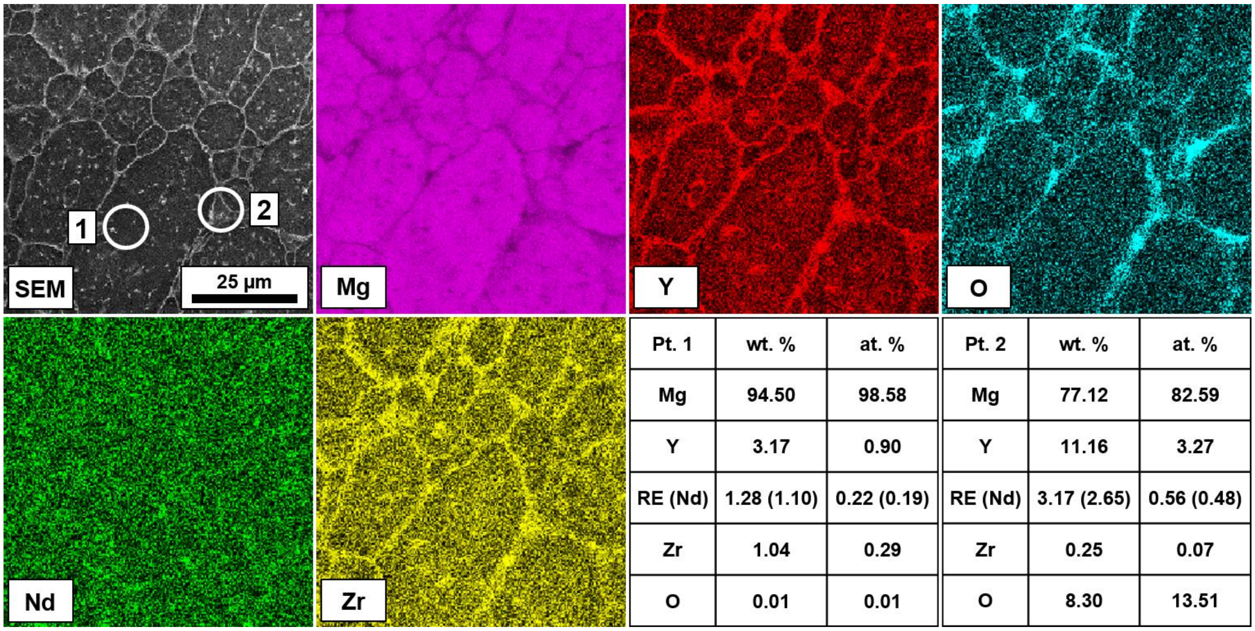

Pt. 1	wt. %	at. %
Mg	94.50	98.58
Y	3.17	0.90
RE (Nd)	1.28 (1.10)	0.22 (0.19)
Zr	1.04	0.29
O	0.01	0.01

Pt. 2	wt. %	at. %
Mg	77.12	82.59
Y	11.16	3.27
RE (Nd)	3.17 (2.65)	0.56 (0.48)
Zr	0.25	0.07
O	8.30	13.51

Figure 6.5: SEM-EDS elemental mapping of the SPS control sample showing the SEM image of the overall sampling area with the individual mapped elements for Mg, Y, O, Nd, and Zr along with EDS point analysis for point 1 and point 2 as indicated in the SEM image where RE = Nd + Gd + Dy. All images are of the same region and set to the same scale. Standard deviation values similar to those presented in Table 6.4.

Table 6.4: Overall chemical analysis of the SPS control sample as measured by the EDS elemental mapping given in Figure 6.5.

	Mg	Y	Total RE	(Individual RE)	Zr	O
wt. %	91.60 ± 0.34	4.36 ± 0.02	2.63 ± 0.08	Nd: 2.25 ± 0.03 Gd: 0.31 ± 0.03 Dy: 0.07 ± 0.02	1.04 ± 0.02	0.37 ± 0.01
at. %	97.39 ± 0.36	1.27 ± 0.01	0.46 ± 0.03	Nd: 0.40 ± 0.01 Gd: 0.05 ± 0.01 Dy: 0.01 ± 0.01	0.29 ± 0.01	0.59 ± 0.02

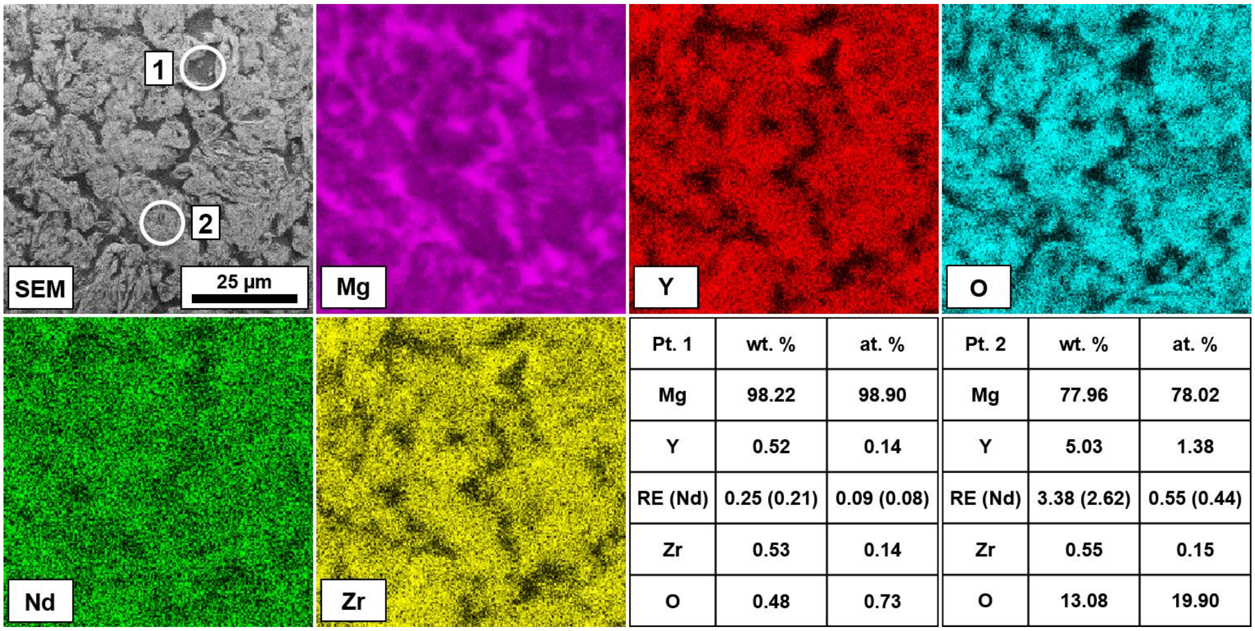

Pt. 1	wt. %	at. %
Mg	98.22	98.90
Y	0.52	0.14
RE (Nd)	0.25 (0.21)	0.09 (0.08)
Zr	0.53	0.14
O	0.48	0.73

Pt. 2	wt. %	at. %
Mg	77.96	78.02
Y	5.03	1.38
RE (Nd)	3.38 (2.62)	0.55 (0.44)
Zr	0.55	0.15
O	13.08	19.90

Figure 6.6: SEM-EDS elemental mapping of the as-SPS'ed sample showing the SEM image of the overall sampling area with the individual mapped elements for Mg, Y, O, Nd, and Zr along with EDS point analysis for point 1 and point 2 as indicated in the SEM image where RE = Nd + Gd + Dy. All images are of the same region and set to the same scale. Standard deviation values similar to those presented in Table 6.5.

Table 6.5: Overall chemical analysis of the as-SPS'ed sample as measured by the EDS elemental mapping given in Figure 6.6.

	Mg	**Y**	**Total RE**	**(Individual RE)**	**Zr**	**O**
wt. %	82.14 ± 0.30	3.61 ± 0.02	2.72 ± 0.07	Nd: 2.17 ± 0.03 Gd: 0.24 ± 0.02 Dy: 0.31 ± 0.02	1.42 ± 0.02	10.11 ± 0.03
at. %	82.70 ± 0.30	0.99 ± 0.01	0.46 ± 0.03	Nd: 0.37 ± 0.01 Gd: 0.04 ± 0.01 Dy: 0.05 ± 0.01	0.38 ± 0.01	15.47 ± 0.05

Looking at the EDS elemental mapping for the SPS control sample in Figure 6.5, it is clear that the areas previously identified as the PPBs (the areas in the SEM image with lighter contrast) are indeed the outlines of individual particles fused during the SPS consolidation process as indicated by the elemental maps of Mg, Y, and O. The Mg elemental map shows that the PPBs are slightly depleted in Mg as indicated by the slightly darker color along these regions. The EDS point analysis also quantifies this Mg difference showing that the interior of one of these particles is roughly 95 wt. % Mg (point 1) while a point sampled from one of triple-point junctions measured 77 wt.% Mg (point 2). The Y and O elemental maps shows an even greater contrast, showing a substantial difference in the amount of Y and showing that the oxygen content is segregated to these boundaries. There does not seem to be any noticeable contrast in the Nd elemental map, suggesting that the distribution of Nd is uniform which is also supported by the EDS point analysis. It is also quite possible that the signal generated from Nd has a low signal-to-background ratio, making it difficult to distinguish between the background and thus making it difficult to accurately ascertain the distribution of Nd. Although Nd is the only RE element that is mapped, other RE elements were measured, including Gd and Dy. However, since the majority of the RE elements are from Nd, the elemental maps for Gd and Dy were not useful as they were indistinguishable from the background signal. And lastly, for the overall chemical composition of the SPS control sample from Table 6.4, we see that the total oxygen content is only 0.37 wt. % which is similar to the EDS results of the as-received powder which was measured to be 1.03 wt. %.

For the elemental mapping of the as-SPS'ed sample in Figure 6.6, we can see that these two previously identified regions in the SEM image (i.e. the dark and light regions) are completely different in composition. The dark regions appear to simply be α-Mg with the other elemental maps showing almost no signal from these regions, indicating that these elements are absent. This observation is backed up by the EDS point analysis which shows that these dark regions are about 98 wt. % Mg (point 1). Contrasting this with the EDS point analysis from these light regions, we see that these lighter regions only constitute about 78 wt. % Mg (point 2) with a very high concentration of oxygen (13 wt. %) and a high concentration of Y and RE elements which are just slightly higher than their total representative percentages in the overall alloy (i.e. about 4 wt. % for Y and about 3 wt. % for RE elements). Also, since oxygen was only detected in these light regions, this analysis also shows that these regions are where the nanocrystalline MgO grains are located. From this analysis, it is clear that these two separate regions of the microstructure are chemically as well as microstructurally distinct with essentially pure Mg regions with the additional of regions rich in RE elements on MgO. For the overall chemical composition of the as-SPS'ed sample from Table 6.5, we see that the total oxygen content is 15.47 wt. % which is very similar to the results from the cryomilled powder which has an oxygen content of 12.86 wt. %. Later on in this section, we will use the atomic percent values of oxygen as measured in the as-SPS'ed sample to estimate the volume fraction of MgO.

6.2.2 Transmission Electron Microscopy

In order to investigate the as-SPS'ed sample in more detail and in order to gain greater insight into these two distinct microstructural regions, TEM along with STEM and STEM-EDS were used. The first image of the overall microstructure of the as-SPS'ed sample as taken from STEM HAADF is given in Figure 6.7. In this image, the two different microstructural regions are quite clear with the same contrast given in the SEM. From this image, we can see that even these regions rich in both MgO and RE elements have somewhat of a non-homogenous grain structure with the darker Mg regions appearing to be interwoven into the microstructure. This microstructure is similar to the microstructure as seen from the cryomilled powders seen under STEM HAADF in Chapter 5, indicating that this microstructure might be a vestige of the cryomilling process. Further characterization will need to be conducted in order to more precisely investigate these regions and in order to figure out the distribution of the nanocrystalline MgO grains.

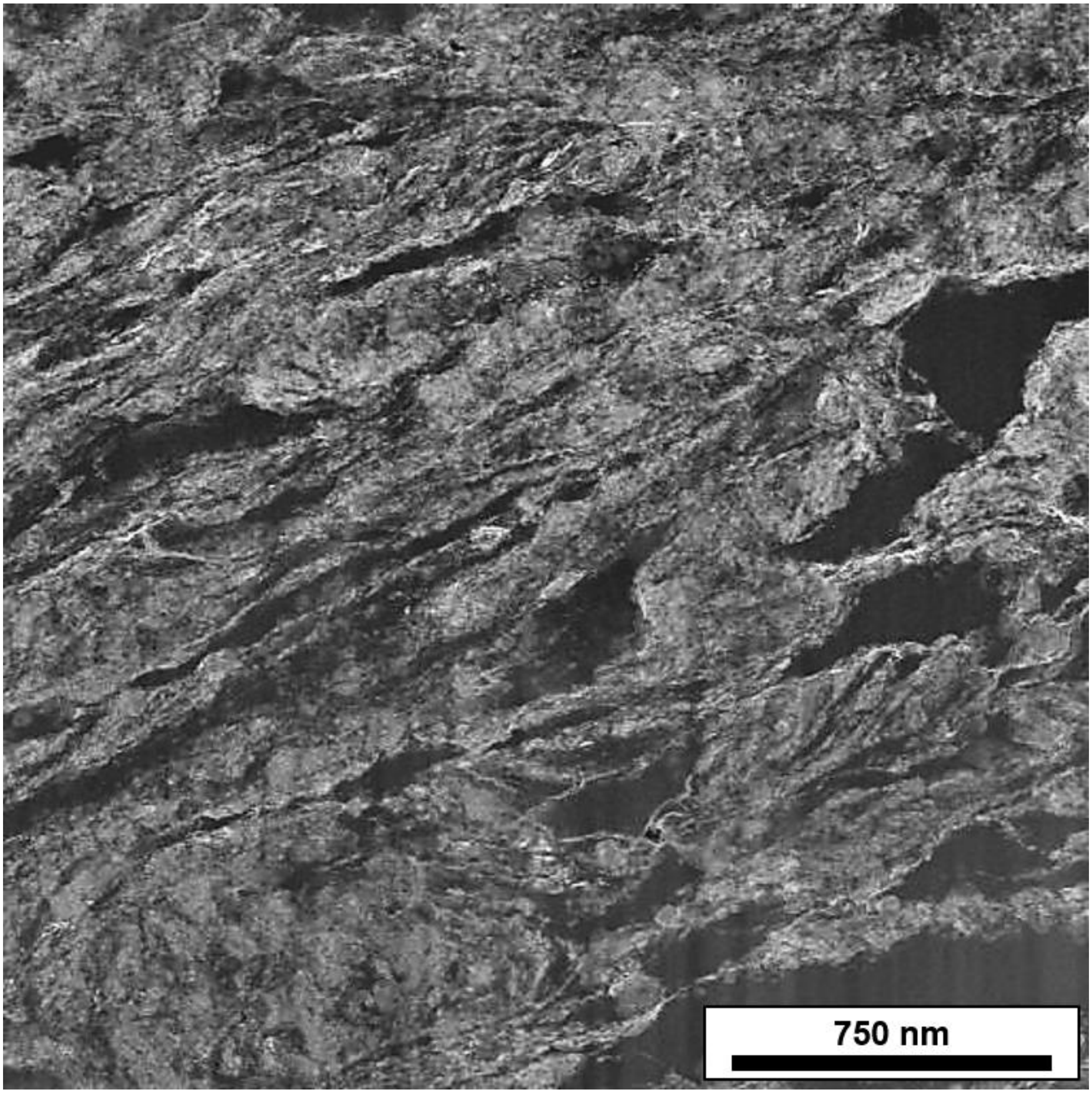

Figure 6.7: STEM HAADF microstructural image of the as-SPS'ed sample.

Further analysis of the region displayed in Figure 6.7 was performed, with a closer look at one of the features displayed in this figure which had a distinctive "fish hook" shape which was darker in contrast compared to the rest of the STEM HAADF image. This feature can be seen towards the top-center of Figure 6.7 measuring about 750 nm across. A closer look at this "fish hook" feature can be seen in Figure 6.8 which shows complete STEM and TEM analysis of this region with a STEM HAADF image presented in Figure 6.8(a). As noted in the previous chapter, STEM HAADF produces signal primarily from Z-contrast which shows regions containing higher atomic number in higher contrast. This suggest that this dark region is deficient in any RE alloying elements as these elements would produce much greater signal compared to α-Mg. Figure 6.8(b) shows the SAED pattern generated from the area of the sample which confirms that the only phases present are Mg and MgO. Figure 6.8(c) displays the DF TEM image produced using the objective aperture as indicted by the black circle in the SAED image showing Mg grains, and Figure 6.8(d) displays the DF TEM image produced using the objective aperture as indicated by the white circle in the SAED image showing mostly MgO grains. As stated in the previous chapter, it was difficult to completely isolate the MgO grains from the Mg grains.

From these two DF images in Figure 6.8, it is clear that the high contrast regions are populated with very fine MgO grains while the low contrast regions are absent of MgO and mostly contain coarser Mg grains compared to the regions containing MgO. This confirms the SEM-EDS results from the as-SPS'ed sample which show almost no oxygen content in the α-Mg regions of the microstructure. This initial analysis also suggests that the RE elements are also in these higher contrast regions that contain the MgO grains. Since oxygen has a lower Z value compared to Mg and because of how the signal is received in HAADF generated images, the high contrast between these two regions must be coming from much higher Z elements such as the RE elements and Y. This would also confirm the results from SEM-EDS which shows the oxygen containing regions also contain the majority of the RE elements along with Y.

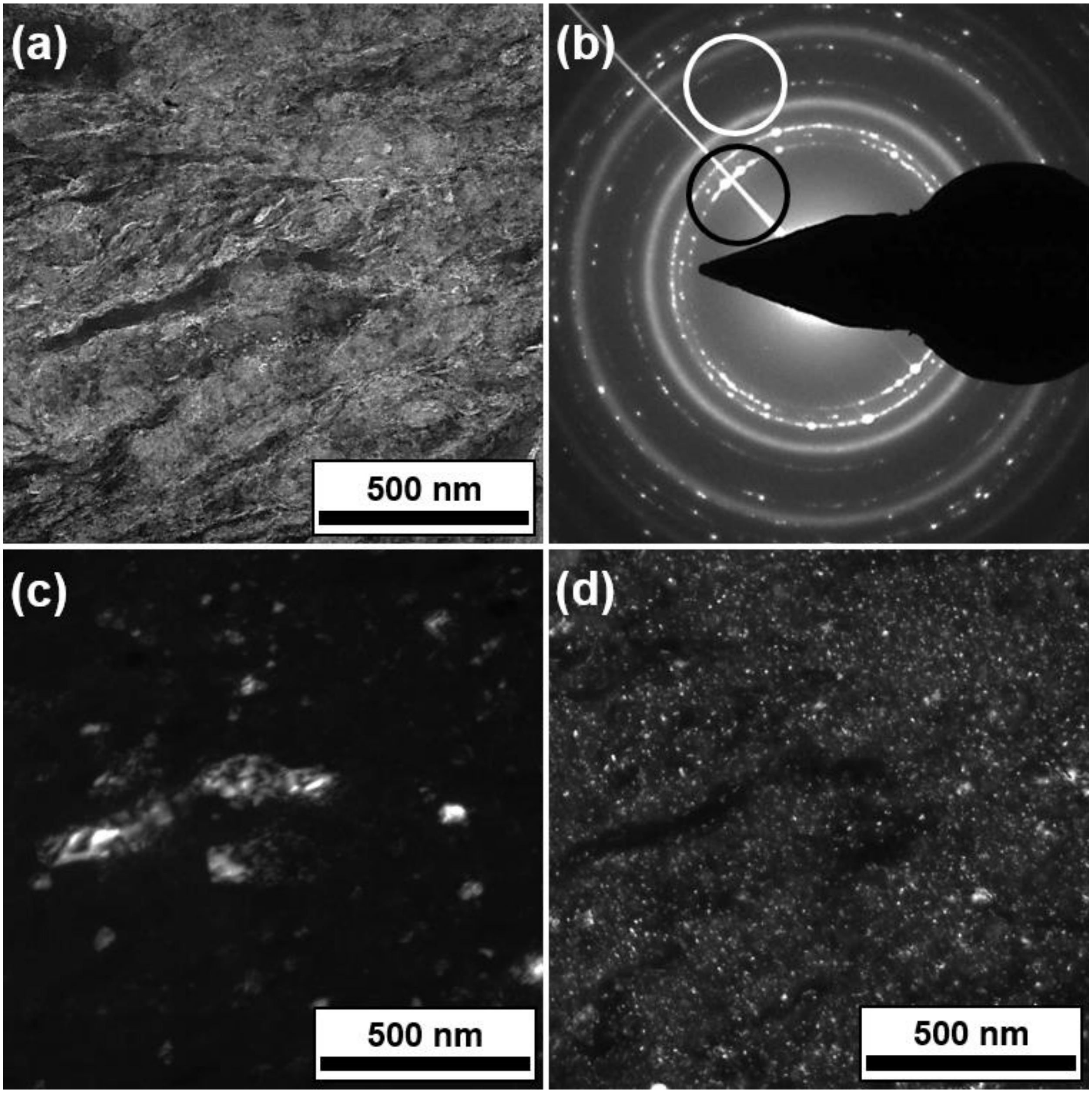

Figure 6.8: S/TEM analysis of the as-SPS'ed sample prepared FIB. (a) STEM HAADF image of as-SPS'ed sample with (b) the resulting SAED pattern generated by the entire area displayed, along with complementary dark-field images taken with the objective aperture encompassing the area of the SAED pattern indicated by (c) the black circle showing Mg grains and (d) the white circle showing mostly MgO grains.

In order to characterize the grain size distribution from both the Mg and MgO grains in these nanocrystalline regions, close to a thousand individual grains for each Mg and MgO were measured from the nanocrystalline regions with the results presented in Figure 6.9 in the form of histograms with the Mg grain data given in Figure 6.9(a) and the MgO grain data given in Figure 6.9(b). These histograms also have the grain size histograms as measured by TEM for the cryomilled powder, as previously presented in Chapter 5, overlayed to show the effects the SPS process. It should be noted that the Mg grain size histogram given in Figure 6.9(a) for the as-SPS'ed sample only includes grain data from the nanocrystalline regions (i.e. the regions containing MgO) and does not include the coarse-grained regions. This data shows that there is no difference between the overall Mg grain size in the cryomilled powders and the Mg grain size in the nanocrystalline regions of the as-SPS'ed sample, with both having a number and area average grain size of about 10 nm and 20 nm, respectively, with no grains over 50 nm being observed. In terms of the MgO grains, there seems to be a slight increase in the grain size, at least in terms of the area average grain size, with an area average grain size almost doubling in the as-SPS'ed sample from 6 nm in the cryomilled powder to 11 nm with almost no change in the number average.

To further characterize the microstructure of the as-SPS'ed sample, STEM-EDS was performed on a zoomed-in portion of the region presented in Figure 6.8, with EDS elemental maps being generated for Mg, Y, O, Nd, and Zr. This data along with similarly scaled DF images from Figure 6.8 are shown in Figure 6.10. These elemental maps confirm the results from SEM-EDS which showed the oxygen content and RE content occur in the same regions. These results along with the results from the DF TEM analysis show that these same regions are nanocrystalline in nature, with a mixture of both Mg and MgO nanocrystalline grains. It is also interesting to note that the coarser Mg grains, as seen in the "fish hook" structure, are lacking in the RE elements and nanocrystalline MgO grains, suggesting that the nanocrystalline MgO grains and RE elements are stabilizing the nanocrystalline Mg grains during the SPS consolidation process.

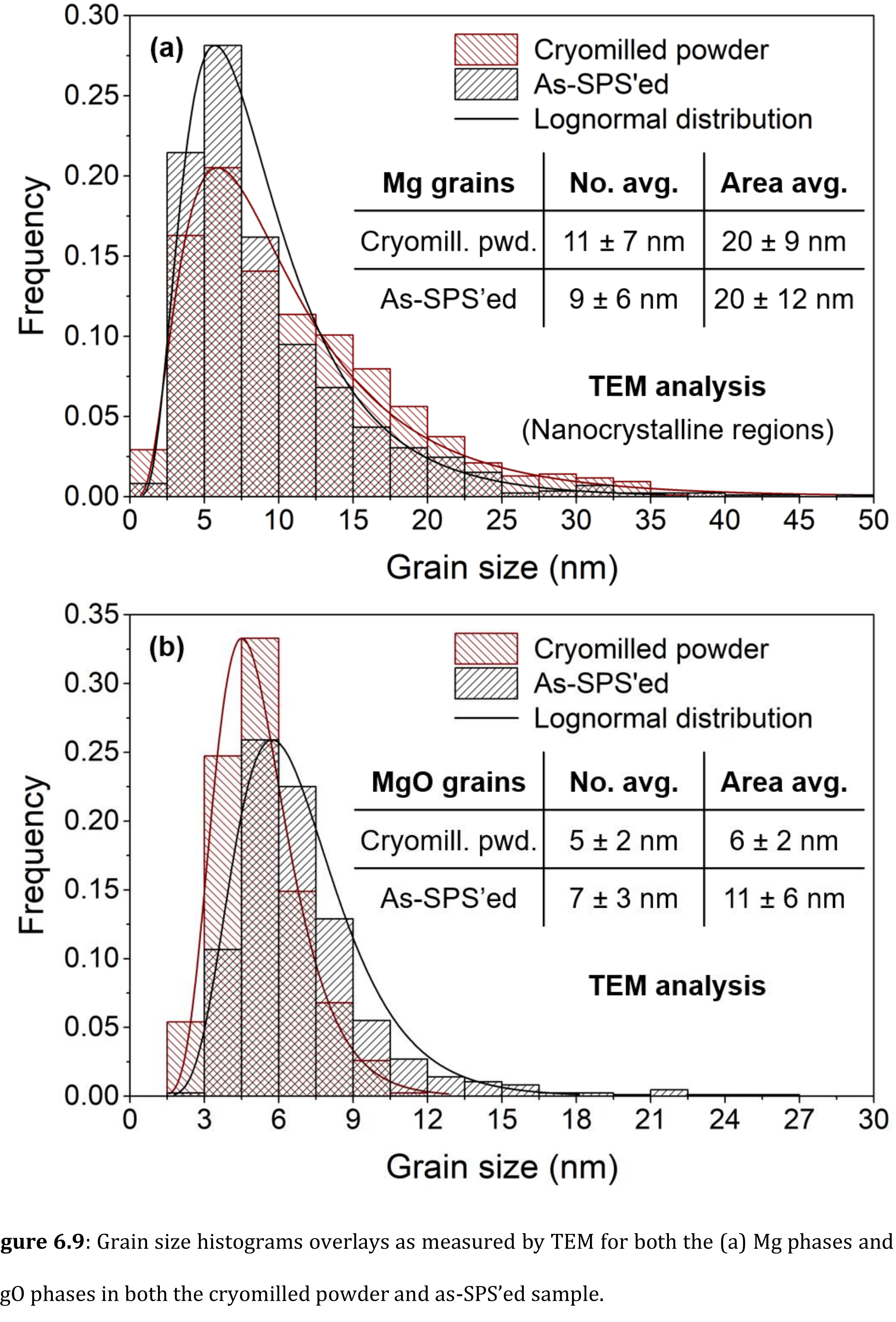

Mg grains	No. avg.	Area avg.
Cryomill. pwd.	11 ± 7 nm	20 ± 9 nm
As-SPS’ed	9 ± 6 nm	20 ± 12 nm

MgO grains	No. avg.	Area avg.
Cryomill. pwd.	5 ± 2 nm	6 ± 2 nm
As-SPS’ed	7 ± 3 nm	11 ± 6 nm

Figure 6.9: Grain size histograms overlays as measured by TEM for both the (a) Mg phases and (b) MgO phases in both the cryomilled powder and as-SPS’ed sample.

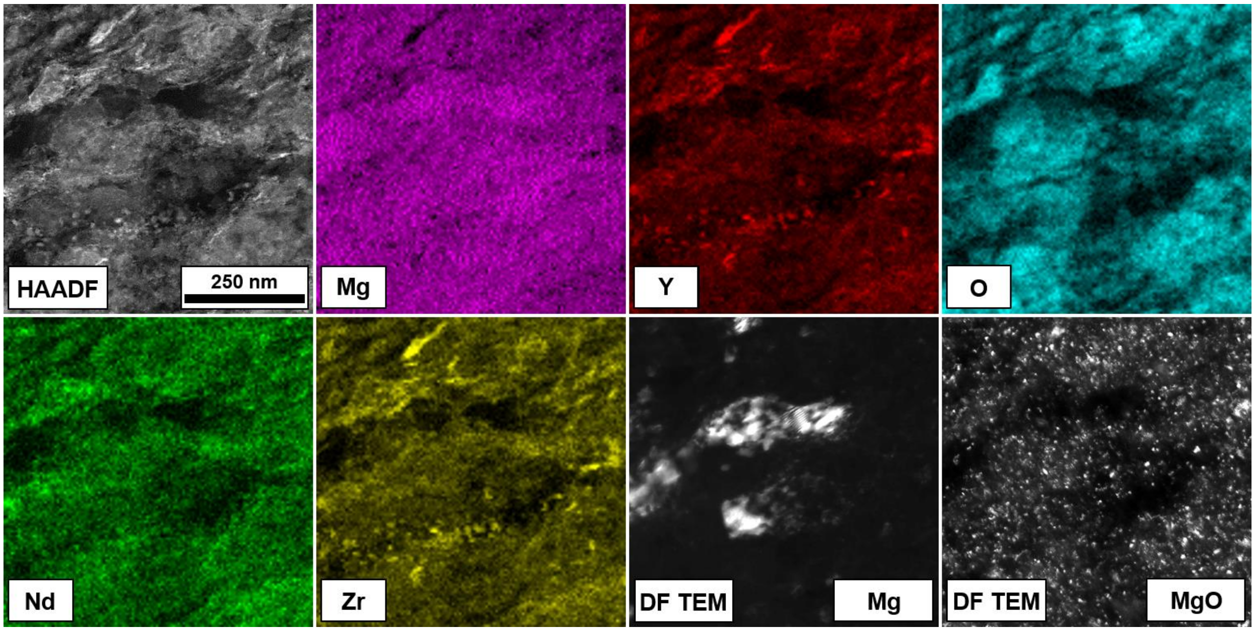

Figure 6.10: STEM-EDS elemental mapping of the as-SPS'ed sample showing the STEM HAADF image of the overall sampling area with the individual mapped elements for Mg, Y, O, Nd, and Zr along with complementary TEM dark-field images (taken from Figure 6.8 and appropriately cropped and scaled) showing the distribution of Mg and MgO grains. All images are of the same region and set to the same scale.

6.2.3 Electron Backscattered Diffraction

In order to characterize the coarser grains in the as-SPS'ed sample, electron backscattered diffraction (EBSD) was used. Figure 6.11(a) shows the EBSD grain map that was generated from the as-SPS'ed sample alongside a similarly scaled SEM image of the as-SPS'ed sample in Figure 6.11(b) (same image that is shown in Figure 6.4). It should be noted that these images are not taken of the same region of the sample. The EBSD data was collected off campus by EBSD Analytical which, for unstated reasons, was unable to simultaneously take an SEM image of the area in which the EBSD grain maps were generated. Additionally, as stated in Chapter 4, due to the limitations of this technique as well as the step size, grain sizes below 100 nm were not able to be measured and appear black in Figure 6.11(a) indicating that no grain data was received from this portion of the sample. Despite this inability to directly correlate the distribution of large grains with the microstructure from an SEM image of the same area that was scanned by EBSD, a reasonable argument can be made that these dark Mg regions as seen in the SEM images have a direct relationship to the size and distribution of the coarse (i.e. measurable) Mg grains as measured by EBSD. It also appears that the coarser of these measured grains appear in small, somewhat isolated clusters, with a disbursement of finer grains throughout the remaining of the microstructure. This observation confirms the results from TEM which shows that the coarse Mg grains were void of MgO as well as RE elements, only containing Mg.

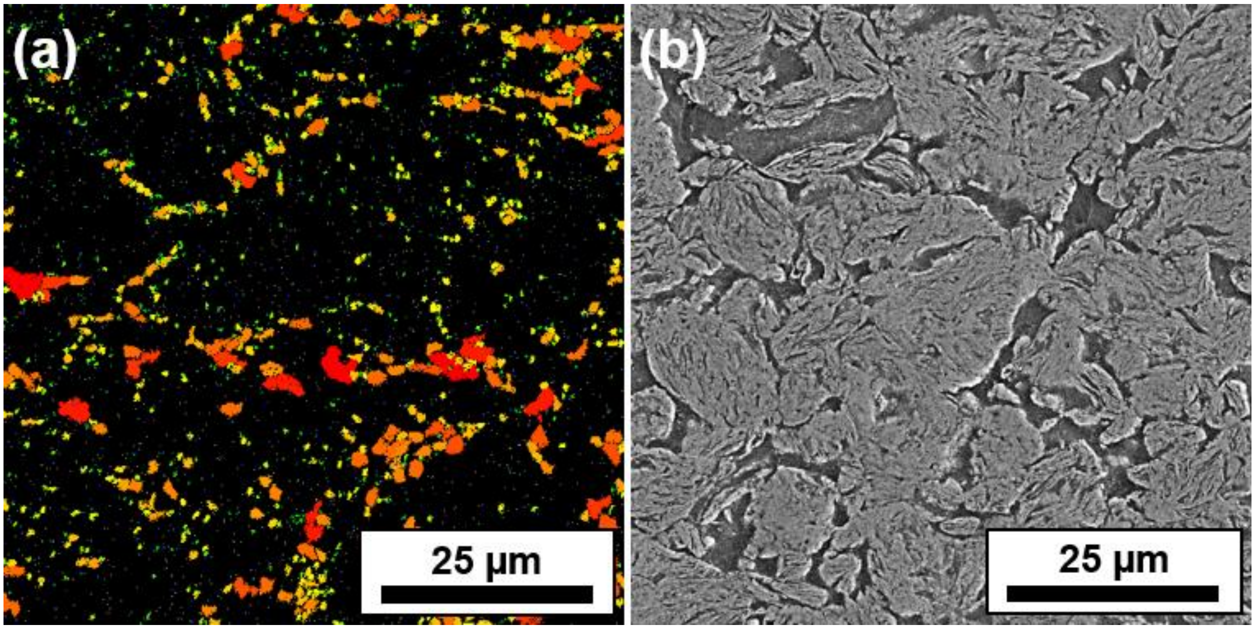

Figure 6.11: (a) Electron backscattered diffraction (EBSD) grain map of the as-SPS'ed sample with different colors corresponding to differing grain size ranges along with (b) a similarly scaled SEM image of the as-SPS'ed sample. *Note*: these images are not of the same region. The SEM image is provided to show similarity between the size and distribution of the measurable grains in the EBSD sample and the dark regions in the SEM image.

Figure 6.12 gives the grain size histogram of the as-SPS'ed sample as measured in the EBSD grain map given in Figure 6.11(a). For this 75 μm x 75 μm scanned area, just over 2,000 grains were measured giving us a large sampling of grains. Even though the histogram only has grain data for grain sizes larger than 100 nm, the histogram still generally follows a lognormal distribution with a number and area average grain size of 0.64 ± 0.59 μm and 1.73 ± 0.86 μm, respectively, with no Mg grains larger than 5 μm being measured. No other phases besides Mg were measured, including MgO, indicating that all of the MgO grains were below 100 nm which confirms the TEM results which indicated that no MgO grains over 50 nm were detected, proving that the MgO grains are very narrowly distributed.

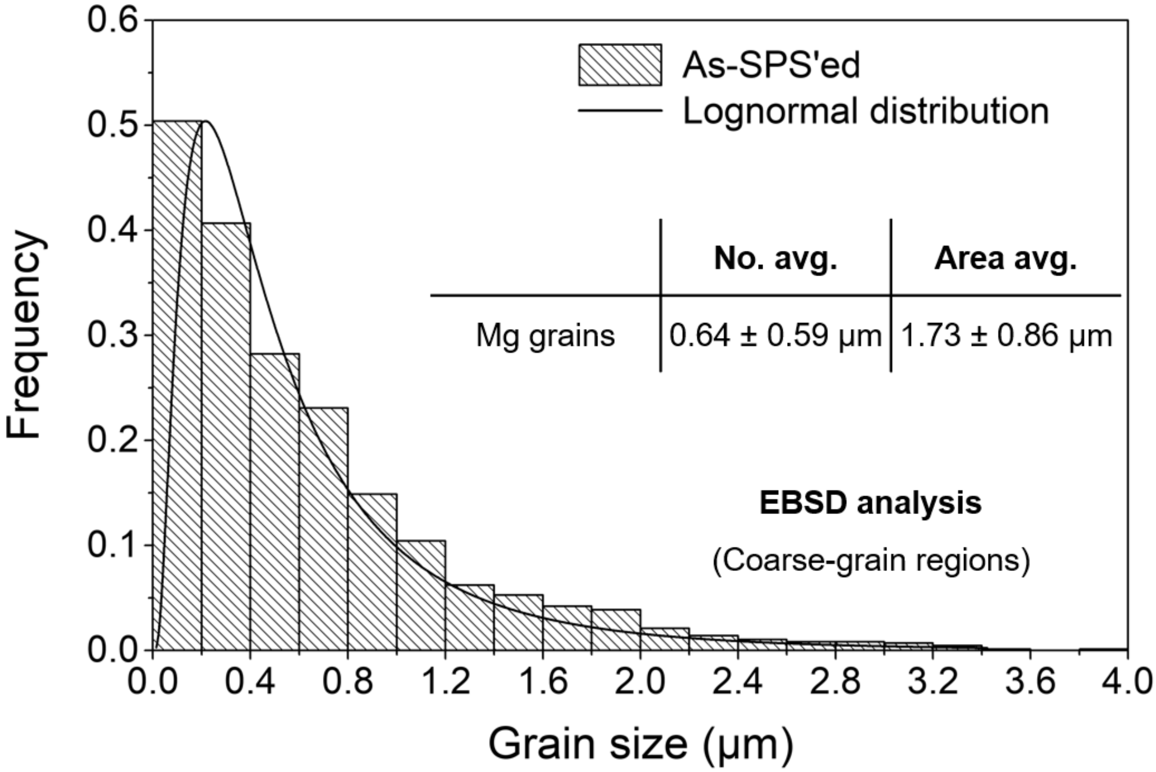

Figure 6.12: Grain size histogram as measured by EBSD for the Mg phase in the as-SPS'ed sample. *Note*: data was acquired with a step size of 100 nm, meaning that grains smaller than 100 nm were not able to be detected.

6.3 Mechanical Properties

6.3.1 Elastic Modulus and Hardness

To further investigate the mechanical properties of the as-SPS'ed sample, nanoindentation was performed. Testing was performed on the as-SPS'ed sample with 50 indents being performed, resulting in a measured elastic modulus and hardness value of 58.4 ± 3.6 GPa and 1.26 ± 0.13 GPa, respectively. It should be noted that when calculating the elastic modulus, a Poisson ratio of 0.3 was assumed. The first thing to note of these results is that the elastic modulus is considerably higher than pure Mg which is 45 GPa. The measured elastic modulus of the as-SPS'ed sample is 58.4 GPa which is 30% higher than pure Mg. However, this result is not that surprising considering the fact that the material contains a non-inconsequential amount of MgO which could be resulting in this high elastic modulus. The high hardness value of 1.26 GPa also suggest that the material has a high yield strength. The standard convention of dividing the hardness by 3 to get the yield strength [#] gives a yield strength of 420 MPa. However, the compressive yield strength will have to be obtained via compressive testing before a yield strength value can be quoted.

In order to determine the effect of the finely dispersed MgO particles on the elastic properties of the as-SPS'ed sample, we will need an equation which relates the elastic properties of both Mg and MgO. Such an equation is given below in Equation 6.1 [66]:

$$E = \frac{E_{Mg}\left[E_{Mg} f_{Mg} + E_{MgO}\left(f_{MgO} + 1\right)\right]}{E_{MgO} f_{Mg} + E_{Mg}\left(f_{MgO} + 1\right)} \qquad Equation\ 6.1$$

where E is the elastic modulus of the composite material (i.e. the as-SPS'ed sample), f_{Mg} and f_{MgO} are the volume fraction of Mg and MgO and E_{Mg} and E_{MgO} are the elastic moduli of Mg and MgO with their respective values of 45 GPa and 300 GPa [67].

In order to estimate the volume fraction of MgO, the semi-quantitative SEM-EDS data given in Table 6.5 was used which showed that oxygen contributed to about 15 at. % (10 wt. %). Using this 15 at. % value along with the assumption that all of the oxygen is participating in MgO with all of the RE elements elementally distributed to the grain boundaries, it is possible to estimate the volume fraction using a simple volume fraction equation as given in Equation 6.2:

$$f_{MgO} = \frac{\frac{0.15\ M_{MgO}}{\rho_{MgO}}}{\frac{0.70\ M_{Mg}}{\rho_{Mg}} + \frac{0.15\ M_{MgO}}{\rho_{MgO}}} \qquad \text{Equation 6.2}$$

where f_{MgO} is the volume fraction of MgO, M_{Mg} and M_{MgO} are the respective molar masses for Mg and MgO, ρ_{Mg} and ρ_{MgO} are the respective densities of Mg and MgO, and the values 0.15 and 0.70 come from the assumption that 15% of the Mg atoms are participating in the formation of MgO leaving only 70% of the Mg atoms to participate in Mg. In addition, this calculation also assumes that the Mg and MgO are equal to their pure counterparts with the molar mass and density for Mg of 24.3 g/mol and 1.74 g/cm^3, respectively, and a molar mass and density for MgO of 40.3 g/mol and 3.58 g/cm^3, respectively.

Using Equation 6.2 and plugging in the values given, we calculate that the MgO volume fraction is 0.15 meaning that the MgO particles compromise about 15% of the as-SPS'ed sample by volume which seems like a reasonable number given all of the other data. Taking this volume fraction, we can now calculate the elastic modulus of this composite by using Equation 6.1 which yields a value of 56 GPa which is close enough to the experimentally calculated value of 58.4 ± 3.6 GPa to feel confident in the results. In order to get both the calculated and experimental values to match, a MgO volume fraction of 0.18 had to be used which suggests that the true volume fraction is most likely between 15% and 20%.

6.3.2 Compressive Yield Strength

Compression testing, both conventional bulk compression testing (Instron) as well as microcompression testing compression (Hysitron PicoIndenter) via the compression of micropillars, was conducted in order to calculate the compressive yield strength of the as-SPS'ed sample. Both of these test methods were also conducted so that the microcompression testing could be established as an accurate analogue for standard bulk compression testing for later testing. Due to the limited supply of the as-SPS'ed material, we were only able to make small number of samples for bulk compression testing and would need to rely on the microcompression testing results as an analogue for testing the heat-treated samples.

These compression results are presented in Figure 6.13 which has both the results from the bulk compression and the results from micro-compression. These results are in quite good agreement with each other, with a compressive strength from the bulk testing of 320 ± 4 MPa and a compressive strength for the micro-compression of 325 ± 19 MPa with 5 samples being tested for both compression methods with both having a nominal strain rate of 2×10^{-3} s^{-1}. Not only do these results show a very high compressive yield strength, they provide high confidence that the micro-compression testing is an accurate and reliable analogue for standard bulk compression testing which can be used to calculate the bulk compressive strength for later test specimen, mainly the heat-treated samples. These results also show that we were successful in our goal to make a high-strength Mg alloy with the nanocrystalline grains indeed providing a substantial strength in the material. The reported compressive yield strength for bulk WE43 after a T6 heat treatment is 190 MPa, showing that the current process of cryomilling and SPS consolidation offers a 130 MPa improvement compared to the traditional processing. Although this is not a quite fair comparison considering the cryomilling process introduced nanocrystalline MgO particles creating a bulk nanocomposite, it serves as a baseline comparison.

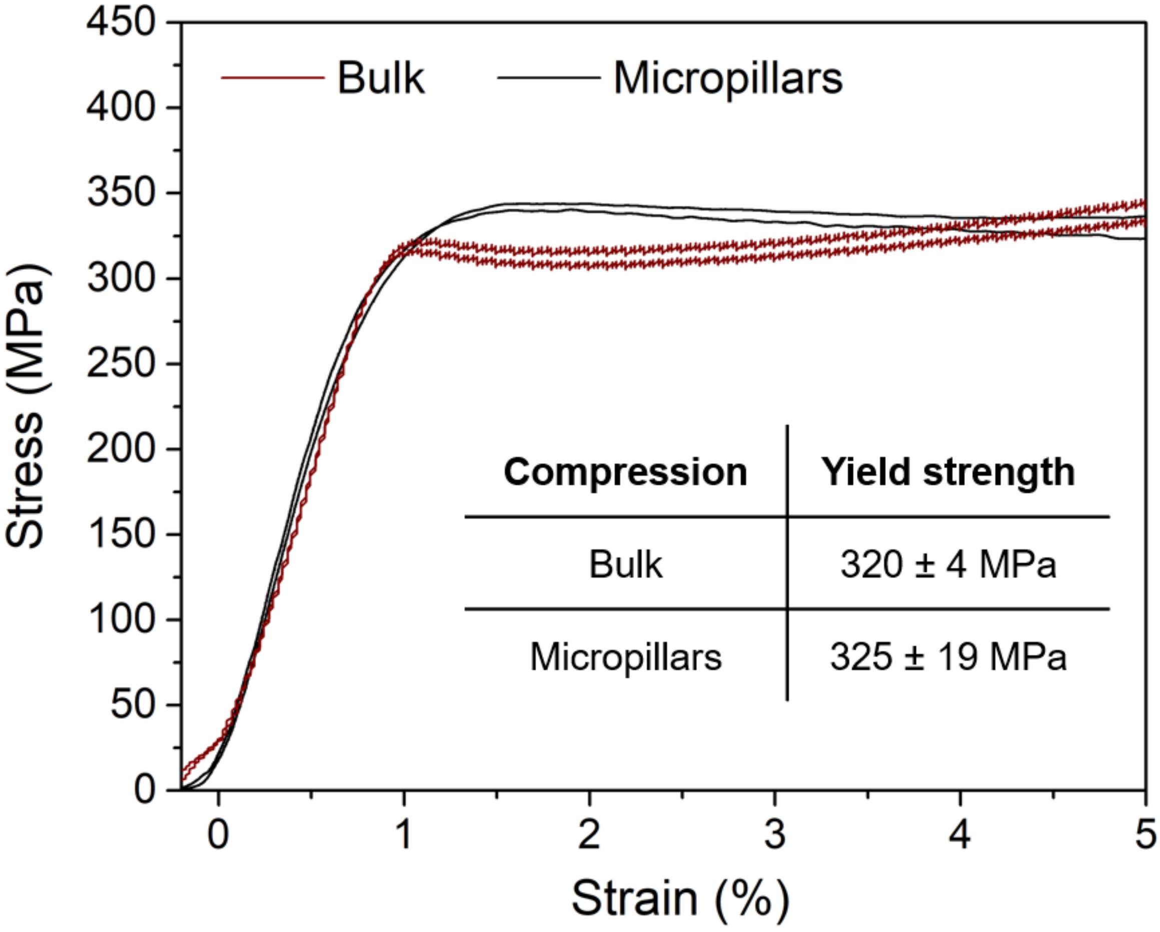

Compression	Yield strength
Bulk	320 ± 4 MPa
Micropillars	325 ± 19 MPa

Figure 6.13: Compression results for the as-SPS'ed sample for both bulk compression testing and micropillar compression testing along with their respective compressive yield strengths.

It should also be noted that in addition to the high strength, the as-SPS'ed sample also shows quite a bit of elongation as evidenced in Figure 6.14 which shows two side-by-side SEM images of a pillar before and after being compressed to a strain of about 10%. This result is unexpected since the one major drawback of nanocrystalline materials is that they do not exhibit much ductility since they do not have the ability to work harden. The ability of the as-SPS'ed sample to accommodate so much compressive ductility must be due to the bimodal grain size distribution with the coarser Mg grains providing ductility with their ability to work harden with the nanocrystalline grains providing the majority of the strength.

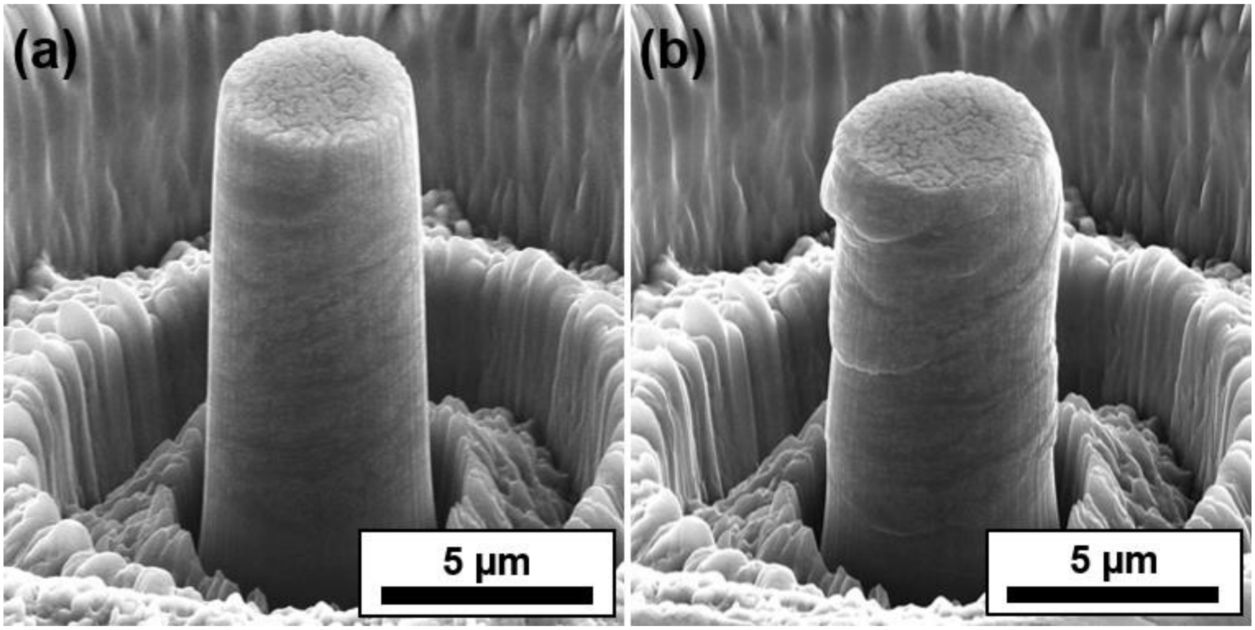

Figure 6.14: SEM images of a single micropillar as fabricated by FIB both (a) before and (b) after compression to a strain of 10%.

Chapter 7

Thermal Stability of Magnesium-Based Bulk Nanocomposite

7.1 Phase Identification and Crystallite Size

7.1.1 Conventional X-Ray Diffraction

Figure 7.1 shows the conventional XRD spectra for both the as-SPS'ed sample and sample heat-treated at 450 °C for 100 hours, the most aggressive of heat treatments the as-SPS'ed sample was subjected to. From the XRD spectrum, it is clear that no additional phases were produced as a result of the heat treatment, with Mg and MgO being the only phases present in both samples. Besides the slight sharpening of the MgO peaks, there is no major differences in the two spectra. The sharpening of the MgO is most likely due to the result of coalescing and coarsening of MgO grains due to the prolonged heat treatment. Table 7.1 shows the lattice constants for Mg as well as the crystallite sizes for both the Mg and MgO phases as calculated from the XRD spectra. From this table, we see that there is no discernable difference from the Mg lattice parameters and no substantial change in the crystallite sizes for both the Mg and MgO phases before and after the heat treatment at 450 °C for 100 hours. The crystallite size for Mg only marginally increases for the heat treated at 450 °C for 100 hours sample, increasing from 79 ± 4 nm to 87 ± 6 nm, indicating some minor grain growth. For MgO, there is only a slight increase in crystallite size, increasing from 2 ± 1 nm to 3 ± 1 nm which is within the margin of error. However, the peak sharpening from the XRD spectra indicate a noticeable difference between the MgO peaks before and after heat treatment. It is possible that the heat treatment has caused the formation of a bimodal grain size distribution for the MgO phase.

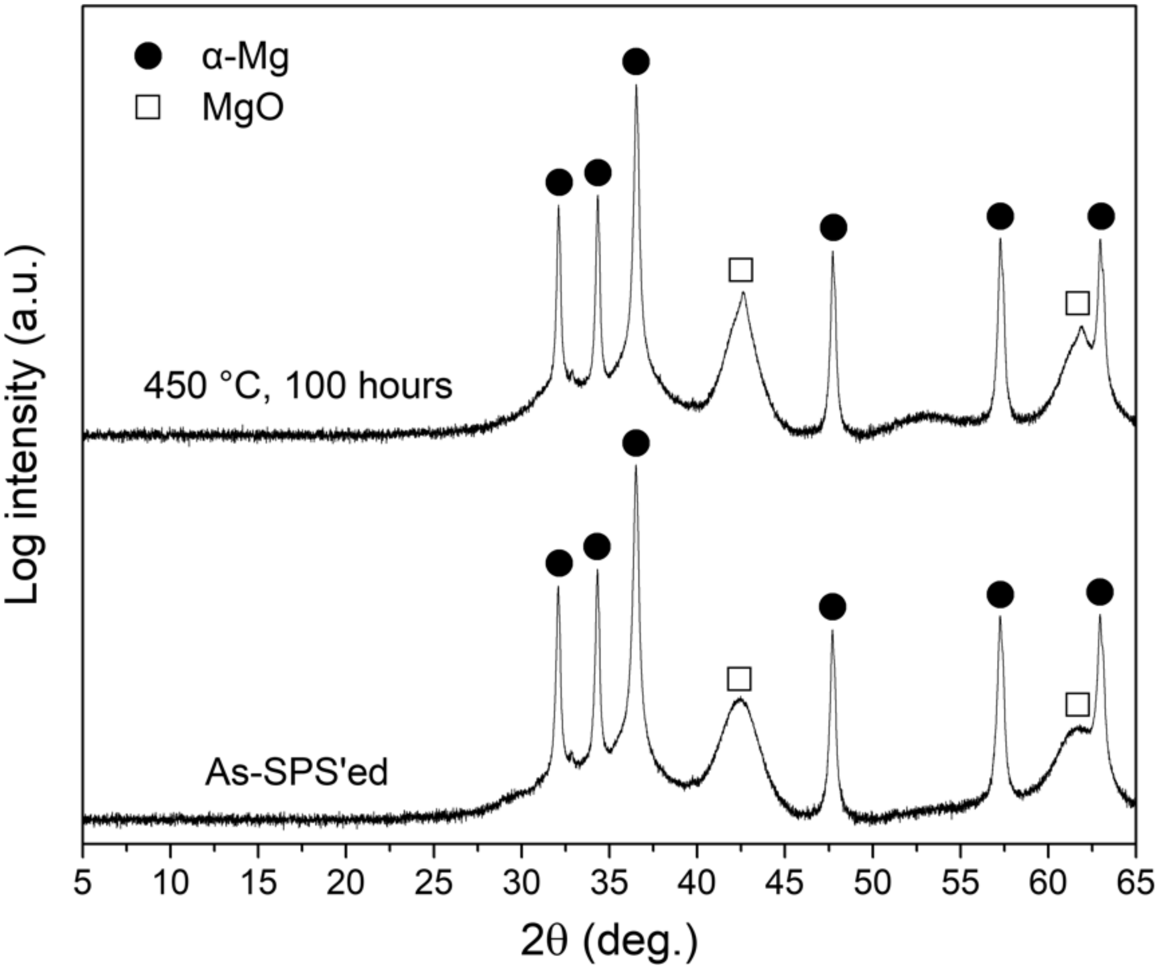

Figure 7.1: Conventional XRD spectra for both the as-SPS'ed sample and the sample heat-treated at 450 °C for 100 hours.

Table 7.1: Relevant lattice constants and crystallite sizes as calculated from the conventional XRD spectra for the as-SPS'ed sample and the sample heated at 450 °C for 100 hours given in Figure 7.1.

	Mg Lattice Parameters			**Crystallite size (nm)**	
	a (nm)	c (nm)	c/a	Mg	MgO
As-SPS'ed	0.3215 ± 0.0004	0.5215 ± 0.0004	1.622 ± 0.003	79 ± 4	2 ± 1
450 °C, 100 hrs.	0.3215 ± 0.0003	0.5219 ± 0.0002	1.623 ± 0.002	87 ± 6	3 ± 1
Pure Mg	0.3209	0.5210	1.624	-	-

Other than the conventional XRD data for the sample heat-treated at 450 °C for 100 hours, comparative XRD spectra at 150 °C for 2 and 100 hours as well as comparative XRD spectra 450 °C for 2 and 100 hours given in Figure 7.2 and Figure 7.3, respectively, along with their respective lattice constants for Mg as well as the crystallite sizes for both the Mg and MgO phases listed in Table 7.2 and Table 7.3. From these results it is apparent that the material is extremely stable over various heat treatments with no noticeable differences in either lattice parameters or crystallite size. The noticeable difference between the four selected heat-treated samples being, as previously discussed, the peak sharpening in relation to the MgO peak for the sample heat treated at 450 °C for 100 hours. It is possible that this particular heat treatment has caused the formation of a bimodal grain size distribution for the MgO phase.

In addtion to the Mg crystallite measurments for the four heat-treated samples just described, Mg crystallite measurements for all of the four temperature regimes (150, 250, 350, and 450 °C) for the varying times (2, 4, 8, 16, 32, 64, and 100 hours) were performed. These results are presented in Figure 7.4 along with the summarized data from the four temperature regimes at 100 hours in Table 7.4. These results show the material's remarkable thermal stability across all temperature regimes. It appears that any prolonged heat treatment causes the Mg crystallites to slightly increase and then to stabilize without any further growth, and it appears that even the most modest of heat treatments will initiate this grain coarsening, at least in relation to the crystallite size. It also quite possible that this apparent increase in crystallite size for the heat-treated samples could be due to lattice strain relaxation. Since the lattice strain was assumed to be negligible, no attempt to subtract the peak broadening was undertaken when calculating the crystallite size. This decrease in peak broadening which corresponds to a slightly larger crystallite size, might simply be the result of eliminating the broadening due to strain. This strain relaxation should theoretically be ascertained by a change in lattice parameter, but if the effect is so small as to be within the margin of error of the measurement, it would be difficult to reasonably detect.

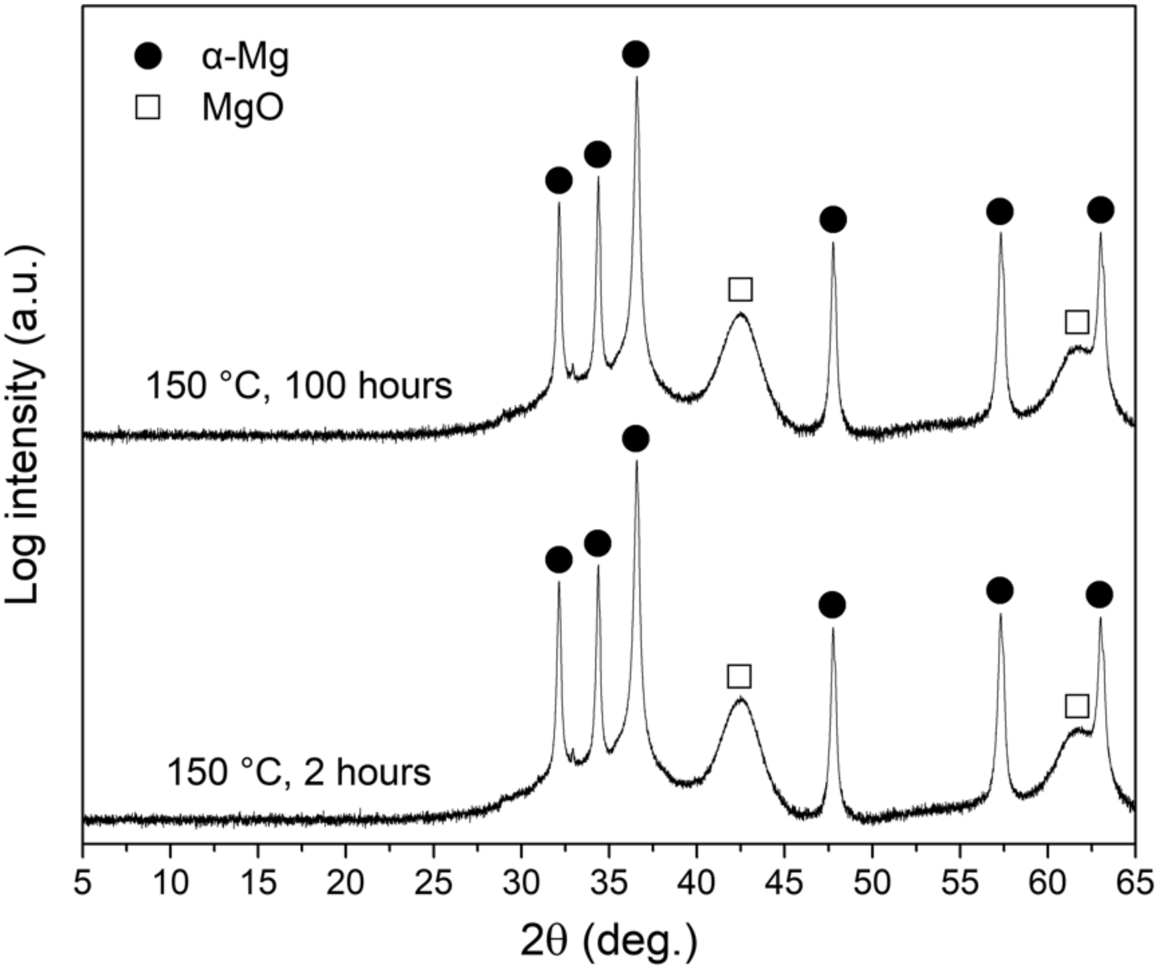

Figure 7.2: Conventional XRD spectra for both the sample heat-treated at 150 °C for 2 hours and the sample heat-treated at 150 °C for 100 hours.

Table 7.2: Relevant lattice constants and crystallite sizes as calculated from the conventional XRD spectra for the samples heat treated at 150 °C for both 2 and 100 hours given in Figure 7.2.

	Mg Lattice Parameters			**Crystallite size (nm)**	
	a (nm)	c (nm)	c/a	Mg	MgO
150 °C, 2 hrs.	0.3213 ± 0.0006	0.5213 ± 0.0004	1.622 ± 0.004	84 ± 2	2 ± 1
150 °C, 100 hrs.	0.3212 ± 0.0003	0.5213 ± 0.0002	1.623 ± 0.002	86 ± 5	2 ± 1
Pure Mg	0.3209	0.5210	1.624	-	-

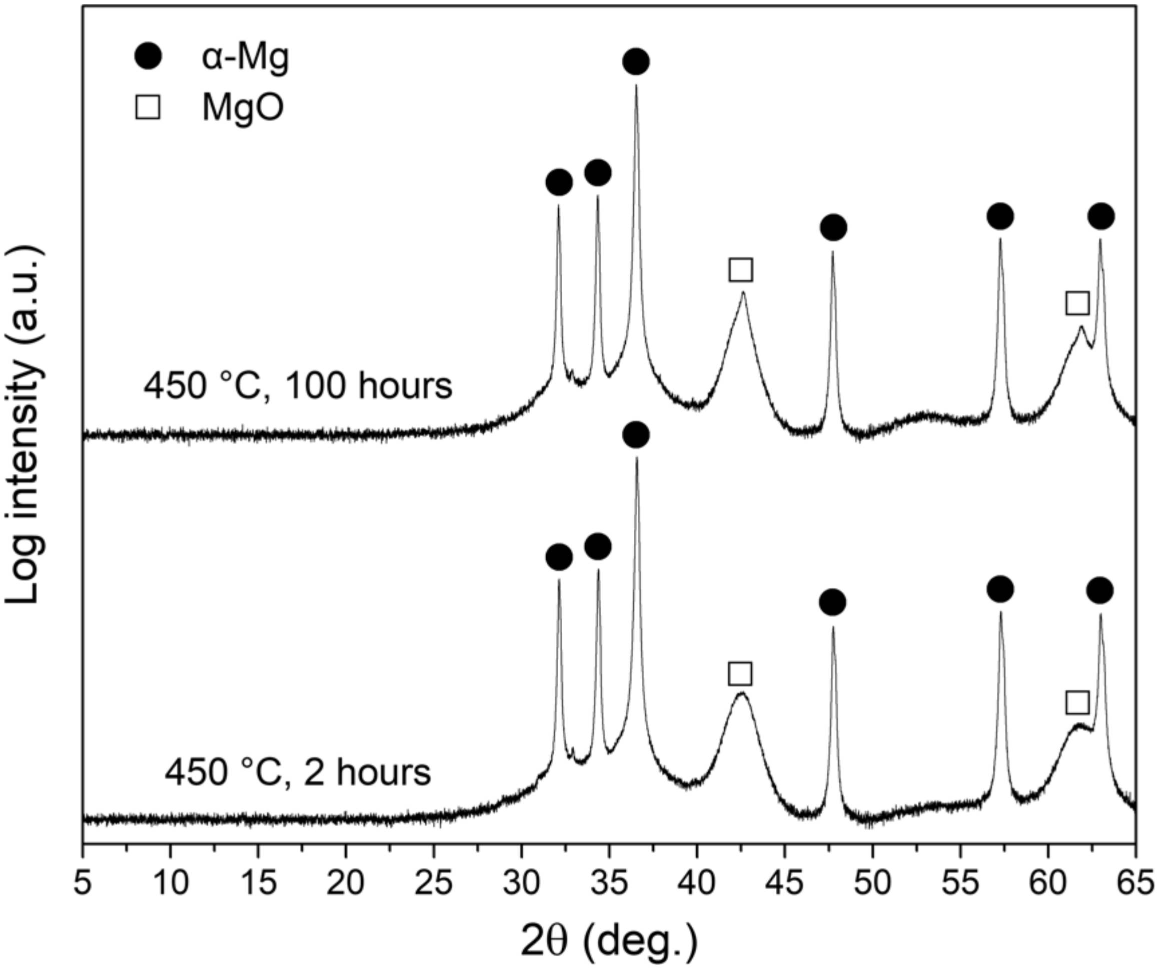

Figure 7.3: Conventional XRD spectra for both the sample heat-treated at 450 °C for 2 hours and the sample heat-treated at 450 °C for 100 hours.

Table 7.3: Relevant lattice constants and crystallite sizes as calculated from the conventional XRD spectra for the samples heat treated at 450 °C for both 2 and 100 hours given in Figure 7.3.

	Mg Lattice Parameters			**Crystallite size (nm)**	
	a (nm)	c (nm)	c/a	Mg	MgO
450 °C, 2 hrs.	0.3213 ± 0.0004	0.5214 ± 0.0004	1.623 ± 0.003	89 ± 3	2 ± 1
450 °C, 100 hrs.	0.3215 ± 0.0003	0.5219 ± 0.0002	1.623 ± 0.002	87 ± 6	3 ± 1
Pure Mg	0.3209	0.5210	1.624	-	-

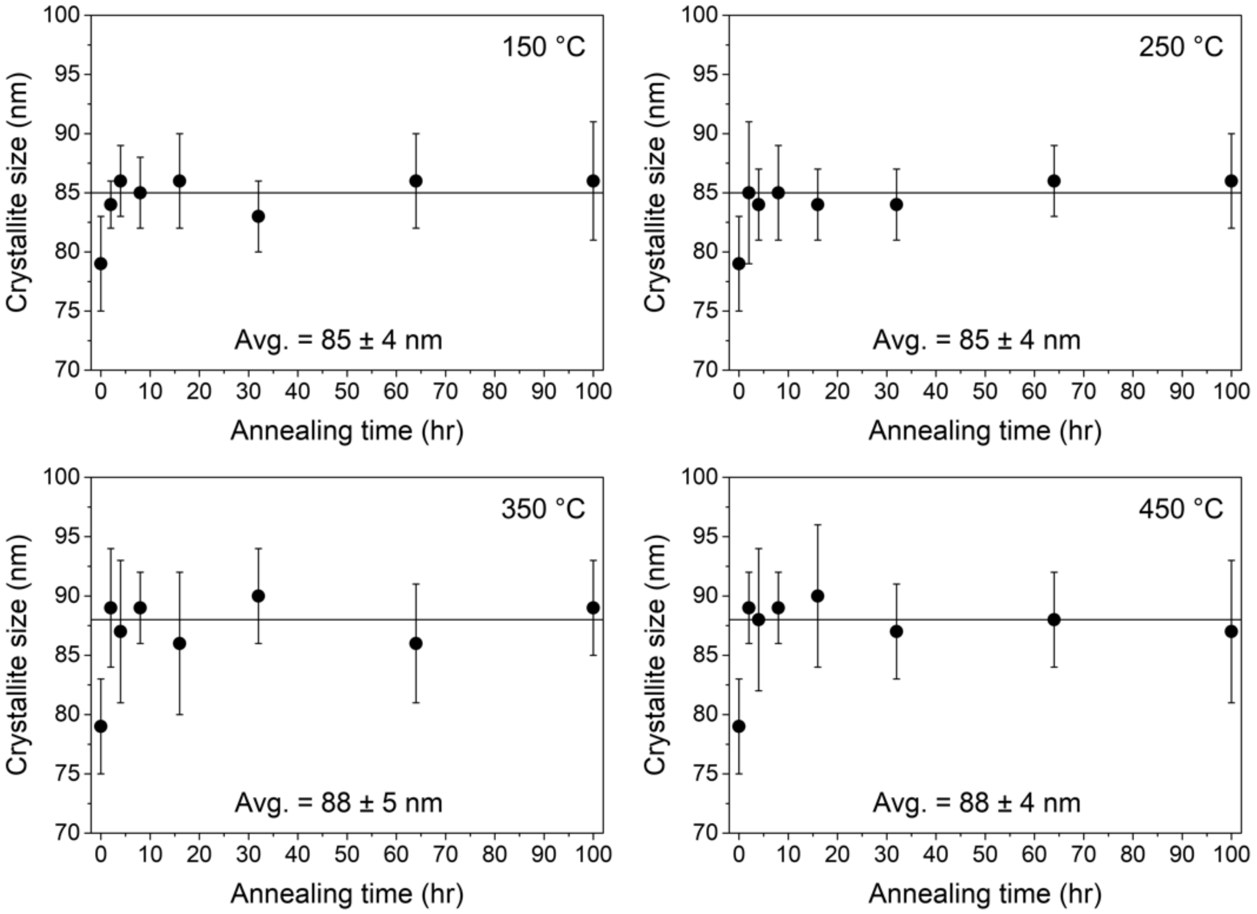

Figure 7.4: Crystallite size as measured by XRD for the as-SPS'ed sample and samples heat-treated at 150, 250, 350, and 450 °C for 2, 4, 8, 16, 32, 64, and 100 hours.

Table 7.4: Homologous temperature and crystallite size summary as measured by XRD for the as-SPS'ed sample and samples heat treated at 150, 250, 350, and 450 °C for 100 hours.

	T/T_m*	**Crystallite size (nm)**
As-SPS'ed	-	79 ± 4
150 °C, 100 hrs.	0.52	86 ± 5
250 °C, 100 hrs.	0.64	86 ± 4
350 °C, 100 hrs.	0.77	89 ± 4
450 °C, 100 hrs.	0.89	87 ± 6

* Calculated using a melting temperature of 540 °C (813 K).

7.1.2 Synchrotron X-Ray Diffraction

In addition to conventional XRD, synchtrotron XRD was also used to confirm our results from conventional XRD. Figure 7.3 shows the spectra from synchrotron XRD for both the as-SPS'ed sample and sample heat-treated at 450 °C for 100 hours. Results from both the conventional and synchrotron XRD are in good agreement, with no additonal phases forming as a result of the heat treatment. The MgO peak sharpening is also confirmed, with the same result appearing in the synchrotron data. Table 7.2 shows the lattice constants and crystallite sizes for both the Mg and MgO phases as calculated from the spectra in Figure 7.2. These results are also similar to the results from conventional XRD. There is no perceived difference in the lattice parameters and no significant differences between the crystallite sizes for the Mg and MgO phases. Due to beam time restrictions, only one sample was tested for each test condition so standard deviation values are not possible. It should be noted that there is a significant difference between the apparent crystallite size of Mg between both techniques. This value is off less importance, however, compared to the relative values between them.

Other than the conventional XRD data for the sample heat treated at 450 °C for 100 hours, comparative XRD spectra at 150 °C for 2 and 100 hours as well as comparative XRD spectra 450 °C for 2 and 100 hours given in Figure 7.5 and Figure 7.6, respectively, along with their respective lattice constants for Mg as well as the crystallite sizes for both the Mg and MgO phases listed in Table 7.5 and Table 7.6. These results are extremely similar to the results of the conventional XRD data, showing no noticeable difference for the Mg lattice parameters or the Mg and MgO crystallite sizes between the as-SPS'ed sample and the heat treated samples, with exception to the sample heat-treated at 450 °C for 100 hours as just mentioned in the previous paragraph which showed a slight increase of the MgO crystallites in the as-SPS'ed sample increasing from 4 nm to 6 nm in the sample heat treated at 450 °C for 100 hours.

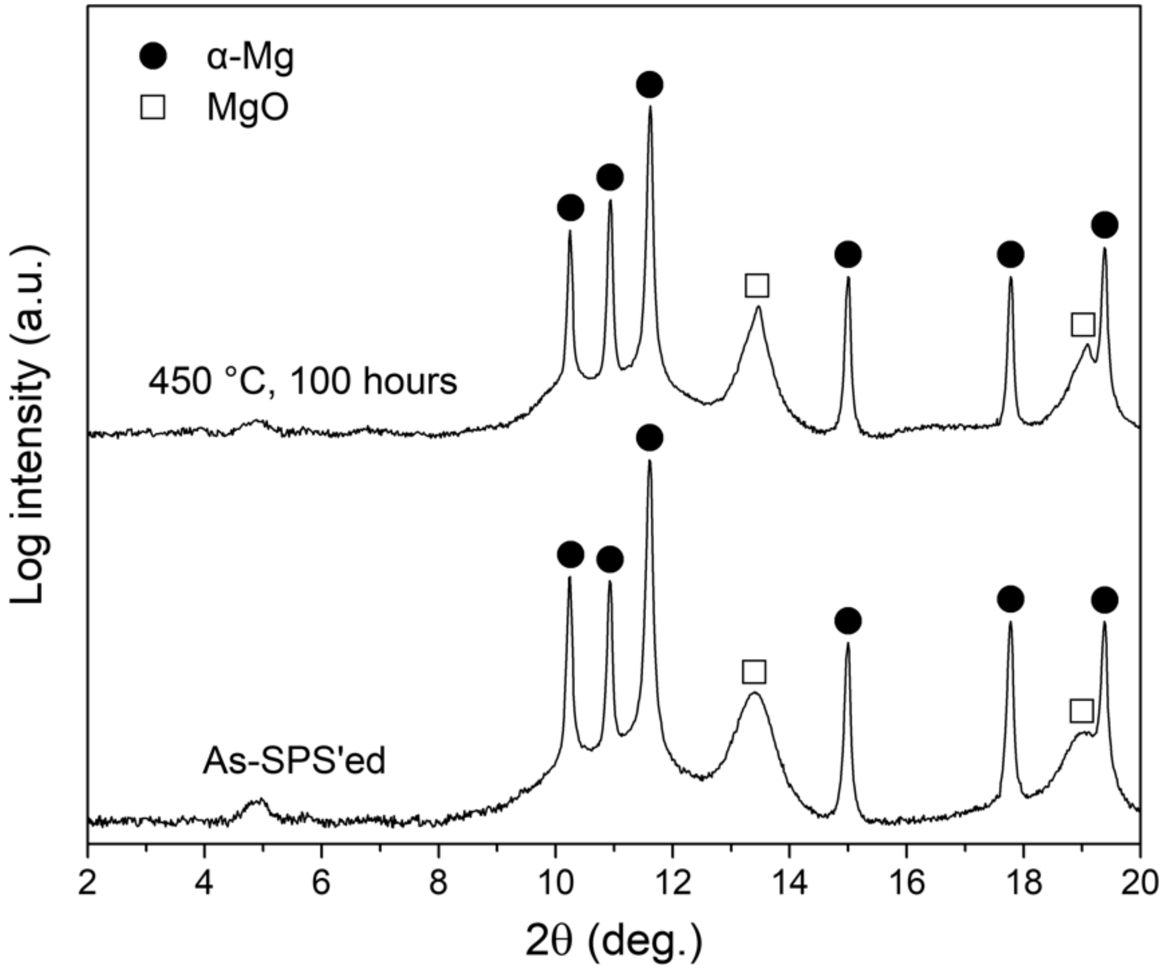

Figure 7.5: Synchrotron XRD spectra for both the as-SPS'ed sample and sample heat-treated at 450 °C for 100 hours.

Table 7.5: Relevant lattice constants and crystallite sizes as calculated from the synchrotron XRD spectra given in Figure 7.5.

	Mg Lattice Parameters			**Crystallite size (nm)**	
	a (nm)	c (nm)	c/a	Mg	MgO
As-SPS'ed	0.3210	0.5209	1.623	37	4
450 °C, 100 hrs.	0.3209	0.5206	1.622	39	6
Pure Mg	0.3209	0.5210	1.624	-	-

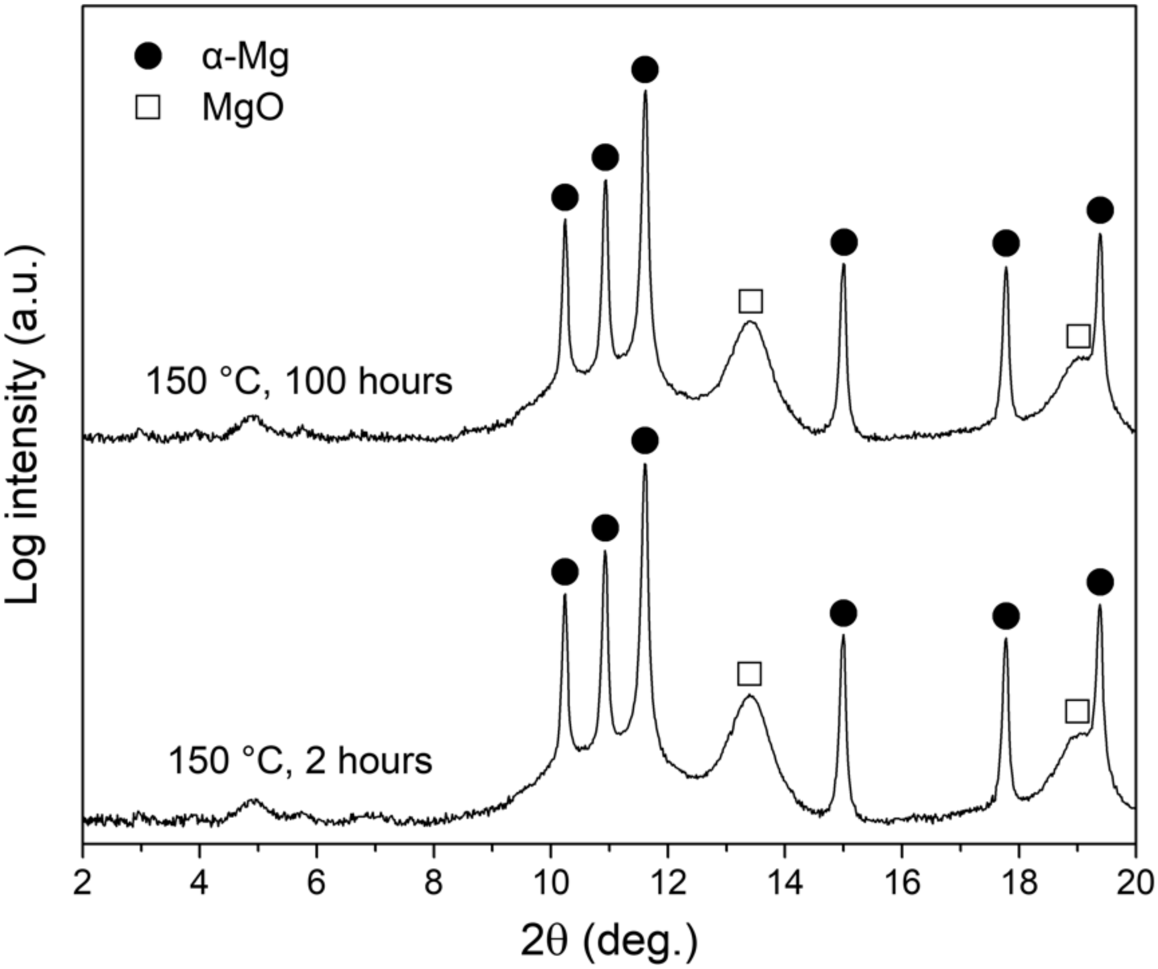

Figure 7.6: Synchrotron XRD spectra for both the sample heat-treated at 150 °C for 2 hours and the sample heat-treated at 150 °C for 100 hours.

Table 7.6: Relevant lattice constants and crystallite sizes as calculated from the synchrotron XRD spectra given in Figure 7.6.

	Mg Lattice Parameters			**Crystallite size (nm)**	
	a (nm)	c (nm)	c/a	Mg	MgO
150 °C, 2 hrs.	0.3210	0.5209	1.623	37	4
150 °C, 100 hrs.	0.3210	0.5207	1.622	40	4
Pure Mg	0.3209	0.5210	1.624	-	-

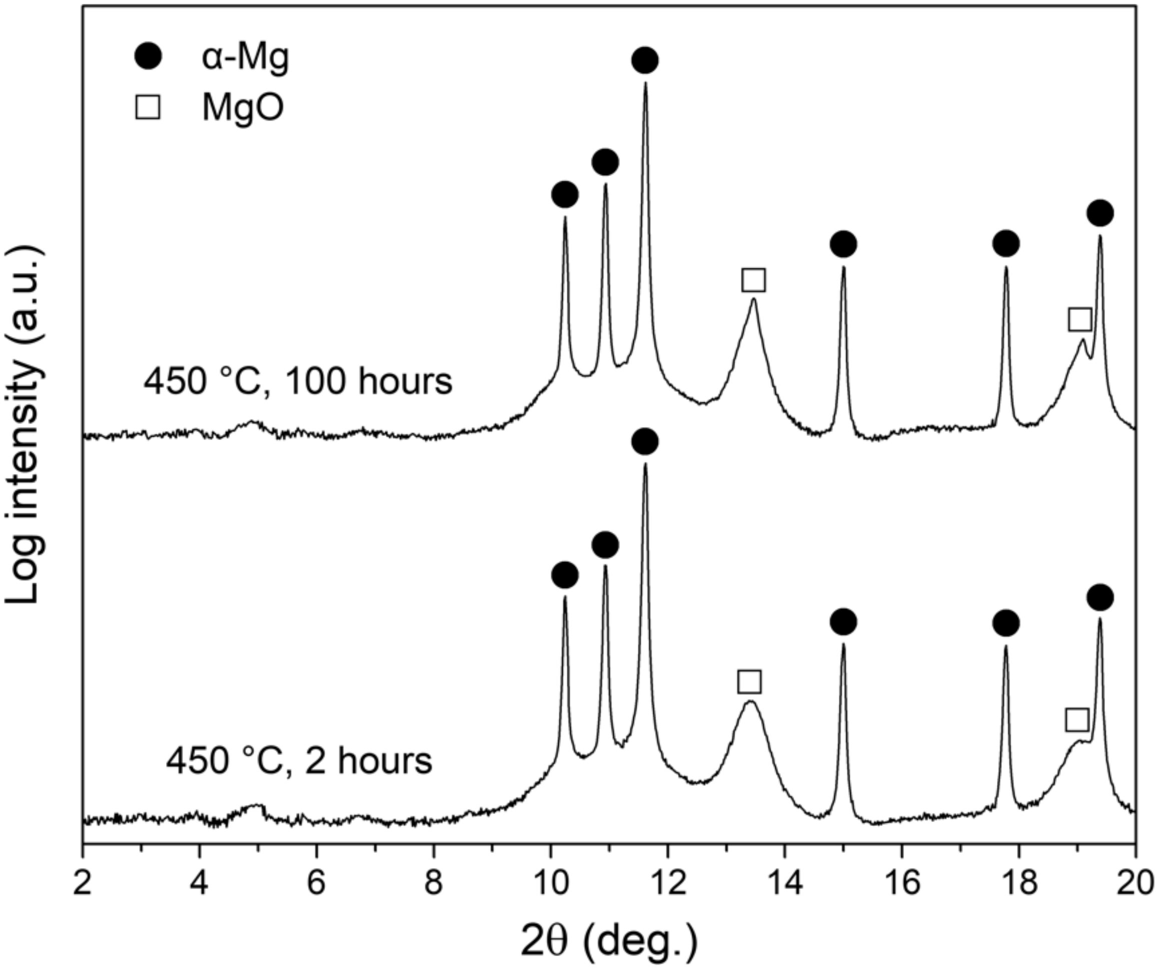

Figure 7.7: Synchrotron XRD spectra for both the sample heat-treated at 450 °C for 2 hours and the sample heat-treated at 450 °C for 100 hours.

Table 7.7: Relevant lattice constants and crystallite sizes as calculated from the synchrotron XRD spectra given in Figure 7.7.

	Mg Lattice Parameters			**Crystallite size (nm)**	
	a (nm)	c (nm)	c/a	Mg	MgO
450 °C, 2 hrs.	0.3210	0.5207	1.622	38	4
450 °C, 100 hrs.	0.3209	0.5206	1.622	39	6
Pure Mg	0.3209	0.5210	1.624	-	-

7.2 Microstructure

7.2.1 Scanning Electron Microscopy

Figure 7.8 presents side-by-side SEM images showing the microstructures of both the as-SPS'ed sample and the sample heated at 450 °C for 100 hours. According to XRD, there was a slight coarsening of both the Mg and MgO phases. However, this coarsening is not seen in the microstructural SEM images with no discernable difference between the two microstructures. The coarse Mg grains and nanocrystalline regions consisting of Mg and MgO appear to be in the same relative proportions in both SEM images, with no noticeable growth of the coarser of the Mg grains. The finely dispersed MgO particles/grains seem to be pinning down the grains, stabilizing the grain structure at very high temperatures. In order to confirm this, however, additional characterization techniques would have to be used to directly measure the grain size distribution.

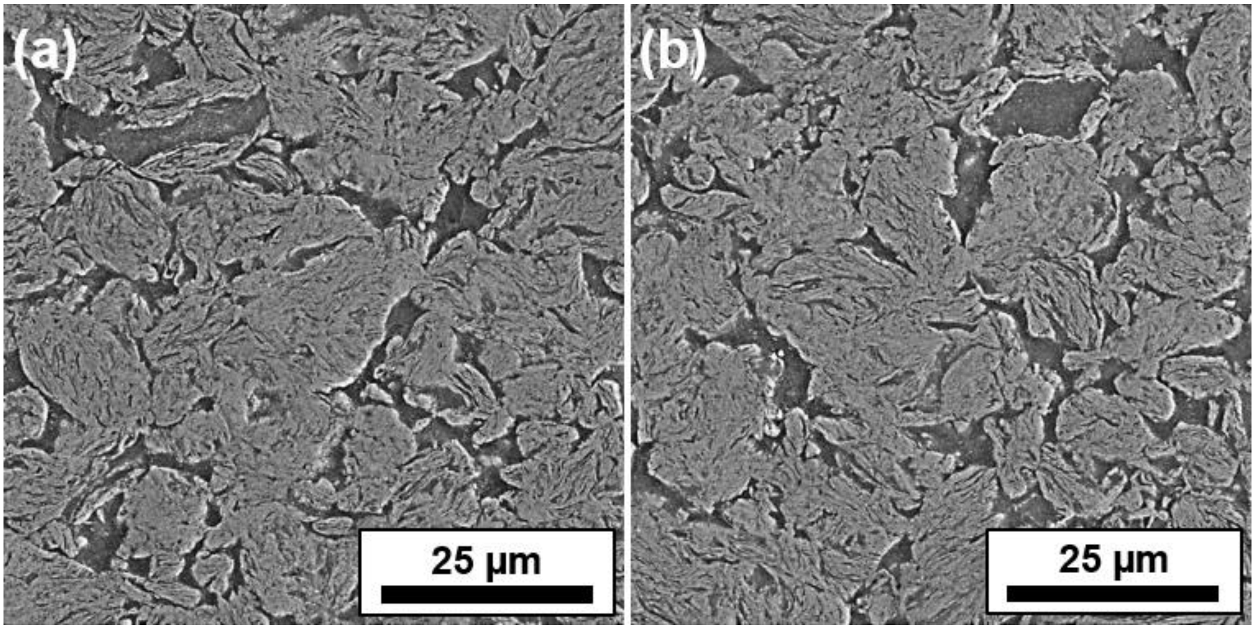

Figure 7.8: SEM microstructural images of (a) the as-SPS'ed sample and (b) the sample heat-treated at 450 °C for 100 hours.

7.2.2 Electron Backscattered Diffraction

In order to confirm the thermal stability, EBSD was used to characterize the coarser grains. Figure 7.9 shows a side-by-side EBSD grain size mapping images showing the distribution of grains for both the as-SPS'ed sample and sample heated at 450 °C for 100 hours. From first glance of these images, there does not seem to be any discernable difference between the grain sizes of the two samples. This is further proved in Figure 7.10 which graphs a histogram overlay of the raw EBSD grain sizes of both the as-SPS'ed sample and the sample heat-treated at 450 °C for 100 hours. This data confirms that there is no distinguishable difference between the two grain size distributions with the number grain size average of the as-SPS'ed and sample heated 450 °C for 100 hours being 0.64 ± 0.59 μm and 0.57 ± 0.54 μm, respectively, and the area grain size average of the as-SPS'ed and sample heated 450 °C for 100 hours being 1.73 ± 0.86 μm and 1.69 ± 0.94 μm, respectively. A complete EBSD grain size analysis of all the heat-treated samples heated for 100 hours at 150, 250, 350, and 450 °C is listed in Table 7.8 with the number and area grain size averages of each sample which shows no statistical differences. Additionally, for all five of these samples measured, no grains over 5 μm in diameter were observed.

This EBSD analysis is the first direct evidence that no grain growth as occurred for the heat-treated samples, at least in relation to Mg grains over 100 nm. Also, due to the relative areas of undetectable Mg grains (i.e. the black regions of the graphs), the coarser grains do not seem to comprise a larger volume fraction of the material. This is also evident in the SEM images (Figure 7.8) showing that these lighter nanocrystalline regions comprise about the same area fraction of the image both before and after heat treatment. This should suggest that the nanocrystalline Mg grains (unable to be measured in this technique), are thermally stable as well. And it might well be that the thermal stability of these nanocrystalline grains is the reason for the thermal stability of the coarse Mg grains, constraining their growth.

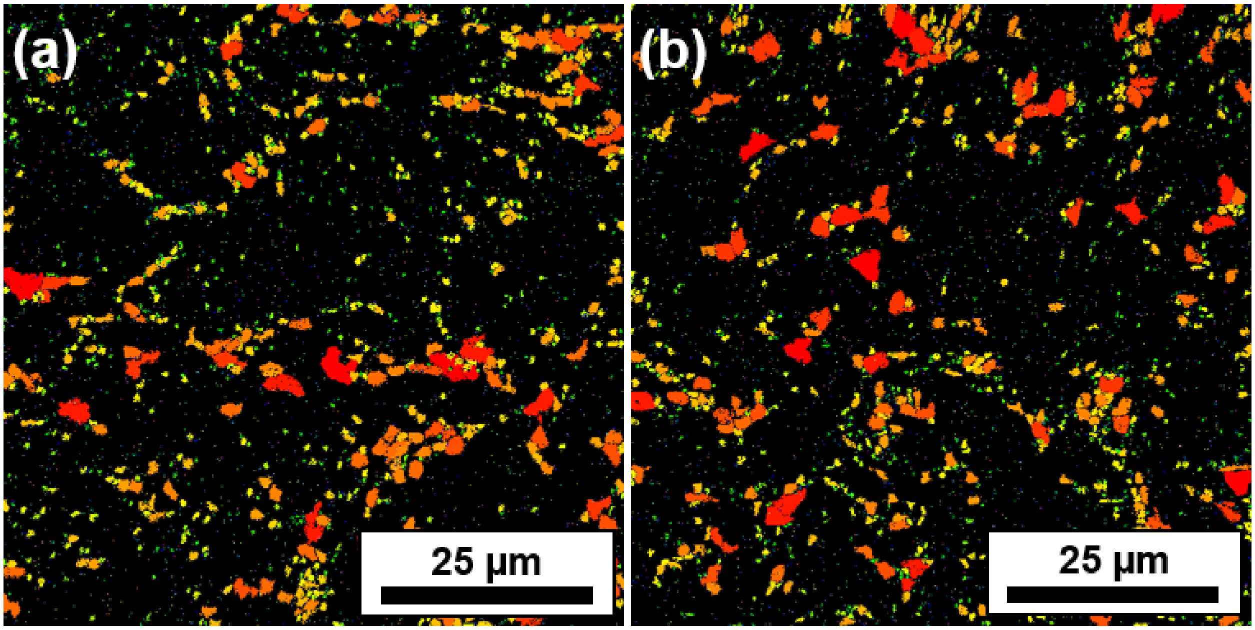

Figure 7.9: EBSD grain size mapping of (a) the as-SPS'ed sample and (b) the sample heat-treated at 450 °C for 100 hours, with different colors corresponding to particular grain size ranges.

As previously speculated, the MgO particles might be the reason for the overall thermal stability of the material, acting as pinning particles at the Mg grain boundaries and inhibiting grain growth. This pinning effect was discussed by Zener [68] who proposed that the driving force for grain growth due to the grain boundary curvature of these grains would be counteracted by a pinning force exerted by particles along these grains boundaries [69]. This effect was quantified by Zener, given in Equation 7.1, which stipulates that normal grain growth would be completely inhibited once a critical grain size was achieved given a particular size and volume fraction of pinning particles:

$$R_c = \frac{4r}{3f} \qquad \text{Equation 7.1}$$

where R_c is the critical maximum grain size radius, r is the radius of the pinning particles, and f is the volume fraction of the pinning particles.

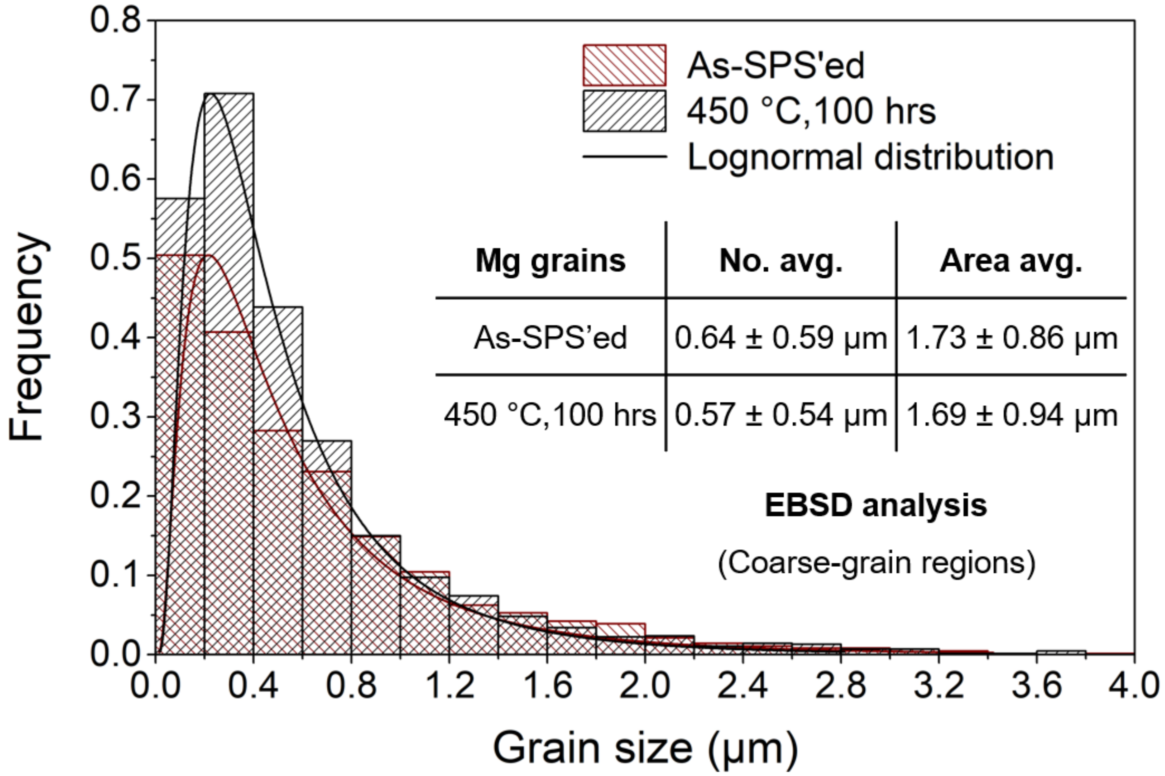

Figure 7.10: Grain size histograms overlays as measured by EBSD for both the as-SPS'ed sample and the sample heat-treated at 450 °C for 100 hours.

Given this Zener equation and assuming that the pinning particles in the as-SPS'ed sample are MgO with a number average particle size of 7 ± 3 nm (as measured by TEM) with a volume fraction between 0.15 and 0.20 (as estimated by EDS), we are able to calculate the critical maximum grain size for the Mg grains in which normal grain growth above this critical value will not take place due to the pinning force exerted by the MgO particles. Given these values, a critical maximum grain size of approximately 50 nm is calculated, below which the Mg grains will be stable. While it is clear that there are Mg grains that are larger than this critical value, as demonstrated by TEM and EBSD, these coarse Mg grains are absent of the nanocrystalline MgO grains. This absence of the MgO grains means that the pinning force is not present for these grains. However, as stated earlier, the thermal stability of these coarse Mg grains might be due to their relative confinement.

Table 7.8: Grain size values as measured by EBSD for the as-SPS'ed sample and samples heat-treated at 150, 250, 350, and 450 °C for 100 hours.

	Number avg. (μm)	**Area avg. (μm)**
As-SPS'ed	0.64 ± 0.59	1.73 ± 0.86
150 °C, 100 hrs.	0.55 ± 0.51	1.59 ± 0.92
250 °C, 100 hrs.	0.65 ± 0.62	1.86 ± 1.01
350 °C, 100 hrs.	0.65 ± 0.60	1.81 ± 1.00
450 °C, 100 hrs.	0.57 ± 0.54	1.69 ± 0.94

It is also important to acknowledge that the RE elements might be playing a minor, or even an equal role, in the thermal stability of the as-SPS'ed compared to the thermal stability effect of the MgO particles. In truth, the role of the RE elements in the thermal stability is largely unknown. It is possible for there to be an unknown synergetic effect between the MgO and RE elements as there appears to be an intimate connection between the distribution of MgO particles and the distribution of the RE elements, with both distributions occurring in the nanocrystalline regions as measured from the ESD mapping and point analysis (both from the SEM and STEM), This correlation between the nanocrystalline regions and the distribution of the RE elements might simply be due to the fact that this is where the overwhelming area fraction of grain boundaries are located due to the nature of nanocrystalline grains, and due to the large lattice mismatch between Mg and the RE elements, this is their preferred location. This would also be supported by the XRD analysis which shows that no RE-containing phases are present, indicating that they are elementally distributed to the grain boundaries. Additionally, it is also important to note that no other phases were detected in the EBSD data for any of the heat-treated data, including the sample heat-treated at 450 °C for 100 hours, showing that the MgO grains remain nanocrystalline and supporting the results from both the conventional and synchrotron XRD.

7.3 Mechanical Properties

7.3.1 Elastic Modulus and Hardness

The elastic modulus and hardness for all of the four temperature regimes for the varying times were measured with the MTS Nano Indenter XP with the elastic modulus and hardness data presented in Figures 7.11 and Figure 7.12, respectively. These graphs also display the as-SPS'ed properties at an annealing time of zero hours indicating no heat treatment. For all data within each temperature (i.e. all samples heated at 150 °C), the data was averaged and a line was horizontal line was placed on each graph with the average value being placed just below the data. In addition to these graphs, the elastic modulus and hardness data from heat-treated samples heated for 100 hours at 150, 250, 350, and 450 °C is listed in table format with the elastic modulus data being given in Table 7.9 and the hardness data being given in Table 7.10.

Comparing the most extreme heat treatment, i.e. the sample heated at 450 °C for 100 hours, to the as-SPS'ed samples, there does not seem to be any significant differences for both the elastic modulus and hardness values. Looking at the elastic modulus values, the as-SPS'ed sample had an elastic modulus of 58.4 ± 3.6 compared to 62.2 ± 3.3 for the sample heated at 450 °C for 100 hours. While this difference in elastic modulus is technically statistically significant given number of indentations and their standard deviation values, it is not different enough to draw any real conclusions from. This difference could simply be due to slight variations in the testing conditions as elastic modulus measurements are quite sensitive to differences in sample tilt and frame stiffness. In terms of hardness, which is less sensitive to these conditions, there is no statistical difference between the as-SPS'ed sample and the sample heated at 450 °C for 100 hours with hardness values of 1.26 ± 0.13 GPa and 1.22 ± 0.12 GPa, respectively. From this data it is clear that there is no significant difference between the as-SPS'ed sample and any of the heat-treated samples, and that the material is remarkably stable at elevated temperatures even up to 100 hours at 450 °C.

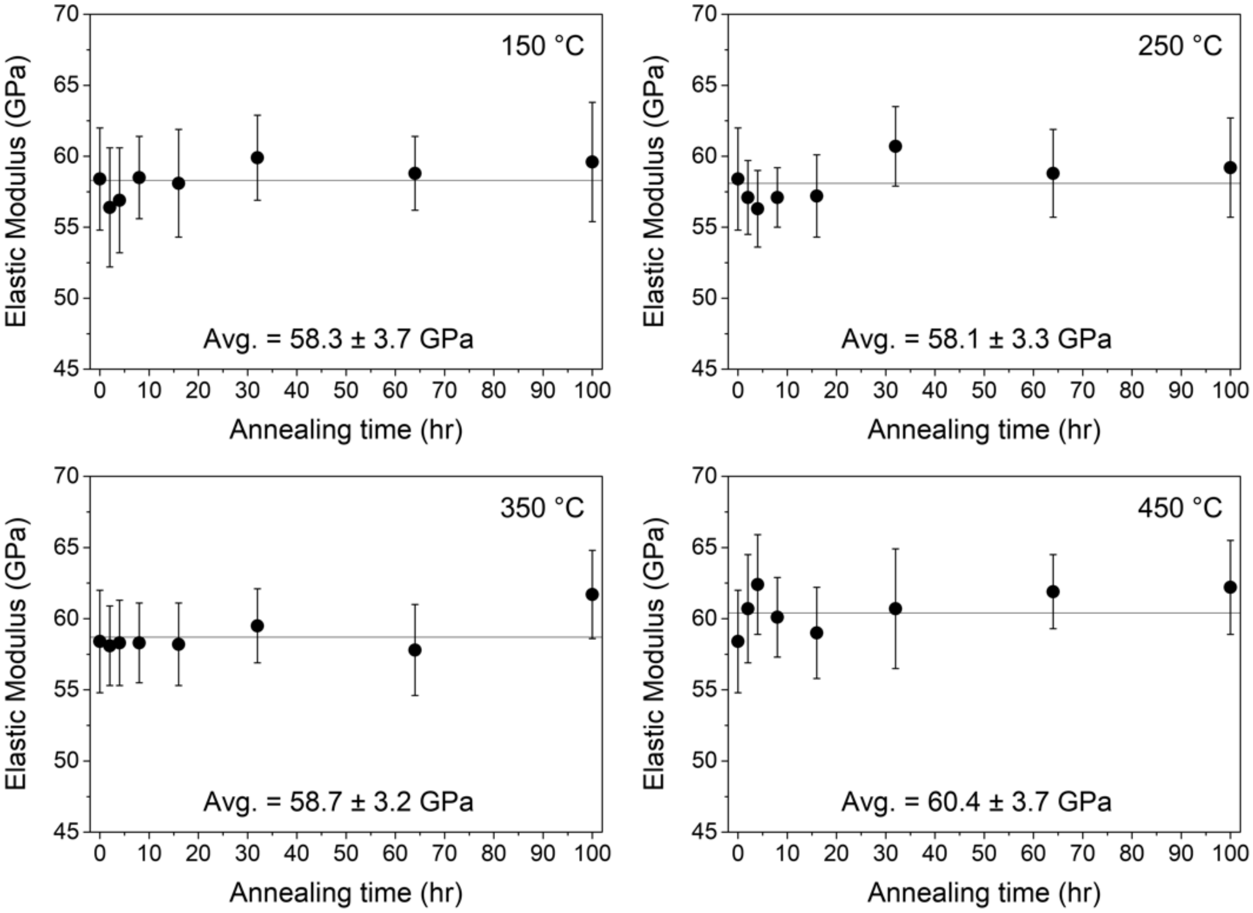

Figure 7.11: Elastic modulus as measured by nanoindentation for the as-SPS’ed sample and samples heat-treated at 150, 250, 350, and 450 °C for 2, 4, 8, 16, 32, 64, and 100 hours.

Table 7.9: Homologous temperature and elastic modulus summary as measured by nanoindentation for the as-SPS’ed sample and samples heat-treated at 150, 250, 350, and 450 °C for 100 hours.

	T/T_m	Elastic modulus (GPa)*
As-SPS’ed	-	58.4 ± 3.6
150 °C, 100 hrs.	0.52	59.6 ± 4.2
250 °C, 100 hrs.	0.64	59.2 ± 3.5
350 °C, 100 hrs.	0.77	61.7 ± 3.1
450 °C, 100 hrs.	0.89	62.2 ± 3.3

* Calculated using a melting temperature of 540 °C (813 K).

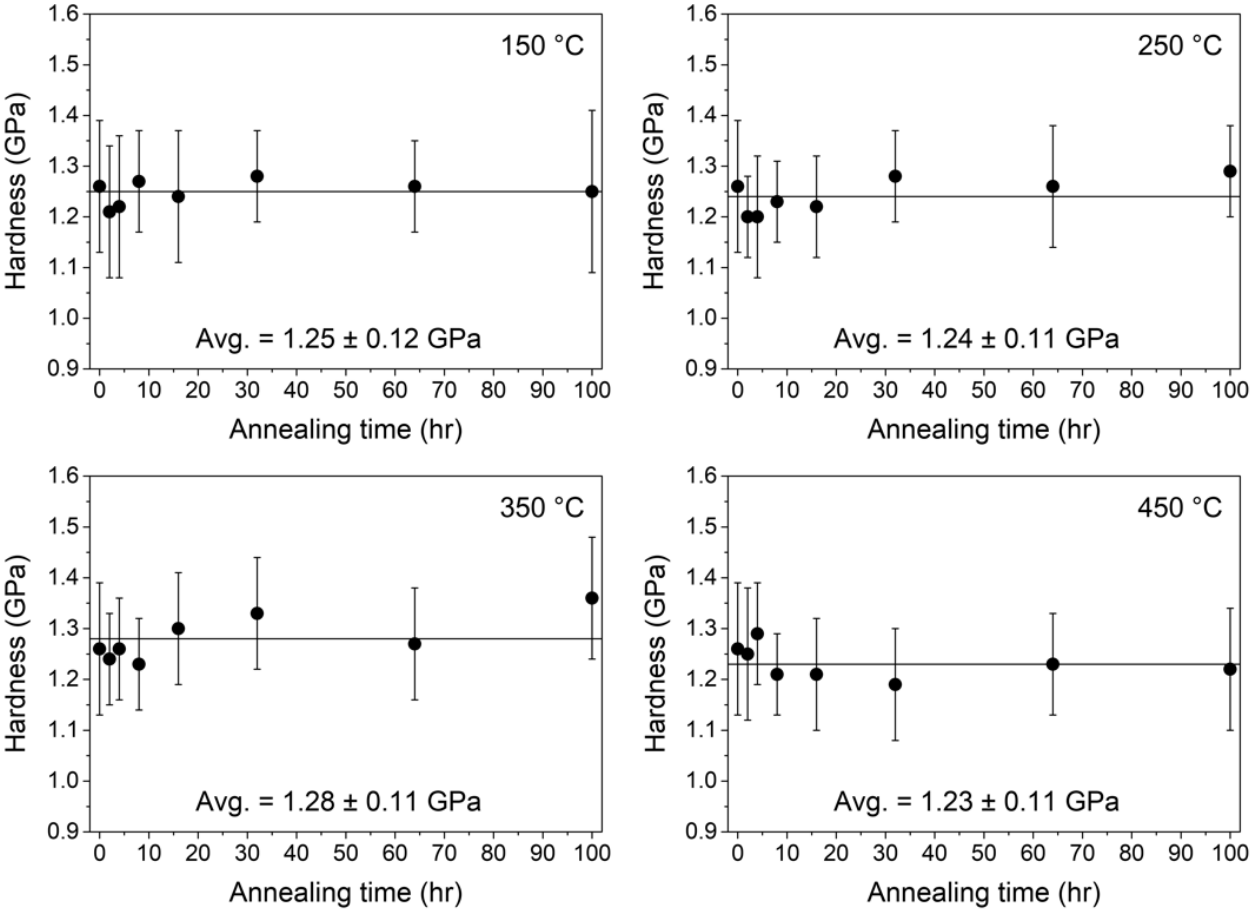

Figure 7.12: Hardness as measured by nanoindentation for the as-SPS'ed sample and samples heat-treated at 150, 250, 350, and 450 °C for 2, 4, 8, 16, 32, 64, and 100 hours.

Table 7.10: Homologous temperature and hardness summary as measured by nanoindentation for the as-SPS'ed sample and samples heat-treated at 150, 250, 350, and 450 °C for 100 hours.

	T/T_m	**Hardness (GPa)**
As-SPS'ed	-	1.26 ± 0.13
150 °C, 100 hrs.	0.52	1.25 ± 0.16
250 °C, 100 hrs.	0.64	1.29 ± 0.09
350 °C, 100 hrs.	0.77	1.36 ± 0.12
450 °C, 100 hrs.	0.89	1.22 ± 0.12

7.3.2 Compressive Yield Strength

In order to confirm the hardness results which demonstrated that there was no difference between the as-SPS'ed sample and the sample heat treated at 450 °C for 100 hours, micro-compression testing of the sample heat treated at 450 °C for 100 hours was conducted. These results are presented in Figure 7.13 which shows the as-SPS'ed sample having a compressive yield strength of 325 ± 19 MPa and the sample heat-treated at 450 °C for 100 hours having a value of 327 ± 17 MPa. These virtually identical results confirm the hardness results and shows that the sample is unaffected in terms of mechanical properties by a very harsh heat treatment of $0.9T_m$ for 100 hours. These micropillar compression results also heavily reinforce the conclusions that there were no significant microstructural changes as determined by SEM, XRD, and EBSD. Although TEM analysis was not conducted on the sample heated at 450 °C for 100 hours in order to ascertain the nanocrystalline grains, EBSD showed that there was no distinguishable difference in coarse grain size (grains over 100 nm) compared to the as-SPS'ed sample.

In addition to there not being any discernable difference between the compressive yield strengths for both the as-SPS'ed sample and sample heat-treated at 450 °C for 100 hours, there also does not seem to be any difference in ductility as both samples with both samples showing ductility well beyond 5% strain during compression. This is not surprising given all of the microstructural characterization and initial mechanical property results from nanoindentation which showed that no major differences between the as-SPS'ed sample and heat-treated samples could be detected. It also proves that the slight coarsening of the MgO grains in the sample heat-treated at 450 °C for 100 hours had no effect on the strength or ductility of the sample, at least when performed under compression. As we will discuss in the next chapter, additional mechanical testing would have to be performed in order to determine the ductility of the as-SPS'ed sample and heat-treated samples under different loading conditions.

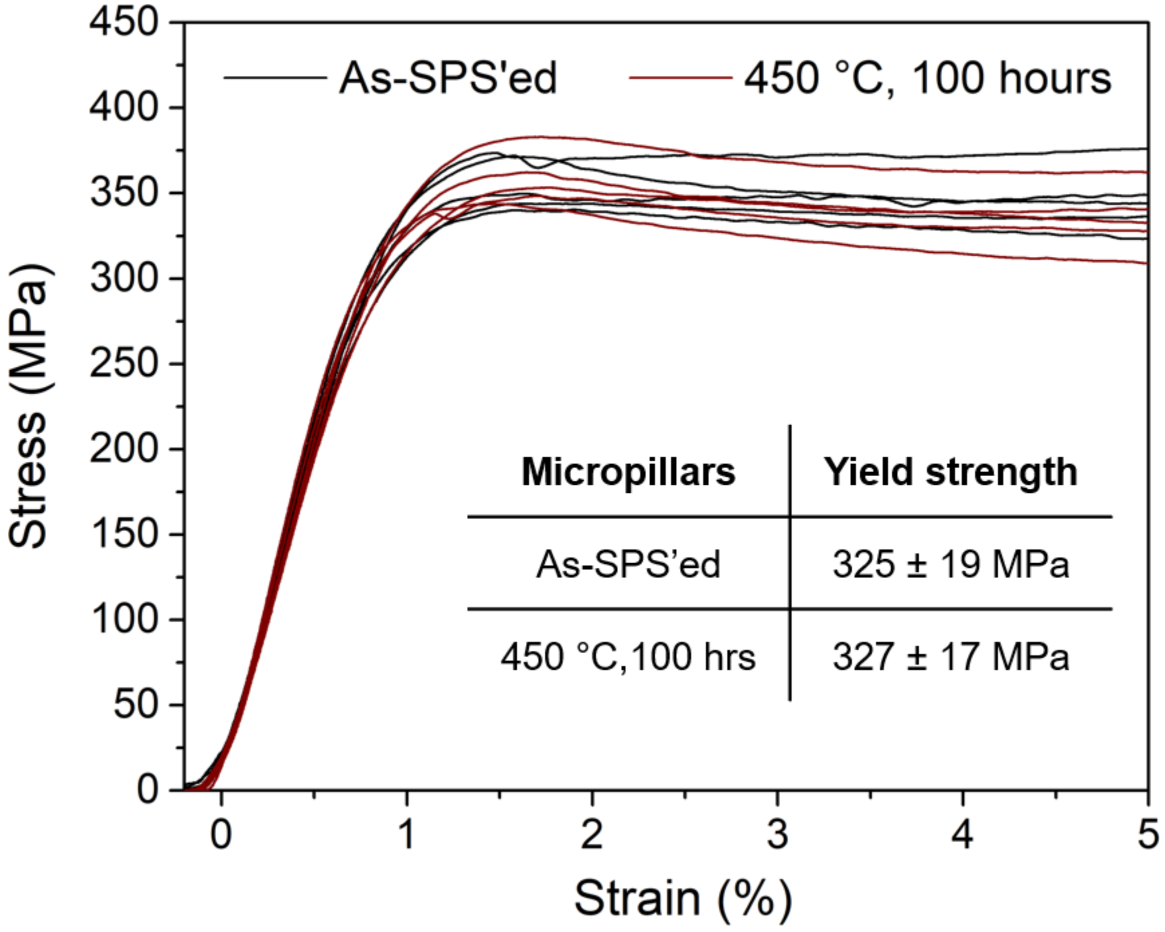

Micropillars	Yield strength
As-SPS'ed	325 ± 19 MPa
450 °C,100 hrs	327 ± 17 MPa

Figure 7.13: Micropillar compression results for both the as-SPS'ed sample and the sample heat-treated at 450 °C for 100 hours along with their respective compressive yield strengths.

Chapter 8

Conclusions

8.1 Summary of Current Work

Mg-4Y-3RE gas atomized powders were successfully cryomilled, achieving the desired goal of obtaining a nanocrystalline grain structure for the Mg-based alloy with a number and area average grain size for the Mg grains of 11 ± 7 nm and 20 ± 9 nm, respectively, as directly measured by TEM with no grains over 50 nm being measured. In addition to achieving nanocrystalline Mg grains from the cryomilling process, an extremely fine dispersion of MgO nanoparticles were introduced into the Mg matrix as a result of the cryomilling with a number and area average grain size for the MgO grains of 5 ± 2 nm and 6 ± 2 nm, respectively, again directly measured from TEM analysis. While the cryomilling process had a drastic effect on the grain size of the powders, it did not seem to have any effect on the powder particle size which was virtually unchanged before and after cryomilling with a volume mean diameter of the as-received powder and cryomilled powders are 19.6 ± 11.6 μm and 17.9 ± 6.8 μm, respectively. The cryomilling process also was shown to eliminate the non-equilibrium Mg_3RE intermetallic phase in the as-received powders created during the gas atomization process while not creating any additional intermetallic phases with the only additional phase to the α-Mg phase being the MgO phase. The STEM HAADF images along with the STEM-EDS mapping showed that there was an uneven distribution of the Mg and MgO phases along with un uneven distribution of the RE elements with the RE elements seeming to solely occupy the regions containing the nanocrystalline Mg grains and MgO nanoparticles.

Both the as-received and cryomilled powders were consolidated by SPS at 425 °C with consolidated densities of 1.84 g/cm^3 and 2.11 g/cm^3 for the SPS control sample (SPS of as-received powders) and the as-SPS'ed sample, respectively, showing a significant different in density despite both samples being almost fully consolidated. Consolidation by SPS was shown to be successful for the cryomilled powders but was shown to not quite be a success for the as-received powders due to the distinct presence of PPBs in the SPS control sample as imaged by SEM which showed that the passivated oxygen layer on the surface of the powders inhibited surface diffusion during the sintering process. No such PPBs were seen in the as-SPS'ed sample primarily due to the fact that the cryomilling process broke up this passivation layer and homogenized the powders to a certain extent, making surface diffusion of the powders much easier. There was also a large difference in the occurrence of phases in both the SPS control sample as well as the as-SPS'ed sample. While the predominant phases present in the as-received powders were α-Mg and the Mg_3RE intermetallic phase, the SPS control sample showed that the intermetallic Mg_3RE phase was eliminated and replaced with a different intermetallic phase, that being the equilibrium $Mg_{41}Nd_5$ intermetallic phase. The as-SPS'ed sample showed no such additional phases, besides α-Mg and MgO, indicating that the RE elements were not participating in the formation of any phases and most likely elementally distributed to the nanocrystalline grain boundaries as evidenced by their overwhelming occurrence in these nanocrystalline regions.

While the as-SPS'ed sample did not show any additional phases as a result of the SPS process, the grain structure was affected, resulting in a bimodal distribution of the Mg grains while also showing a quasi-duplex microstructure with two distinct regions as seen with SEM. These two regions, while not strictly a duplex microstructure, were easily differentiated by SEM which showed dramatic contrast differences with the brighter regions containing most, if not all, of the MgO and RE elements with the darker regions containing essentially all Mg. Two main methods were used to characterize the grain structure of these two regions, with TEM characterizing the nanocrystalline

Mg grains (grains < 100 nm) and EBSD characterizing the coarser Mg grains (grains > 100 nm) with nanocrystalline grains having a number and area average grain size for the Mg grains of 9 ± 6 nm and 20 ± 12 nm, respectively, and the coarser grains having a number and area average grain size for the Mg grains of 0.64 ± 0.59 μm and 1.73 ± 0.86 μm, respectively, showing a distinctly bimodal grain structure. TEM grain analysis was also performed on the MgO grains which showed a number and area average grain size for the MgO grains of 7 ± 3 nm and 11 ± 6 nm, respectively, with no coarse MgO grains being detected by EBSD indicating a very narrow grain size distribution. This characterization for both the Mg and MgO grains demonstrates that a large portion of the nanocrystalline Mg grains were unaffected by the SPS process with the MgO grains virtually not impacted at all. It was also noticed that all of the nanocrystalline MgO grains were found in regions containing nanocrystalline Mg grains, suggesting that the MgO grains might have an inhibiting effect on the grain growth of Mg.

In terms of mechanical properties, the bulk compressive strength of the as-SPS'ed sample was found to be 320 ± 4 MPa which is a remarkable increase compared to the reported compressive yield strength for bulk WE43 after the traditional processing via a T6 heat treatment which is 190 MPa. Additionally, it was shown that the bulk compressive yield strength could accurately and reliably be calculated via micropillar compression with a compressive yield strength of 325 ± 19 MPa demonstrating that the result from micropillar compression were representative of bulk properties. Elastic modulus and hardness values were also obtained for the as-SPS'ed sample via nanoindentation resulting in an elastic modulus and hardness values of 58.4 ± 3.6 GPa and 1.26 ± 0.13 GPa, respectively. While the elastic modulus is considerably higher than pure Mg (45 GPa), it was found to be a reasonable value given the non-inconsequential amount of MgO which was calculated to be between 15 and 20 volume percent as calculated via the EDS analysis which showed that oxygen constituted about 15 to 20 atomic percent of both the cryomilled powder as well as the as-SPS'ed sample.

The as-SPS'ed sample showed remarkable thermal stability in terms of both its microstructure as well as in its mechanical properties. From both SEM and EBSD results, there was no distinguishable difference between the as-SPS'ed sample and any of the heat-treated samples, including the sample heat-treated at 450 °C for 100 hours. The coarse Mg grains showed no statistical difference for the heat-treated samples as measured by EBSD with the sample heat-treated at 450 °C for 100 hours having a number and area average grain size for the Mg grains of 0.57 ± 0.54 μm and 1.69 ± 0.94 μm, respectively. Additionally, EBSD did not detect any coarse MgO grains indicating the stability of the MgO grains as well. There was also no noticeable difference between the compressive yield strengths of the as-SPS'ed sample and the heat-treated samples with the compressive yield strength of the sample heat-treated at 450 °C for 100 hours having a compressive yield strength of 327 ± 27 MPa as measured by microcompression. Similarly, there was almost no difference in both the elastic modulus and hardness for the heat-treated samples with the sample heat-treated at 450 °C for 100 hours having an elastic modulus and hardness values of 62.2 ± 3.3 GPa and 1.22 ± 0.12 GPa, respectively, as measured by nanoindentation. Ultimately, the excellent thermal stability of the composite structure was attributed to the combined effect of both the MgO nanoparticles along with the presence of the RE elements likely elementally distributed to the grain boundaries of the nanocrystalline Mg grains.

8.2 Recommendations for Future Work

8.2.1 Longer Cryomilling Times

No attempts were made in the current work to study the effects of different milling times on the microstructural and chemical evolution of the powders. Due to the high cost of the WE43 powders and high cost of the cryomilling process, a single milling time of 8 hours was chosen. This choice was mainly influenced by previous work with the mechanical alloying of elemental Mg and Al powders under the same milling conditions which showed a homogenous microstructure and an even distribution of phases for the same milling parameters at 8 hours. The assumption was that the Mg powders, although different chemically, would behalf similarly with the same pilling parameters. However, in looking back at the S/TEM images of the cryomilled powders of this current work (Chapter 5) and subsequently the as-SPS'ed sample (Chapter 6), it is apparent that 8 hours was an insufficient milling time and lead to a non-uniform distribution of elements and phases. In truth, the large *in situ* oxidation was not expected due to no such oxide forming in the earlier work previously described, and the formation of the MgO during the milling process probably added additional complexity. The non-homogeneous microstructure in the cryomilled powders, mainly the non-uniform distribution of MgO, was cited as the precursor for the eventual bimodal grain growth in the as-SPS'ed sample. While this bimodal grain structure was probably a large contributing factor to the relatively large compressive strains, it would be interesting to see the mechanical properties of a completely uniform microstructure with an even distribution of MgO. Perhaps a milling time of 16 or even 24 hours would be sufficient to achieve this.

8.2.2 Further Investigation of the Thermal Stability Mechanisms

Although the heat-treated samples were extensively investigated by EBSD, none of the heat-treated samples were microstructurally characterized by TEM, namely the sample heat-treated to 450 °C for 100 hours. From the XRD data, it was clear that the MgO particles slightly coalesced and grew during the heat treatment as evidenced by the sharpening of the MgO peaks. In order to definitively prove the microstructural thermal stability of the sample heat-treated to 450 °C for 100 hours, direct grain size measurements by TEM would have to be performed. However, based on the mechanical results, it is unlikely that these results would be significantly different than the as-SPS'ed sample due to the fact that they virtually indistinguishable from each other. In addition to further charactering the heat-treated samples, it would also help get a better insight into the thermal stability mechanism that has led to the remarkable thermal stability. Another way to gain greater insight into the thermal stability mechanisms could be achieved through mechanical testing at elevated temperature which could also demonstrate similar high-strength even at high operating temperatures. Through these additional characterization methods, a better understanding of the underlying thermal stability mechanisms could be achieved which would be extremely valuable when applying this knowledge to other material systems in order to achieve a similar level of thermal stability.

8.2.3 Deformation Mechanisms Under Different Loading Conditions

In order to fully flesh out the mechanical properties and ultimately the applicability of this nanocomposite material, sufficient ductility under non-compression type testing would have to be demonstrated. Bulk tensile samples were cut from the as-SPS'ed sample but ultimately failed when the treads sheared off during the lathe turning process. This failure was attributed to residual porosity in the material, but it is unclear whether a lack of ductility also played a role. While the ductility in both the as-SPS'ed and sample heat-treated to 450 °C for 100 hours showed promising amounts of ductility, additional modes of testing would have to be conducted to verify that the material is indeed ductile and not susceptible to brittle fracture under different loading conditions. In addition, understanding the fracture mechanisms under different loading conditions will be needed in order to better understand the complete mechanical behavior of the material. Due to the limited supply of material, micromechanical bending tests similar to microcompression could be performed with a cantilever-type structure being milled by FIB.

REFERENCES

1. A. J. Bodenlos and T. P. Thayer, “Magnesium refractories,” In: United States Mineral Resources: Geological Survey Professional Paper 820, ed. D.A. Brobst and W.P. Pratt, 1973, p. 379-384.
2. D. A. Kramer, Magnesium, its Alloys and Compounds, U.S. Geological Survey Open-File Report, 2001.
3. K. K. Turekian, Oceans, Yale University, New Jersey: Prentice-Hall, 1968.
4. T. G. Tripp, “Production of magnesium from Great Salt Lake, Utah USA,” Natural Resources and Environmental Issues, 2009, vol. 15, p. 55-61.
5. J. Wisniak, “The Dead Sea - a live pool of chemicals,” Indian Journal of Chemical Technology, 2002, vol. 9, p. 79-87.
6. L. M. Pidgeon and W. A. Alexander, “Thermal production of magnesium – pilot-plant studies on the retort ferrosilicon process,” Transactions of the American Institute of Mining and Metallurgical Engineering, 1944, vol. 159, p. 315-352.
7. W. M. Peirce, R. K. Waring, and L. D. Fetterolf, “Some developments in the production of magnesium from dolomite by the ferrosilicon process,” American Institute of Mining and Metallurgical Engineers: Technical Publication No. 1707, 1944, p. 1-14.
8. J. C. Zang, “The Pidgeon process in China and its future,” in: Magnesium Technology 2001, ed. J. N. Hryn, TMS, 2001, p. 113-116.
9. U.S. Geological Survey, Mineral Commodity Summaries, Magnesium, 2018, p. 102-103.
10. U.S. Geological Survey, Mineral Commodity Summaries, Aluminum, 2018, p. 20-21.
11. U.S. Geological Survey, Mineral Commodity Summaries, Iron and Steel, 2018, p. 82-83.
12. U.S. Geological Survey, Mineral Commodity Summaries, 2014, p. 98-99.
13. U.S. Geological Survey, Mineral Commodity Summaries, Magnesium, 1999, p. 106-107.

14. H. Friedrich and S. Schumann, "Research for a 'new age of magnesium' in the automotive industry," Journal of Materials Processing Technology, 2001, vol. 117, p. 276-281.
15. R. E. Brown, "Future of magnesium developments in 21st century," in: Presentation at Materials Science & Technology Conference, Pittsburgh, PA, USA, October 5-9, 2008.
16. G. D. Wardlow, "A changing world with different rules – new opportunities for magnesium alloys," in: Presentation at the 64th Annual World Magnesium Conference, Vancouver, BC, Canada, May 13th-15th, 2007.
17. F. Hollrigl-Rosta, "Magnesium in Volkswagen," Light Metal Age, 1980, 22-29.
18. A. A. Luo, "Magnesium casting technology for structural applications," Journal of Magnesium and Alloys, 2013, vol. 1, no. 1, p. 2-22.
19. O. Pashkova, I. Ostrovsky, Y. Henn, "Present state and future of magnesium application in aerospace industry," in: Presentation at New Challenges in Aeronautics, Moscow, 2007.
20. U.S. Geological Survey, Mineral Commodity Summaries, Magnesium, 2018, p. 102-103.
21. M. M. Avedesian, H. Baker, Magnesium and Magnesium Alloys, ASM International, Materials Park, OH, 1999.
22. E. C. Burke and W. R. Hibbard Jr., "Plastic deformation of magnesium single crystals," Transactions of the American Institute of Mining and Metallurgical Engineers, 1952, vol. 194, p. 295-303; *also see* Journal of Metals, March 1952.
23. R. v. Mises, "Mechanik der plastischen formänderung von kristallen" ("Mechanics of plastic deformation of crystals"), Zeitschrift für Angewandte Mathematik und Mechanik (Journal of Applied Mathematics and Mechanics), 1928, vol. 8, no. 3, p. 161-185 (in German).
24. E. O. Hall, "The deformation and ageing of mild steel: III discussion of results," Proceedings of the Physical Society B, 1951, vol. 64, no. 9, p. 747-753.
25. N. J. Petch, "The cleavage strength of polycrystals," Journal of the Iron and Steel Institute, 1953, vol. 174, p. 25-28.

26. J. P. Hirsh and J. Lothe, Theory of Dislocations, Krieger Publishing Company, Malabar, Florida, 1982.

27. T. G. Nieh and J. Wadsworth, "Hall-Petch relation in nanocrystalline solids," Scripta Metallurgica et Materialia, 1991, vol. 25, p. 955-958.

28. R. Z. Valiev, Y. Estrin, Z. Horita, T. G. Langdon, M. J. Zehetbauer, and Y. T. Zhu, "Producing bulk ultrafine-grained materials by severe plastic deformation," The Journal of The Minerals, Metals, and Materials Society, 2006, vol. 58, no. 4, p. 33-39.

29. R. Z. Valiev, R. K. Islamgaliev, and I. V. Alexandrov, "Bulk nanostructured materials from severe plastic deformation," Progress in Materials Science, 2000, vol. 45, no. 2, p. 103-189.

30. N. A. Smirnova, V. I. Levit, V. P. Pilyugin, R. I. Kuznetsov, L. S. Davydova, and V. A. Sazonova, "Evolution of the FCC single-crystal structure during severe plastic deformation," The Physics of Metals and Metallography, 1986, vol. 61, no. 6, p. 127-134 (in Russian).

31. X. Zhao, W. Fu, X. Yang, and T. G. Langdon, "Microstructure and properties of pure titanium processed by equal-channel angular pressing at room temperature," Scripta Materialia, 2008, vol. 59, no. 5, p. 542-545.

32. X. Z. Liao, Y. H. Zhao, Y. T. Zhu, R. Z. Valiev, and D. V. Gunderov, "Grain-size effect on the deformation mechanisms of nanostructured copper processed by high-pressure torsion," Journal of Applied Physics, 2004, vol. 96, p. 636-640.

33. H. Jiang, Y. T. Zhu, D. P. Butt, I. V. Alexandrov, and T. C. Lowe, "Microstructural evolution, microhardness, and thermal stability of HPT-Processed Cu," Materials Science and Engineering A, 2000, vol. 290, p. 128-138.

34. A. P. Zhilyaev, G. V. Nurislamova, B. K. Kim, M. D. Baro, J. A. Szpunar, and T. G. Langdon, "Experimental parameters influencing grain refinement and microstructural evolution during high-pressure torsion," Acta Materialia, 2003, vol. 51, no. 3, p. 753-765.

35. R. Z. Valiev and A. A. Nazarov, “Bulk nanostructured materials by SPD processing: techniques, microstructures, and properties,” in: Bulk Nanostructured Materials, ed. M. J. Zehetbauer and Y. T. Zhu, Wiley-VCH, 2009, Chapter 2, p. 21-48.
36. C. Suryanarayana, “Mechanical alloying and milling,” Progress in Materials Science, 2001, vol. 46, p. 1-184
37. A. W. Weeber, H. Bakker, and F. R. De Boer, “The preparation of amorphous Ni-Zr powder by grinding the crystalline alloy,” Europhysics Letters, 1986, vol. 2, no. 6, p. 445-448.
38. R. Petkovic-Luton and J. Vallone “Composite dispersion strengthened composite metal powders,” US Patent No. 4,619,699, 1986.
39. M. J. Luton, C. S. Jayanth, M. M. Disko, S. Matras, and J. Vallone, “Cryomilling of nano-phase dispersion strengthened aluminum,” In: “Multicomponent Ultrafine Microstructures,” ed. L. E. McCandlish, D. E. Polk, R. W. Siegel, and B. H. Kear, Materials Research Society Symposium Proceedings (Boston, Massachusetts), 1989, vol. 132, p. 79-86.
40. A. S. Helle, K. E. Easterling, and M. F. Ashby, “Hot-isostatic pressing diagrams: new developments,” Acta Materialia, 1985, vol. 33, no. 12, p. 2163-2174.
41. H. V. Atkinson and S. Davies, “Fundamental aspects of hot isostatic pressing: an overview,” Metallurgical and Materials Transactions A, 2000, vol. 31, p. 2981-3000.
42. S. H. Risbud, J. R. Groza, and M. J. Kim, “Clean grain boundaries in aluminum nitride ceramics densified without additives by a plasma-activated sintering process,” Philosophical Magazine B, 1994, vol. 69, no. 3, p. 525-533.
43. Z. A. Munir, U. Anselmi-Tamburini, and M. Ohyanagi, “The effect of electrical field and pressure on the synthesis and consolidation of materials: a review of the spark plasma sintering method,” Journal of Materials Science, 2006, vol. 41, p. 763-777.
44. G. F. Taylor, “Apparatus for making hard metal compositions,” US Patent No. 1,896,854, 1933.

45. O. Yanagisawa, T. Hatayama, and K. Matsugi, “Recent research on spark sintering process,” Materia Japan, 1994, vol. 33, no. 12, p. 1489-1496.

46. M. Tokita, “Development of large-size ceramic/metal bulk FGM fabricated by spark plasma sintering,” in Materials Science Forum, Proceedings of the 5th International Symposium on Functionally Graded Materials, ed. W. A. Kaysser, Switzerland, 1999, p. 83-89.

47. M. Nygren and Z. Shen, “On the preparation of bio-, nano- and structural ceramics and composites by spark plasma sintering,” Solid State Sciences, 2003, vol 5, p. 125-131.

48. A. M. Mullis, L. Farrell, R. F. Cochrane, and N. J. Adkins, “Estimation of cooling rates during close-coupled gas atomization using secondary dendrite arm spacing measurement,” Metallurgical and Materials Transactions B, 2013, vol. 44, p. 992-999.

49. D. B. Witkin and E. J. Lavernia, “Synthesis and mechanical behavior of nanostructured materials via cryomilling,” Progress in Materials Science, 2006, vol. 51, p. 1-60.

50. P. Scherrer, "Bestimmung der Grösse und der inneren Struktur von Kolloidteilchen mittels Rötgenstrahlen,” Nachrichten von der Königlichen Gesellschaft der Wissenschaften zu Göttingen, Mathematisch-Physikalische Klasse 1918, p. 98-100 (in German).

51. A. Guinuer. X-ray Diffraction in Crystals, Imperfect Crystals, and Amorphous Bodies, W. H. Freeman and Company, San Francisco and London, 1963.

52. V. Uvarov and I. Popov, “Metrological characterization of x-ray diffraction methods at different acquisition geometries for determination of crystallite size in nano-scale materials,” Materials Characterization, 2013, vol. 85, p. 111-123.

53. Y. Hirai and H. Kamitsubo, “Industrial use of synchrotron radiation at the SAGA Light Source,” Synchrotron Radiation News, vol. 27, no. 3, 2014, p. 11-14.

54. W. C. Oliver and G. M. Pharr, “An improved technique for determining hardness and elastic modulus using load and displacement sensing indentation experiments,” Journal of Materials Research, 1992, vol. 7, no. 6, p. 1564-1583.

55. M. S. Kashani and V. Madhavan, “Analysis and correction of the effect of sample tilt on results of nanoindentation,” Acta Materialia, vol. 59, 2011, p. 883-895.
56. I. N. Sneddon, “The relation between load and penetration in the axisymmetric Boussinesq problem for a punch of arbitrary profile,” International Journal of Engineering Science, 1965, vol. 3, p. 47-57.
57. E. S. Berkovich, "Three-faceted diamond pyramid for studying microhardness by indentation," Zavodskaya Laboratoria, vol. 13, no. 3, 1950, p. 345-347 (in Russian).
58. M. M. Khrushchov and E. S. Berkovich, "Methods of determining the hardness of very hard materials: the hardness of diamond," Industrial Diamond Review, 1951, vol. 11, p. 42-49.
59. G. Simmons and H. Wang, Single Crystal Elastic Constants and Calculated Aggregate Properties: A Handbook, MIT Press, Cambridge, MA, 1971
60. C. P. Frick, B. G. Clark, S. Orso, A. S. Schneider, and E. Arzt, "Size effect on strength and strain hardening of small-scale [111] nickel compression pillars," Materials Science and Engineering A, 2008, vol. 489, p. 319-329.
61. C. A. Volkert and E. T. Lilleodden, "Size effects in the deformation of sub-micron Au columns," Philosophical Magazine, 2006, vol. 86, p. 5567-5579.
62. C. Goujon, P. Goeuriot, P. Delcroix, and G. Le Caër, “Mechanical alloying during cryomilling of a 5000 Al alloy/AlN powder: the effect of contamination,” Journal of Alloys and Compounds, 2001, vol. 315, p. 276-283.
63. B. Akinrinlola, R. Gauvin, C. Blais, and M. Brochu, “Thermal stability of cryomilled Al-Mg-Er powders,” Journal of Nanomaterials, 2017, p. 1-17.
64. L. L. Rokhlin, T. V. Dobatkina, I. E. Tarytina, V. N. Timofeev, and E. E. Balakhchi, “Peculiarities of the phase relations in Mg-rich alloys of the Mg-Nd-Y system,” Journal of Alloys and Compounds, 2004, vol. 367, p. 17-19.

65. D. Tolnai, C. L. Mendis, A. Stark, G. Szakács, B. Wiese, K. U. Kainer, and N. Hort, “In situ synchrotron diffraction of the solidification of Mg-RE alloys,” in: Magnesium Technology 2013, ed. N. Hort, S. N. Mathaudhu, N. R. Neelameggham, and M. Alderman, TMS, 2013, p. 253-257.
66. K. S. Ravichandran, “Elastic properties of two-phase composites,” Journal of the American Ceramic Society, 1994, vol. 77, no. 5, p. 1178-1184.
67. G. Simmons and H. Wang, Single Crystal Elastic Constants and Calculated Aggregate Properties: A Handbook, Second Edition, Cambridge, Massachusetts, The MIT Press, 1971.
68. C. S. Smith, “Introduction to grains, phases, and interfaces – an interpretation of microstructure,” Transaction of the Metallurgical Society of AIME, 1948, vol. 175, p. 15-51.
69. P. A. Manohar, M. Ferry, and T. Chandra, “Five decades of the Zener equation,” Iron and Steel Institute of Japan (ISIJ) International, 1998, vol. 38, no. 9, p. 913-924.